Thermally excited 630.0 nm emissions in the polar ionosphere

Norah Kaggwa Kwagala

Thesis for the Degree of Philosophiae Doctor (PhD)
University of Bergen, Norway
2018

UNIVERSITY OF BERGEN

Thermally excited 630.0 nm emissions in the polar ionosphere

Norah Kaggwa Kwagala

University of Bergen

UNIS
The University Centre in Svalbard

Thesis for the Degree of Philosophiae Doctor (PhD)
at the University of Bergen

2018

Date of defence: 24.08.2018

Year: 2018

Title: Thermally excited 630.0 nm emissions in the polar ionosphere

Name: Norah Kaggwa Kwagala

Print: Skipnes Kommunikasjon / University of Bergen

Thermally excited 630.0 nm emissions in the polar ionosphere

Norah Kaggwa Kwagala

University of Bergen

UNIS
The University Centre in Svalbard

Thesis for the degree of Philosophiae Doctor (PhD)

Department of Physics and Technology
University of Bergen

April 2018

Abstract

This thesis investigates the importance and significance of thermally excited 630.0 nm emissions in the cusp and polar ionosphere. Thermal excitation by heated ambient electrons in the cusp and polar ionosphere is a rarely studied source of 630.0 nm emissions in this region, and is therefore, not well represented in literature. On the other hand, direct impact excitation by precipitating electrons and dissociative recombination have been extensively studied and they are believed to be the main sources of 630.0 nm emissions. This thesis utilizes ground-based incoherent scatter radar and optical measurements from Svalbard to study the thermally excited emissions. The thermal excitation component of the 630.0 nm emission is derived from EISCAT Svalbard Radar measurements. The thermal excitation component is then studied through both case and statistical studies presented in three scientific papers.

The first part of this thesis investigates the contribution of the thermal component to the total observed 630.0 nm emission, and for the first time the thermal excitation component is separated from the observed total 630.0 nm emission intensity. The contribution is quantified and characteristics investigated. The second part of the thesis statistically investigates the occurrence of thermally excited emissions specifically focussing on the strong (intensity $>$ 1 kR) thermal component. The magnetic local time distribution, emission intensity levels, ionosphere, solar wind and interplanetary magnetic field conditions, seasonal and solar cycle variations of the strong thermal excitation component are investigated.

The main conclusions of this thesis are:

$\rightarrow$ Thermal excitation can be important in the cusp and polar ionosphere, particularly on the dayside. It should therefore, be taken into account when studying dayside 630.0 nm emissions and electron thermal balance in this region.

$\rightarrow$ The strong thermal excitation component maximizes around magnetic noon, with

an occurrence rate of $\sim$10%.

$\rightarrow$ When the strong thermal component is present, it can contribute $>$50% of the total 630.0 nm emission intensity.

$\rightarrow$ The thermally excited emissions have a relatively high peak emission altitude of $\sim$350 km, and could be responsible for the 630.0 nm emission at such altitudes and above.

$\rightarrow$ Thermal excitation is most likely to give rise to 630.0 nm emission intensities of order of kRs, when the electron gas temperature exceeds $\sim$2500 K for electron densities $\sim$(1-8)$\times 10^{11}$ m^{-3}.

$\rightarrow$ Thermal excitation in the cusp and polar ionosphere maximizes during equinox and/or solar maximum.

$\rightarrow$ Magnetic reconnection on the dayside is most likely the main driving process of the strong thermal excitation in the cusp and polar ionosphere.

Acknowledgements

I am very grateful for the opportunity to pursue a PhD at the Birkeland Centre for Space Science (BCSS) at the Department of Physics and Technology, University of Bergen. I am also thankful for the chance to be a guest student at the University Centre in Svalbard (UNIS), where I got to spent the first half of 2016. I have also presented my research at international meetings in USA and Austria, an opportunity I truly appreciate. My PhD project has been funded by the Norwegian Research Council; this has afforded me a unique and unforgettable experience. The BCSS group has provided a perfect and conducive environment where colleagues are also friends, contributing greatly not only to my academic/work well-being, but also to my social life through coffee breaks, lunch at 11:30, 'norsklunsj', parties, dinners, and 'hyttetur'.

I would like to thank my supervisor, Kjellmar Oksavik. I am very grateful for your invaluable advice, guidance and discussions. Your eagerness to help, prompt feedback, and encouragement when you spot potential, have all been truly appreciated. I have enjoyed working with you for the past five years, since I started my Master's degree in 2013. I would also like to thank my co-supervisors: Dag Lorentzen and Magnar Johnsen. The lack of frequent face-to-face meetings has not stopped you from providing feedback and participating in fruitful discussions about our research. This thesis would not have been the same without you.

Many people have made this work possible. I would like to thank Karl Laundal and Herbert Carlson for the helpful discussions we have had. I would like to thank the former Q2 group of BCSS: Theresa, Kjellmar, Kalle, Dag, Lisa, Jesper, and Katie for the useful discussions. I would also like to thank Beate Humberset and Carolina Maiorana for their company and for listening and responding to my sometimes abstract questions. I thank Kavitha Østgaard for her advice on grammar and figure formatting, and Jone Reistad for the help with latex configuration, and Paul Tenfjord for the help with different programming languages. I thank Kjellmar, Dag, Magnar, Christine Smith-Johnsen, Marit Sandanger and Katie Herlingshaw for proof-reading my thesis. Unfortunately, I don't have enough space to mention everyone who has helped me, but am truly appre-

ciative to all BCSS members.

I would like to thank my 'two families' for the encouragement and support. My friends from the Anglican Church in Bergen have been my family based in Norway. Then, I thank my parents, brothers Silas and Ezra, sister-in-law Jessica, in Uganda, for your prayers, love, support and encouragement through this period. Juliet, my dear niece, you provided the perfect distraction at the time I needed it most, thank you. Finally, I thank the Almighty God for yet another accomplishment.

For data used; I acknowledge the NASA/GSFC's Space Physics Data Facility's OMNIWeb service, and OMNI data (`https:omniweb.gsfc.nasa.gov/`). The EISCAT data were accessed from `https://www.eiscat.se` and processed using GUISDAP. EISCAT is an international association supported by research organizations in China (CRIRP), Finland (SA), Japan (NIPR and STEL), Norway (NFR), Sweden (VR), and the United Kingdom (NERC). The Meridian Scanning Photometer (MSP) data from Kjell Henriksen Observatory (KHO) were provided by Dag Lorentzen. The NRLMSISE-00 Atmospheric model was accessed from
`https://ccmc.gsfc.nasa.gov/modelweb/models/nrlmsise00.php`. Simulation results for the TIE-GCM model have been provided by the Community Coordinated Modelling Center at Goddard Space Flight Center through their public Runs on Request system (`http://ccmc.gsfc.nasa.gov`). The TIE-GCM Model was developed by the R. G. Roble et al. at the High Altitude Observatory, National Center for Atmospheric Research (HAO NCAR). The TIE-GCM is an open-source community model available at the HAO/NCAR website.

Bergen, April 2018
Norah Kaggwa Kwagala

Contents

Abbreviations

λ_D	Debye length, p. 34
λ_{radar}	Wavelength of the transmitted radio wave from the radar, p. 34
ACF	Autocorrelation function, p. 35
CHAMP	Challenging Minisatellite Payload, p. 42
EISCAT	European Incoherent SCATter, p. iii
ESR	EISCAT Svalbard Radar, p. 33
EUV	Extreme ultraviolet, p. 3
FAC	Field-aligned current, also known as Birkeland current, p. 21
FTE	Flux transfer event, p. 21
GSM	Geocentric Solar Magnetic, p. 10
GUISDAP	Grand Unified Incoherent Scatter Design and Analysis Package, p. 38
HAO	High-Altitude Observatory, p. 42
hF2	height of maximum electron density, p. 23
IMF	Interplanetary magnetic field, p. 9
IPY	International Polar Year, p. 42
ISR	Incoherent scatter radar, p. 35
KHO	Kjell Henriksen Observatory, p. 31
MLT	Magnetic local time, p. 19
MSIS	Mass Spectrometer and Incoherent Scatter, p. 40
MSP	Meridian scanning photometer, p. 31

N_e Electron number density, p. 22

N_i Ion number density, p. 22

NASA National Aeronautics and Space Administration , p. 17

NCAR National Center for Atmospheric Research, p. 42

NEIALs Naturally enhanced ion acoustic lines, p. 39

nF2 maximum electron density in the F region, p. 23

NRLMSISE-00 Naval Research Laboratory Mass Spectrometer and Incoherent Scatter 2000, p. 40

PMAF Poleward moving auroral forms, p. 21

R-M Russell-McPherron, p. 12

SNR Signal-to-noise ratio, p. 36

T_e Electron temperature, p. 23

T_i Ion temperature, p. 35

TIE-GCM Thermosphere-Ionosphere-Electrodynamics General Circulation Model, p. 42

UNIS The University Centre in Svalbard, p. 4

UT Universal time, p. 4

UV Ultraviolet, p. 3

V_i line-of-sight ion drift velocity, p. 35

Chapter 1

Introduction

The Earth continuously interacts with the Sun via solar radiation and solar wind-magnetosphere coupling. The solar radiation spectrum includes X-ray, extreme ultraviolet, ultraviolet, visible and infrared radiation. The visible part, can easily be noticeable to us through the lovely sunshine in our day-to-day life. The important part for this study, however, is the extreme ultraviolet (EUV) and the ultraviolet (UV) radiation. The Sun-Earth interaction via solar wind-magnetosphere coupling manifests itself as northern (southern) lights usually visible at high latitudes in places like Norway. The northern (or southern) lights are optical emissions, which prove that part of the energetic charged particles streaming from the Sun, as solar wind, has been captured by the Earth's magnetic field, and precipitated into the upper atmosphere in polar regions. The northern lights, also known as aurora, are the focus of this thesis. An image of the sky above Svalbard from an All-Sky camera is shown in Figure 1.1. The figure shows a display of northern lights with red and green emissions.

To a large extent, the Earth is protected by the magnetic field that surrounds it, also called the geomagnetic field. However, under certain configurations the geomagnetic field and the Sun's magnetic field merge via a process called magnetic reconnection. This coupling provides charged particles in the solar wind access to the Earth's upper atmosphere. As the energetic particles precipitate into the polar atmosphere, they lose their energy either through heating of ionospheric electrons, or ionizing the neutral constituents in the atmosphere, or through direct impact excitation of neutral constituents giving off auroral emissions. Optical auroral emissions arising from the latter process have been studied extensively for more than a century [e.g., *Egeland and Burke*, 2013, and references therein]. However, optical emissions can also arise from the heated ambient electrons that were energized by the precipitating electrons. Heating in the right altitude depends on sufficiently soft (hundreds of eV) and sufficiently many precipitat-

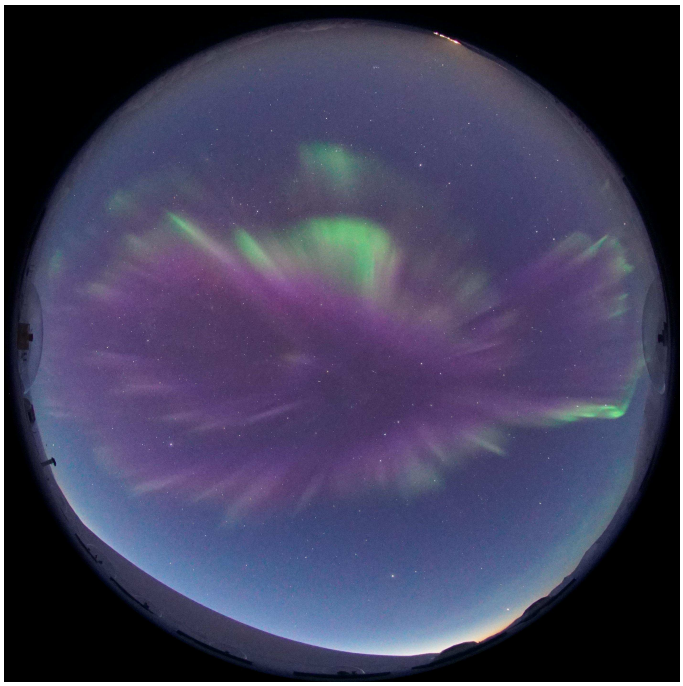

Figure 1.1: An image of the northern lights taken at the Kjell Henriksen Observatory at Longyearbyen, Svalbard, by the Sony all-sky dSRL camera belonging to the University Centre in Svalbard (UNIS) . The image was taken on November 27th 2016 at 0749 UT .

ing electrons. Thermal excited emissions occur when the ambient electrons are heated to high enough temperatures, that they cool via excitation of atomic oxygen which de-excites by giving off red aurora [e.g., *Carlson et al.*, 2013]. This process can also be referred to as thermal excitation. Models such as GLOW [*Solomon et al.*, 1988] and TRANSCAR [*Blelly et al.*, 2005; *Lilensten and Blelly*, 2002] have the physics producing thermally excited emissions built in but the topic has not been treated in its own right (except in *Johnsen et al.* [2012] which applied the GLOW model). Generally, less is known about the auroral emissions arising from thermal excitation.

In this thesis, therefore, we take up the challenge of investigating and understanding the thermally excited red auroral emissions. Earlier studies [e.g., *Gault et al.*, 1981; *Meier et al.*, 1989; *Shepherd*, 1979] have acknowledged thermal excitation as a potential source of red auroral emissions, but giving rise to negligible emission intensities and therefore considered not to be important. On the other hand, some studies [e.g., *Lockwood et al.*, 1993; *Sandholt et al.*, 2002] have indicated that thermal excitation can become important, while a few studies [e.g., *Carlson et al.*, 2013; *Johnsen et al.*, 2012;

Wickwar and Kofman, 1984] have studied thermal excitation and suggest it could be more important than earlier anticipated. If thermal excitation is important in the polar ionosphere, then;

1) The 630.0 nm (red) auroral optical measurements are not representative of direct impact excitation, but could rather be contaminated by thermally excited emissions. Optical emissions are commonly used to extract information about the dynamic solar wind-magnetosphere coupling processes. To avoid biased information, it is important that the right production processes for the auroral emissions are used.

2) The cooling of the electron gas via thermal excitation of atomic oxygen, leading to 630.0 nm emissions can be important. It is crucial to know the contribution of different heating and cooling processes of the different species in order to understand how thermal balance is attained in the atmosphere.

Thesis objective

The motivation for this thesis is triggered by the above mentioned implication of thermally excited emission in the polar ionosphere although not much is known about them. This thesis, therefore, sets out to answer two open questions;

1) How significant are thermally excited auroral emissions in the polar ionosphere?

2) When and where does thermal excitation become important in the polar ionosphere?

Approach

These questions are tackled through work presented in the three scientific papers, which form a central part of this thesis.

- **Paper I:** Kwagala, N. K., K. Oksavik, D. A. Lorentzen, and M. G. Johnsen, On the contribution of thermal excitation to the total 630.0 nm emissions in the northern cusp ionosphere, *Journal of Geophysical Research: Space Physics*, Vol. 122, doi:10.1002/2016JA023366, 2017

- **Paper II:** Kwagala, N. K., K. Oksavik, D. A. Lorentzen, and M. G. Johnsen. How often do thermally excited 630.0 nm emissions occur in the polar ionosphere? *Journal of Geophysical Research: Space Physics*, Vol. 123, doi: 10.1002/2017JA024744, 2018

- **Paper III:** Kwagala, N. K., K. Oksavik, D. A. Lorentzen, M. G. Johnsen and K. M. Laundal. Seasonal and Solar Cycle Variations of Thermally Excited 630.0 nm Emissions in the Polar Ionosphere, Submitted to *Journal of Geophysical Research: Space Physics*, 2018

Paper I applies existing theoretical knowledge from the literature, to derive the thermal excitation component of the red auroral emission, using ionospheric parameter measurements from the EISCAT Svalbard Radar. The calculations are compared to optical observations, thereby separating, for the first time, the thermal component from the observed total red aurora. The contribution from the thermal component is estimated and associated conditions in the ionosphere and solar wind are investigated. Based on the technique in Paper I, a statistical study on the occurrence of thermally excited emissions in the polar ionosphere is carried out and results on typical intensities, diurnal, seasonal, and solar cycle variations are presented in Papers II and III. The papers are collected in the Appendix.

Thesis organisation

The relevant theory and background for this thesis is given in Chapter 2, followed by a description of the instrumentation and data used in Chapter 3. Our results are summarized and discussed in Chapter 4. The conclusion of this thesis and future prospects are summarized in Chapter 5.

Chapter 2

Background and theory for the study

2.1 The Earth's ionosphere

The Earth's upper atmosphere ($\sim$>100 km) is dominated by neutral constituents. The heavier molecular constituents dominate at low altitude, below $\sim$200 km, while the lighter atomic constituents dominate at higher altitude. The Sun is the main source of energy for the Earth, and this energy is manifested in different ways in the Earth's upper atmosphere. One of the main consequences of the Sun's effect in the upper atmosphere is the presence of a partially ionized region called the ionosphere. The composition of the daytime upper atmosphere is shown in Figure 2.1.

The ionosphere is produced when the neutral constituents are ionized to produce electron-ion pairs. There are two sources of ionization in the ionosphere: photoionisation by absorption by the neutral atmosphere of solar EUV and UV radiation, and impact ionisation of the neutral atmosphere by energetic particles resulting from the Sun-Earth interaction via solar wind-magnetosphere coupling.

2.1.1 Sources of the ionisation

Photoionisation by solar EUV radiation

When EUV and UV radiation from the sun is absorbed by the neutral particles in the atmosphere, an electron may be extracted, thereby producing a free electron and an ion. The production of electron-ion pairs via absorption of a photon or radiation is known as photoionisation. The photoionisation rate from this process is dependant on the intensity of the incident radiation, the solar zenith angle, the neutral particle number density (which absorbs the radiation), the altitude, the photoionisation efficiency and the radiation absorption cross-section. The production rate by this process has been

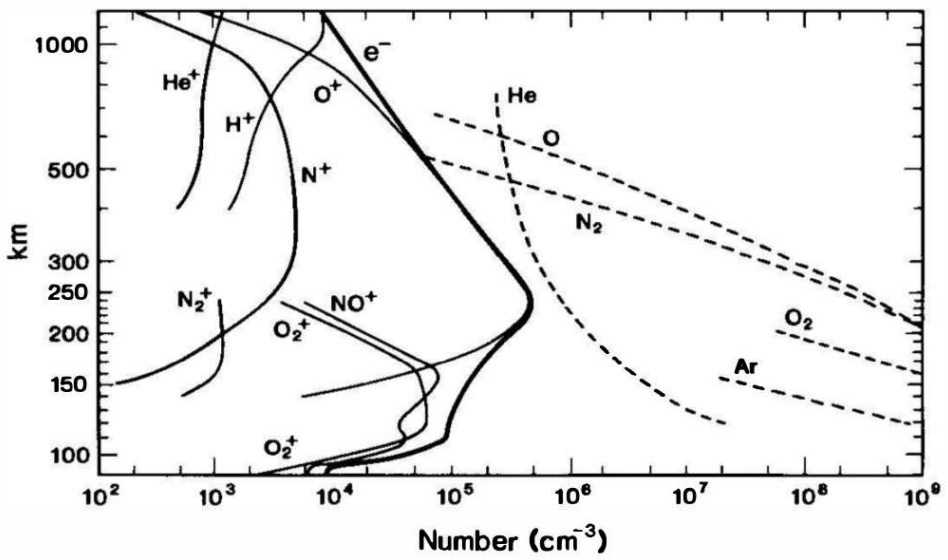

Figure 2.1: Daytime ionospheric and atmospheric composition based on mass spectrometer measurements, during the international solar quiet year. The bold lines mark the ionosphere composition, while the dashed lines mark the neutral composition. (Retrieved from *Luhmann* [1995], originally from *Johnson* [1969])

described by the Chapman production function [*Chapman*, 1931],:

$$Q_\nu(z) = \kappa_\nu \sigma_\nu n_o I_\infty \exp[-\frac{z}{H} - \frac{\sigma_\nu n_o H}{\cos\chi_\nu}\exp(\frac{-z}{H})] \tag{2.1}$$

where;
$\rightarrow Q_\nu(z)$ is the photoionisation rate per unit volume at a given height z
$\rightarrow \kappa_\nu$ is the photoionisation efficiency
$\rightarrow \sigma_\nu$ is the radiation absorption cross-section
$\rightarrow n_o$ is the atmospheric neutral density at $z = 0$
$\rightarrow I_\infty$ and χ_ν are described in Figure 2.2
$\rightarrow H$ is the scale height for an isothermal atmosphere, and the neutral density at a given altitude, $n_n(z) = n_o \exp(\frac{-z}{H})$

More details on this production process can be found in textbooks like *Kivelson and Russell* [1995] or *Baumjohann and Treumann* [1996].

Generally the photoionisation dominates the production of the ionosphere. However, another production process becomes important at high magnetic latitudes, where

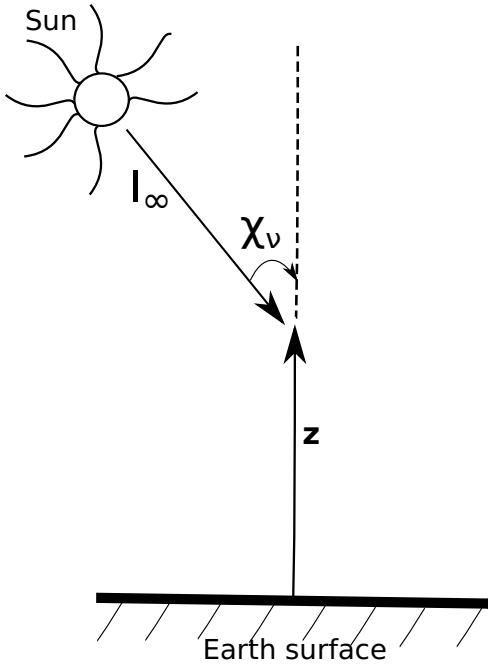

Figure 2.2: Illustration of the solar flux/radiation intensity I_∞ incident at an altitude z with the solar zenith angle χ_ν.

the Earth's magnetic field traces to the locations where dynamic magnetospheric processes associated with the interaction with the solar wind occur. At these latitudes, the ionisation by the energetic particle precipitation via solar wind-magnetosphere coupling, becomes an important ionization source. However, even with reduced solar UV radiation, when the solar zenith angle is greater than 90°, measurements of plasma parameters in the polar ionosphere have suggested that solar EUV radiation is still the dominant source of ionization due to transport from lower latitudes [e.g., *Vontrat-Reberac et al.*, 2001].

Solar Wind-magnetosphere coupling

Energetic, charged particles continuously stream from the Sun at high speeds, as plasma attached to the interplanetary magnetic field (IMF). Part of this solar wind energy is precipitated into the Earth's upper atmosphere via magnetic reconnection at the dayside magnetopause and in the magnetotail on the nightside [*Dungey*, 1961] as illustrated in Figures 2.3 and 2.4. The dayside here refers to the part of the Earth that faces the Sun, while nightside refers to the part of the Earth facing away from the Sun. For southward IMF orientation, magnetic reconnection opens the closed geomagnetic field

lines at the Earth's dayside magnetopause at point a) in Figure 2.3, and closes the opened magnetic field lines in the magnetotail on the nightside at point e). This gives rise to convection of plasma and magnetic flux forming a convection pattern known as the Dungey cycle, which was first described by *Dungey* [1961]. Magnetic reconnection occurs at points where the magnetic field lines are anti parallel, like points a) and e) in Figure 2.3 and point x) in Figure 2.4. At the dayside magnetopause, this happens at low latitudes for southward oriented IMF as illustrated in Figure 2.4a, and at high latitudes for northward oriented IMF orientation as illustrated in Figures 2.4b and c) [e.g., *Frey et al.*, 2003; *Fuselier et al.*, 2002]. Magnetic reconnection enables particle energy, momentum, and mass transfer from the solar wind to the Earth's magnetosphere and ionosphere. The rate of energy transfer changes depending on the variability of the solar wind parameters and the IMF intensity and orientation [*Sandholt et al.*, 2002].

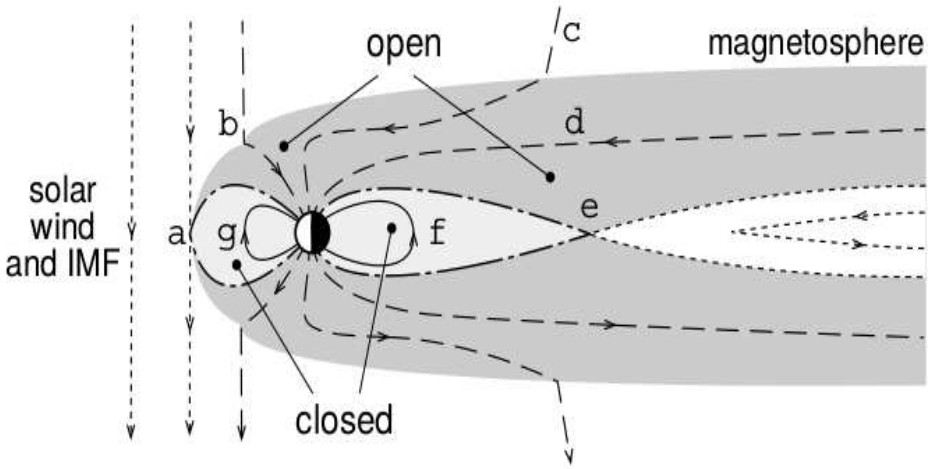

Figure 2.3: A schematic diagram of the magnetosphere in the noon-midnight meridian. The solar wind and IMF impinge from the left, IMF field lines represented by dotted curves. Full and dashed curves show closed and open field lines, respectively. The dot-dashed lines indicate the open/closed field line boundary, the ionospheric projection of which is the polar cap boundary. Letters a) to g) indicate the time evolution of field lines during the Dungey cycle. Figure and illustration from *Milan et al.* [2003].

The coordinate system and the Russell-McPherron effect

Throughout this thesis, we use the Geocentric Solar Magnetic (GSM) coordinate system [e.g., *T. Russell*, 1971] to define the orientation of the magnetic field **B**. The x-axis refers to the direction toward the Sun from the Earth, the z-axis, pointing northward, lies in the plane normal to the x-axis along the projection of the geomagnetic dipole

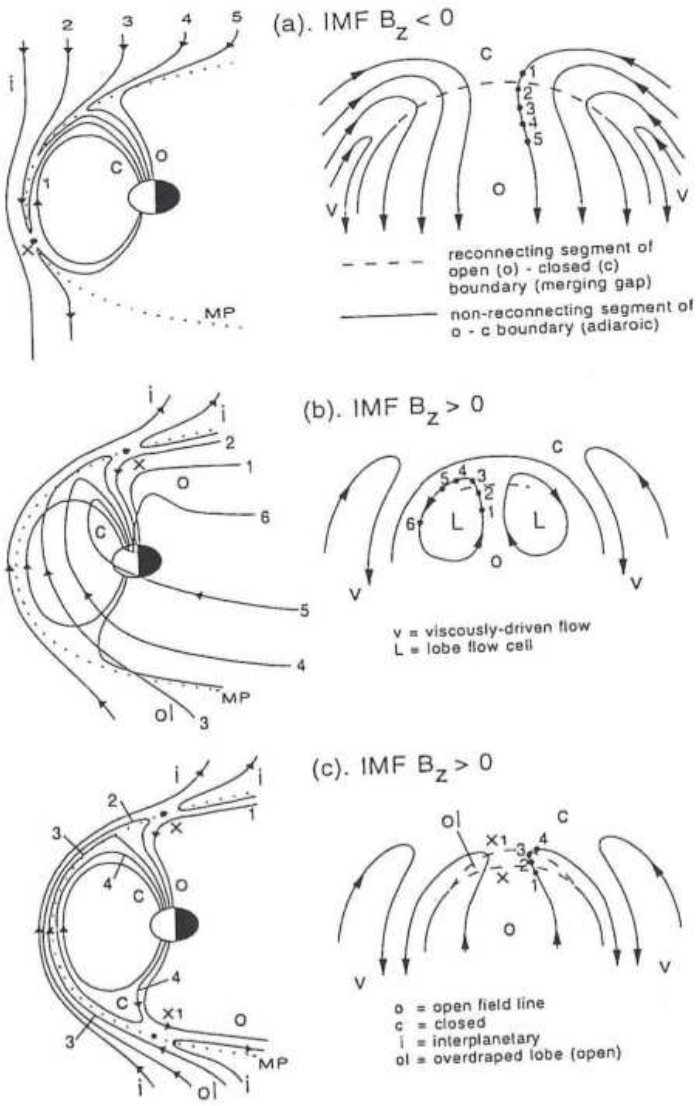

Figure 2.4: A schematic illustration of (left) the time evolution of reconnected field lines in the magnetosphere, as seen from the dusk view and (right) the corresponding flow in the northern hemisphere for magnetopause reconnection during (a) southward IMF, (b) northward IMF in the northern lobe only, and (c) northern IMF reconnecting both in the northern and southern lobes [*Lockwood*, 1998; *Sandholt et al.*, 2002]. Figure from *Sandholt et al.* [2002].

axis in this plane, while the y-axis points westward toward dusk. Therefore, southward IMF refers to $\mathbf{B}_z < 0$ while northward IMF refers to $\mathbf{B}_z > 0$. The x- and z-axes, and consequently the $\mathbf{B}_y$ and $\mathbf{B}_z$ components of the IMF, vary annually due to the changing in-

clination of the Earth's geographic pole with respect to the Earth-Sun line as illustrated in Figure 2.5. This in turn leads to variations in the GSM $\mathbf{B}_y$ and $\mathbf{B}_z$ IMF components due to the rotation of the Earth's geomagnetic pole about the geographic pole [e.g., *Aruliah et al.*, 1996, and references therein]. *Russell and McPherron* [1973] proposed that the changes in the orientation of the Earth' magnetosphere with respect to the IMF play an important role in the variation of the solar wind-magnetosphere coupling. This hypothesis is known as the Russell-McPherron (R-M) effect. According to the R-M effect, the solar wind-magnetosphere coupling is expected to peak during equinox, but be at the minimum during solstice [e.g., *Russell and McPherron*, 1973; *Zhao and Zong*, 2012]. The R-M effect has also been suggested as the reason for equinoctial asymmetry, sometimes seen in the seasonal variations of some aspects at high latitudes [e.g., *Aruliah et al.*, 1996].

The polar cap and the cusp

The area in the ionosphere which is penetrated by the open magnetic field lines defines the polar cap [*Siscoe and Huang*, 1985]. The region where the solar wind particles have direct access to the Earth's upper atmosphere, allowing direct particle energy transfer on the dayside via magnetic reconnection, is known as the cusp. The polar cap expands and contracts depending on the total amount of open magnetic flux, which is affected by magnetic reconnection on the dayside and nightside [e.g., *Cowley and Lockwood*, 1992; *Milan et al.*, 2003; *Siscoe and Huang*, 1985]. The polar region of the ionosphere is the focus of this thesis.

Energetic particle precipitation

Particles of different energies precipitate along the magnetic field lines into the ionosphere as a result of the solar wind-magnetosphere coupling. Particles of different energy deposit their energy at different altitudes. This thesis focuses on electrons. Figure 2.6 shows altitudes where different electron energies are deposited in the ionosphere. Higher-energy particles penetrate deeper into the ionosphere, and therefore deposit most of their energy at lower altitudes ($<$200 km), whereas the lower-energy (soft $\sim$ 100 eV) particles are stopped at higher altitudes, where they deposit their energy. The soft electrons deposit most of their energy between 300 and 400 km [e.g., *Mantas and Walker*, 1976].

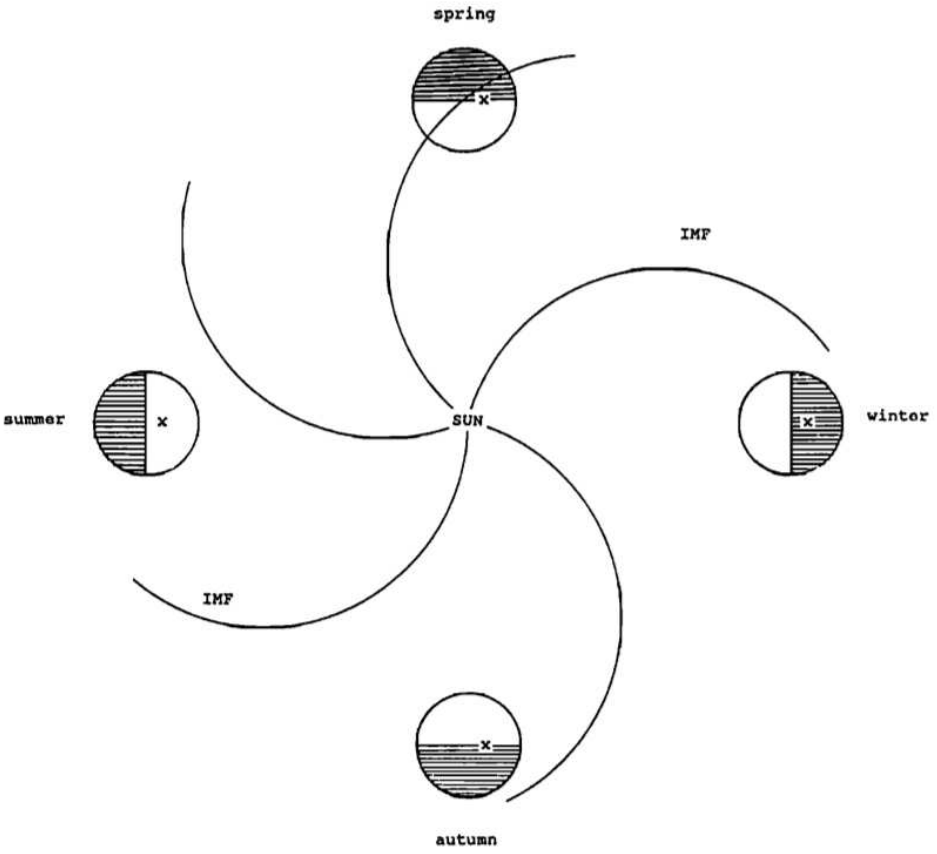

Figure 2.5: View of the ecliptic plane illustrating the average orientation of the IMF vector and position of the Earth's geographic pole (X) at the solstices and equinoxes [*Aruliah et al.*, 1996].

As the energetic electrons precipitate down along the magnetic field line, they can lose energy in three ways:

1) Impact ionisation of the neutral atmosphere, contributing to the production of the ionosphere.

2) Excitation of the neutral atmosphere leading to auroral optical emissions.

3) Heating of ambient electrons in the ionosphere via Coulomb collisions.

Processes 1) and 2) will be discussed briefly, starting with 1), which is a production source of the ionosphere. The third process, heating of ambient electron gas, is the focus of this thesis, and will be discussed in more detail.

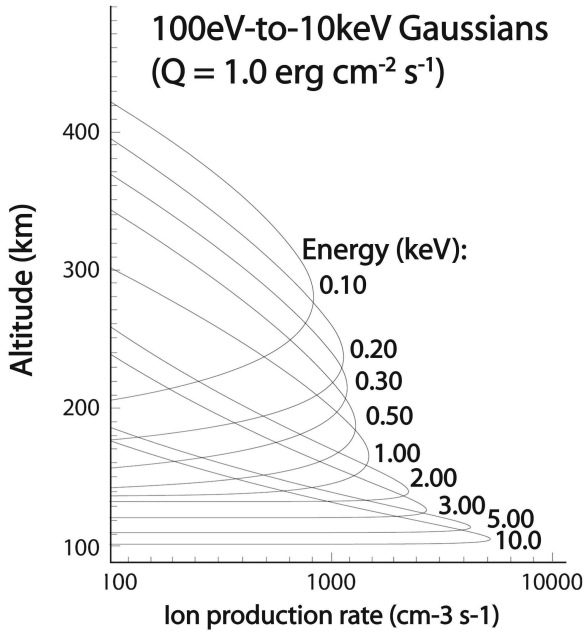

Figure 2.6: Total ion production rate for different precipitating energies for the same incident particle flux with energy 0.1-10 keV. Highest energy is deposited where the highest ion production rate is achieved. Figure from *Carlson et al.* [2012].

For a precipitating electron to ionise a neutral particle in the ionosphere, it should have energy greater than the ionisation threshold energy, which is the energy required to extract an electron from a neutral particle. Therefore, the more energy the precipitating particle has, the more electron-ion pairs it is likely to produce at the altitude where it is stopped. In the same format as the Chapman production function described earlier, the impact ionisation rate per unit volume at a given altitude, $Q_e(z)$ is given as:

$$Q_e(z) = \kappa_e F_e E_{ion} \sigma_n n_o \exp(\frac{-z}{H}) \tag{2.2}$$

where;

$\rightarrow \kappa_e$ is the impact ionisation efficiency

$\rightarrow F_e$ is the flux of the precipitating electrons

$\rightarrow E_{ion}$ is the ionisation energy

$\rightarrow \sigma_n$ is the neutral particle cross-section

$\rightarrow$ H and n_o have the same definition as in Equation 2.1

For more details, the reader is referred to textbooks like *Baumjohann and Treumann*

[1996] or *Kivelson and Russell* [1995].

2.1.2 Ion loss processes

The produced ions and electrons in the ionosphere, undergo certain chemical reactions, through which they are either lost, or produce other ions. This happens either when:

1) Ions and electrons recombine back to neutral particles via
   $e + X^+ \rightarrow X + h\nu$
   or
   $e + XY^+ \rightarrow X + Y$

2) Electrons attach to neutral particles forming negative ions via
   $e + Z \rightarrow Z^-$

where e is the electron, X^+ and XY^+ are atomic and molecular ions, Z is a neutral particle, and $h\nu$ is an emitted photon [e.g., *Bates et al.*, 1939]. The balance between the production and loss rates in the ionosphere, results into formation of electron density regions in the ionosphere at different altitudes. The ionosphere is, therefore, divided into three regions (D, E, F), which vary with time of the day and solar cycle as shown in Figure 2.7. The altitude of focus in this thesis is 250-650 km, and therefore, the discussion herein will, to a large extent, be limited to the F-region.

2.2 Optical auroral emission

The second way via which precipitating energetic particle lose energy is excitation of neutral particles leading to emission of optical auroral emissions. Auroral emissions are usually observed at high latitudes. These optical auroral emissions may be spontaneous as precipitating electrons directly excite bound electrons, which relax to lower energy levels via emission of photons, or result from further chemical reactions as the particle energy drops, with emission of photons a long the way. Auroral emissions are therefore usually used to study the impact, dynamics and effects of the solar wind-magnetosphere coupling processes.

2.2.1 The auroral spectrum

Auroral emissions can occur at a number of different wavelengths, ranging from ultra-violet to infrared, depending on the energy transitions during the excitation. Of interest to this thesis, is the aurora in the visible spectrum, $\sim$390-700 nm. Depending on the

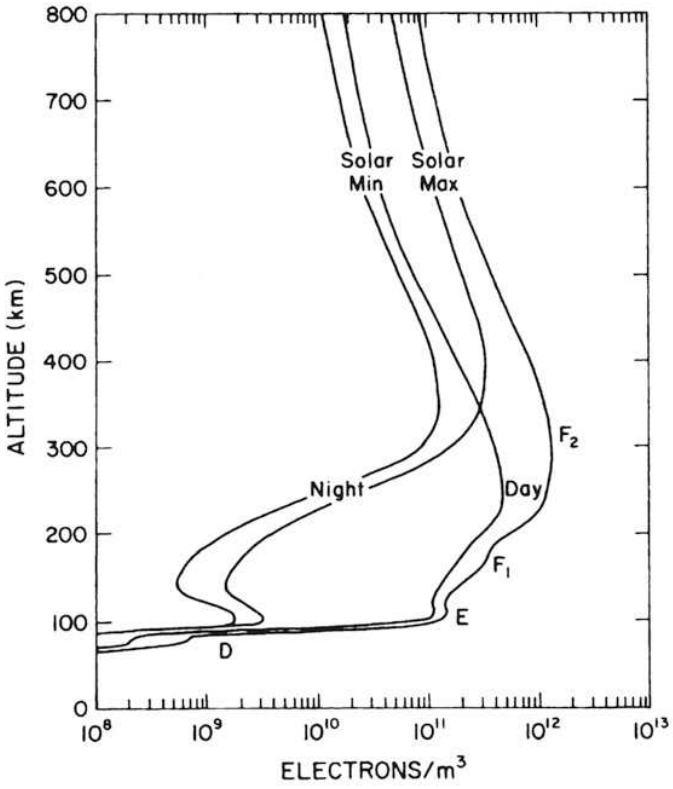

Figure 2.7: Typical ionospheric electron density regions with respect to altitude, for day and night, at solar maximum and solar minimum. Figure from *Brekke* [2013].

atmospheric constituent excited in the atmosphere, the auroral emission will either be a line at a specific wavelength, or a band spanning a few nanometres (nm). The atomic and molecular constituents will give rise to emission lines and bands, respectively. This thesis focuses on the emission lines.

The commonly observed auroral emission lines from ground, are the green-line at 557.7 nm wavelength and the red-line at 630.0 nm wavelength. Figure 2.8 shows a photograph of aurora taken from space, displaying the green and red auroral emissions. Both these emission lines arise from atomic oxygen excited states. The 557.7 nm and 630.0 nm are both forbidden atomic oxygen lines, where forbidden simply means that they defy quantum mechanics selection rule, and have a much longer lifetime than the $\sim 10^{-7}$s of permitted lines. The 557.7 nm line is emitted when an electron from the O(^{1}S) state (4.17 eV), relaxes to the lower energy O(^{1}D) state (1.96 eV), whereas the 630.0 nm line is emitted when an electron from the O(^{1}D) state relaxes to the

ground state, O(^{3}P), as illustrated in Figure 2.9. The lifetime of ∼0.8s and ∼110s that is indicated in brackets, for 557.7 nm and 630.0 nm emission, respectively, is the statistically probable time between excitation and natural relaxation by spontaneous emission of a photon [e.g., *Rees and Roble*, 1975; *Sandholt et al.*, 2002]. Because of the low excitation energy for the O(^{1}D) state, the 630.0 nm line characterises the soft electron precipitation, and is the most probable emission line at high altitudes, where low energies are deposited, and collisional quenching is infrequent (see also section 2.2.3). Direct impact excitation by soft electrons produces O(^{1}D) and O(^{1}S) in a ratio of ∼14:1, nearly independent of the energy of the incident electrons [*Mantas and Walker*, 1976]. The O(^{1}D) state can also result from low energy processes like thermal excitation. The 630.0 nm line has also been reported to be the dominant auroral emission on the dayside and in the polar region ionosphere. In this thesis, we use the 630.0 nm emission line as a proxy for ambient electron cooling via thermal excitation in the polar F-region ionosphere, which is the main topic for this thesis. Therefore, the discussion herein, will be limited to the 630.0 nm line.

Figure 2.8: A photograph of aurora taken from the International Space Station on June 26th 2017. The low energy red-line aurora is seen at higher altitude than the green-line emission. The high altitude red-line aurora is the focus of this thesis. Image Credit : NASA

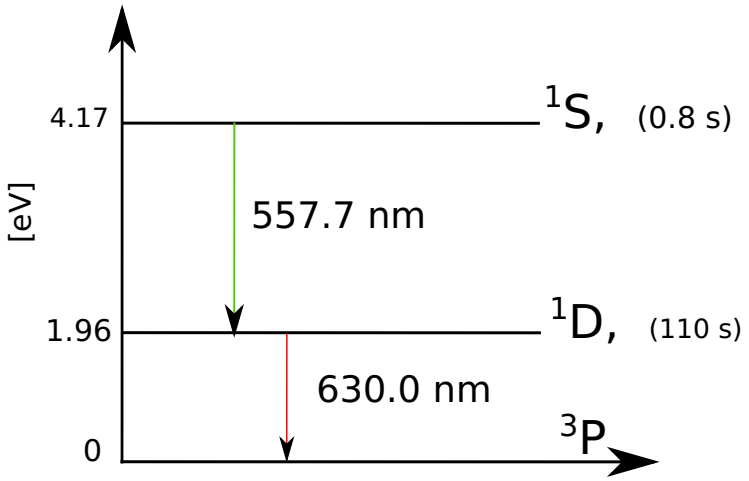

Figure 2.9: Illustration of the energy level transitions in the oxygen atom leading to emission of photons at the 557.7 nm and 630.0 nm wavelength. The associated radiative half-lives are indicated in brackets.

2.2.2 Sources of the 630.0 nm emission

One energy transfer reaction that can lead to emission of the red-line includes electron impact

$$e + O(^3P) \rightarrow e' + O(^1D) \tag{2.3}$$

$$O(^1D) \rightarrow O(^3P) + h\nu_{630.0nm} \tag{2.4}$$

where e is either a primary precipitating or secondary electron and e' is the secondary electron with lower energy, $O(^3P)$ is the ground state of atomic oxygen, from which a bound electron is excited to the O(^1D) state. O(^1D) relaxes, back to the ground state, via emission of a photon at 630.0 nm wavelength [e.g., *Rees et al.*, 1967].

The chemical reactions that can lead to this energy exchange reaction above include:

1) Direct electron impact excitation of atomic oxygen (to O(^{1}D) state) by precipitating electrons [e.g., *Meier et al.*, 1989].

2) Dissociative recombination of O_2^+ ions [e.g., *Rees et al.*, 1967]

$$O_2^+ + e \rightarrow O + O \tag{2.5}$$

It is assumed that the relative production of O_2^+ is proportional to the relative number density of O_2 [e.g., *Rees et al.*, 1967], and therefore this process will

be assumed negligible above 250 km, where the molecular oxygen number density is negligible (see Figure 2.1). It will also be associated to the hard electron precipitation which deposits energy at lower altitudes, in the E-region.

3) Excitation of atomic oxygen by thermal electrons in the high energy tail of the electron energy distribution. This occurs when the ambient electron gas is heated to high temperature, such that it cools by excitation leading to production of the O(^{1}D) state [e.g., *Carlson et al.*, 2013; *Lockwood et al.*, 1993; *Wickwar and Kofman*, 1984]. Emissions from this process are the main focus of this thesis.

Another energy exchange reaction, leading to emission of the 630.0 nm line, is the production of O(^{1}D) due to cascading (from the O(^{1}S) state) through the emission of the 557.7 nm:

$$O(^1S) \rightarrow O(^1D) + h\nu_{557.7nm} \tag{2.6}$$

2.2.3 Quenching of O(^{1}D)

The O(^{1}D) has a long lifetime of ∼110 s, compared to the ∼0.8 s for O(^{1}S). Due to this long lifetime, the O(^{1}D) is susceptible to collisional quenching before it is able to emit the 630.0 photon. Molecular nitrogen N_2 is believed to be the dominant quenching element for the O(^{1}D) [e.g., *Link et al.*, 1981]. However, the N_2 number density dominates at low altitudes, below ∼250 km (see Figure 2.1), and decreases with increasing altitude. Therefore, the O(^{1}D) is greatly quenched below ∼250 km [e.g., *Rees et al.*, 1967, and references therein]. Above ∼250 km, the quenching is greatly reduced and the loss of the O(^{1}D) via radiation of the 630.0 nm photon dominates [e.g., *Link and Cogger*, 1988]. Since this thesis focuses on the altitude range above 250 km, we thus ignore quenching.

2.2.4 Dayside versus nightside auroral emissions

The intensity of the auroral emissions varies with respect to the precipitating particle flux and energies. The emissions are observed at all magnetic local times (MLTs) , and the region where aurora is displayed is called the auroral oval. A statistical study by *Xiong et al.* [2014] showed that the boundaries of the auroral oval have no dependence on solar EUV flux and season. On the other hand, auroral oval boundaries have been shown to expand and contract with respect to magnetic activity [e.g., *Akasofu*, 1964; *Feldstein and Starkov*, 1970; *Hardy et al.*, 1985; *Johnsen and Lorentzen*, 2012; *Johnsen*

et al., 2012; *Xiong et al.*, 2014]. Figure 2.10 shows the location of the auroral oval during different magnetic activity levels, at different MLTs and magnetic latitudes. Note the variation of the boundaries, especially the equatorward boundary, which expands equatorward with increasing magnetic activity.

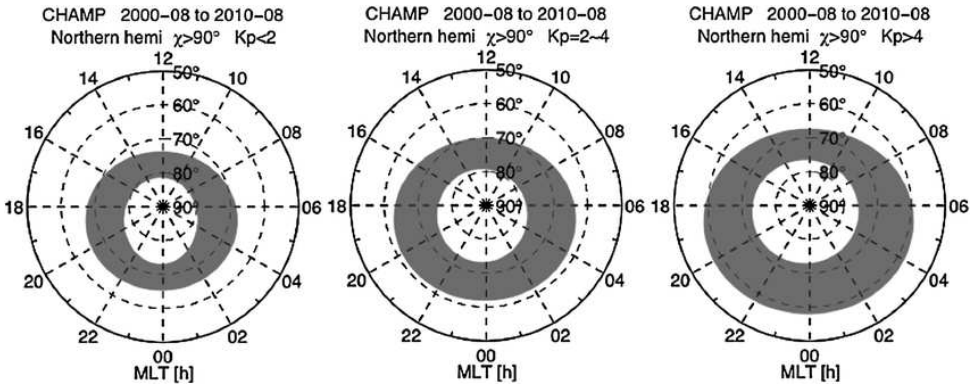

Figure 2.10: Magnetic latitude and local time distribution of the auroral oval (gray shading) for three different magnetic activity level conditions in the northern hemisphere: quiet, medium and active from left to right, respectively (*Lühr et al.* [2017] and *Xiong et al.* [2014]).

The dayside is the part that faces the Sun (06-18 MLT), while that facing away from the sun is the nightside (18-06 MLT)). As seen in Figure 2.10, the dayside auroral oval is located at higher magnetic latitudes than the nightside. The ionospheric measurements used in this thesis, are at a magnetic latitude of 75.12°N. From Figure 2.10, our measurements are most likely within the dayside auroral oval, and in the poleward boundary of the nightside part of the auroral oval. The polar cap boundary is believed to be co-located with the open/closed magnetic field line boundary, which is taken to be the equatorward boundary of the red dominated emissions in the dayside oval [e.g., *Johnsen and Lorentzen*, 2012; *Johnsen et al.*, 2012; *Lorentzen et al.*, 1996], and on the poleward boundary of the auroral oval on the nightside [e.g., *Blanchard et al.*, 1995]. Hard particle precipitation dominates on the nightside, mainly arising from magnetotail reconnection, and it is dominated by 557.7 nm auroral emissions. On the other hand, soft particle precipitation dominates on the dayside, mainly associated with the dayside magnetopause reconnection, and dominated by the 630.0 nm emission. The difference in the precipitation energies is attributed to the different plasma sources in the magnetosphere like magnetosheath for cusp and the central plasma sheet for the nightside precipitation [e.g., *Newell et al.*, 2004, and references therein].

Some phenomena in the dayside auroral oval have been identified as ionospheric signatures of flux transfer events (FTEs) or magnetic reconnection events at the dayside magnetopause [e.g., *Milan et al.*, 2000]. Poleward moving auroral forms (PMAFs) , in optical observations and radar measurements, are believed to be the visible ionospheric signatures of FTEs [e.g., *Oksavik et al.*, 2004, 2005; *Southwood*, 1987]. These features have also been reported during thermally excited emissions [e.g., *Carlson et al.*, 2013]. The PMAFs have been reported to vary with solar wind parameters and IMF configuration [e.g., *Fasel*, 1995], and therefore, they are an indicator of the dayside magnetic reconnection variation with solar wind and IMF activity. *Sandholt et al.* [1998] categorised the auroral features and motions at different MLTs and magnetic latitudes for the different IMF B_z and B_y conditions or configurations on the dayside.

2.3 Thermally excited emissions in the polar ionosphere

In this section, we introduce the main topic of this thesis, the thermally excited emissions, in a more detailed manner. As mentioned in the previous sections, precipitating energetic electrons lose some of their energy to the ambient electron gas via Coulomb collisions on their way through the ionosphere. This process acts to heat the ambient electrons, and is therefore important in the cusp and polar ionosphere, where energetic particle precipitation prevails. At the onset of electron precipitation into the ionosphere, the ambient electron gas temperature will start increasing at a rate dependent on the incident electron flux [*Lockwood et al.*, 1993]. An intense flux of electron energy of order of tens of electron volts, could initiate electron temperature increase at a rate of $\sim$1000 K per minute [*Lockwood et al.*, 1993].

Other ways in which the ambient electron gas can be heated in the ionosphere, like the solar EUV radiation, dissociative recombination and perpendicular electric fields, are discussed by *Schunk and Nagy* [1978]. The former process, heating due to perpendicular electric fields, arises from magnetic field-aligned (Birkeland) currents (FACs) , formed in response to the stress exerted on the magnetosphere by the solar wind [e.g., *Le et al.*, 2010; *Potemra et al.*, 1987]. The resulting electric field acts to drive ions and electrons up against the neutrals leading to frictional or Joule heating of the ions which try to follow the neutrals. The ratio of the electron to ion heating from Joule heating, is approximately proportional to the electron/ion mass ratio, and therefore most of this heat goes to the ion gas [*Schunk and Nagy*, 1978], which is not our focus.

The electron temperature to which the ambient electron gas is heated in the polar region ionosphere, is dependent on both the heating and cooling rates [e.g., *Sandholt et al.*, 2002]. We have so far discussed the possible ambient electron gas heating processes in the polar ionosphere. We now discuss how thermal balance is achieved in the ionosphere, and the processes that contribute to the cooling of the heated ambient electron gas. Normally, at low altitudes (<200 km), the electron gas generally cools by direct collision with the neutral gas and by collisions with the ion gas at high altitudes [e.g., *Schunk and Nagy*, 1978]. Therefore, generally, the electrons carry most of the initial energy, and pass it on to the other species [e.g., *Sandholt et al.*, 2002]. Only when Joule heating intensifies, does the heat flow in the reverse direction from ions to the cooler electrons. However, Joule heating mainly peaks at altitudes below 250 km, and therefore is considered negligible at the altitude of interest for this thesis.

Our focus is on the electron temperature above 250 km, where the electron gas is expected to be in good thermal contact with the ions. The cooling of electrons to ion gas is proportional to the number density of electrons, times the number density of ions. Since the number of electrons is assumed to be approximately equal to the number of ions (charge neutrality, $N_i \approx N_e$) in the ionosphere, this cooling rate is proportional to the square of the electron density (N_e^2). Specifically, cooling to ions is considered to be unimportant for $N_e << 3\times10^{11}$ m^{-3} but dominant otherwise [e.g., *Lockwood et al.*, 1993]. However, if the electron gas is heated at a much faster rate than the electron-ion collision rate, the electron gas may lose thermal contact with the ion gas, and thermal balance may then be achieved at higher electron temperatures, close to and above 3000 K [e.g., *Carlson et al.*, 2013; *Kozyra et al.*, 1990, 1997; *Lockwood et al.*, 1993]. At such high temperature levels, a third cooling rate becomes important, the cooling via excitation of the lowest excited state of atomic oxygen O(^{1}D), leading to 630.0 nm emissions [e.g., *Lockwood et al.*, 1993; *Meier et al.*, 1989; *Wickwar and Kofman*, 1984]. Such excitation of 630.0 nm emissions is strongly temperature dependent. The question put forward by *Lockwood et al.* [1993] is whether we should expect a sufficiently high electron temperature at an altitude where sufficiently large atomic oxygen concentration exists, such that the rate of collisional excitation of O(^{1}D) will lead to 630.0 nm emissions with kilo Rayleigh (kR) intensities. The unit Rayleigh is defined as the column emission rate of 10^{10} photons per square meter per column per second [*Hunten et al.*, 1956].

Some previous studies on thermal excitation in the cusp and polar region ionosphere

Some studies [e.g., *Gault et al.*, 1981; *Link et al.*, 1983] neglected thermal excitation in the analysis of dayside optical auroral emission, because they considered it unimportant. However, *Wickwar and Kofman* [1984], using the Søndrestrøm Incoherent Scatter Radar measured sufficiently high electron temperatures to excite 630.0 nm emission ($\sim$3000-4200 K), which coincided with enhanced electron densities ($\sim$(5-8)$\times 10^{11}$ m^{-3}), at high magnetic latitudes (74-78°N). From calculations based on the radar measurements, they found thermal excitation to contribute a significant intensity (up to $\sim$7 kR) to the 630.0 nm emission, which could be detectable by optical instruments, but they did not have any optical observation. Their line-of-sight integrated intensities from both thermal excitation and dissociative recombination are shown in Figure 2.11. They reported a peak emission altitude of $\sim$350-400 km and measurements were from $\sim 14{:}23 - 14{:}28$ MLT.

Another more recent thermal excitation study which involved measurements, was by *Carlson et al.* [2013]. They measured enhanced electron temperatures ($>$ 3000 K) which they found to show strong contribution of thermal excitation at altitudes $\sim$300-600 km. The coincident electron densities were $\sim$(3-6)$\times 10^{11}$ m^{-3}. Unlike *Wickwar and Kofman* [1984], they had ground-based 630.0 all-sky imager data, which, using time/space agreement, matched with the calculated volume emission rate, and the best match at altitudes $\sim$400-450 km which they reported as the peak emission altitude. Results from one of their case studies are shown in Figure 2.12, showing the electron temperature measurements, calculated volume emission rate, electron density, and all-sky images.

While investigating the OCB using 630.0 nm emission in the cusp, *Johnsen et al.* [2012] modelled the volume emission rate from thermal excitation, separating the airglow and the direct impact excitation part. They found that the volume emission rate varied with solar cycle, electron temperature T_e , maximum electron density in the F region (nF2) , and the height of maximum electron density (hF2) . Their modelled volume emission rates are shown in Figure 2.13. Their results showed that the there is no significant thermal excitation below 250 km, and that the volume emission rate increases toward solar maximum, and also increases with increasing electron gas temperature, and density.

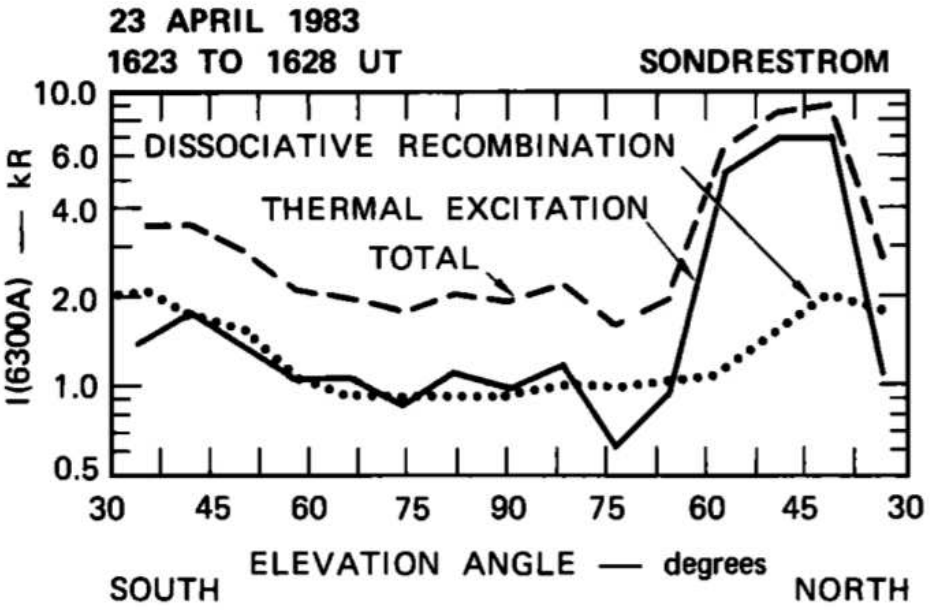

Figure 2.11: Line-of-sight integrated 630.0 nm intensities for thermal excitation and dissociative recombination from radar measurements by *Wickwar and Kofman* [1984]. Magnetic local time was ∼UT-2, therefore ∼14:23-14:28 MLT.

Generally, all these studies indicate that thermal excitation at the cusp and polar latitudes could be more important and frequent than generally anticipated, hence the motivation for the work in this thesis.

Typical thermal electron energy distribution in the ionosphere

The thermal electrons in the ionosphere are believed to typically have a Maxwellian energy distribution, where the population decreases exponentially with increasing energy. At electron temperatures close to or above 3000 K, there may be enough electrons in the high energy tail of the Maxwellian energy distribution, exceeding the $O(^1D)$ excitation energy level of 1.96 eV [e.g., *Mantas*, 1994]. A typical thermal electron Maxwellian distribution in the ionosphere, is shown in Figure 2.14, indicating the high energy tail responsible for excitation of $O(^1D)$. The steps leading to thermally excited emissions in the polar ionosphere are summarised in Figure 2.15.

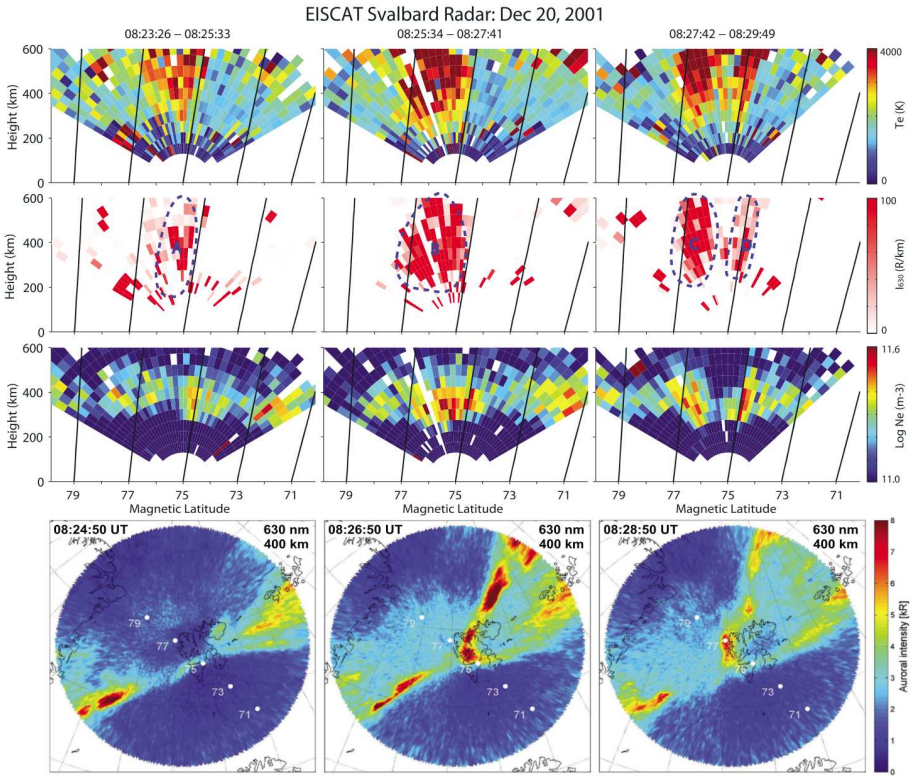

Figure 2.12: Measured electron gas temperature Te, derived 630.0 nm volume emission rate R/km, and measured electron density Ne, for 100–600 km altitude versus ∼70-80°magnetic latitude (top 3 rows), where each independent data point is a 3.2 s integration and the radar scans north-south along the magnetic meridian in a windshield wiper-like sweep of 128 s duration, and the bottom row shows the 630.0 nm all-sky images where the position of the latitude numbers 71, 73, 75, 77, 79 for the volume emission rate (second row) is superposed on the all-sky image. The observed brightening in the all-sky data matches the location of the derived thermal volume emission rate and the best fit is found at an altitude of ∼400-450 km [*Carlson et al.*, 2013].

Thermal electron impact excitation rate

Thermal electron excitation of O(^{1}D) has been suggested as the primary source of other 630.0 nm emissions such as stable aurora red arcs at mid-latitudes [e.g., *Kozyra et al.*, 1990], and 630.0 nm emissions observed in artificial ionosphere heating experiments [e.g., *Mantas*, 1994; *Mantas and Carlson*, 1991]. This thesis, however, focuses on the thermally excited 630.0 nm emissions in the polar region ionosphere. Over the past few decades, efforts have been made to calculate and measure the thermal electron impact excitation cross section [e.g., *Doering and Gulcicek*, 1989; *Henry et al.*, 1969; *Lan et al.*, 1972; *Shyn and Sharp*, 1986; *Smith et al.*, 1967; *Thomas and Nesbet*, 1975].

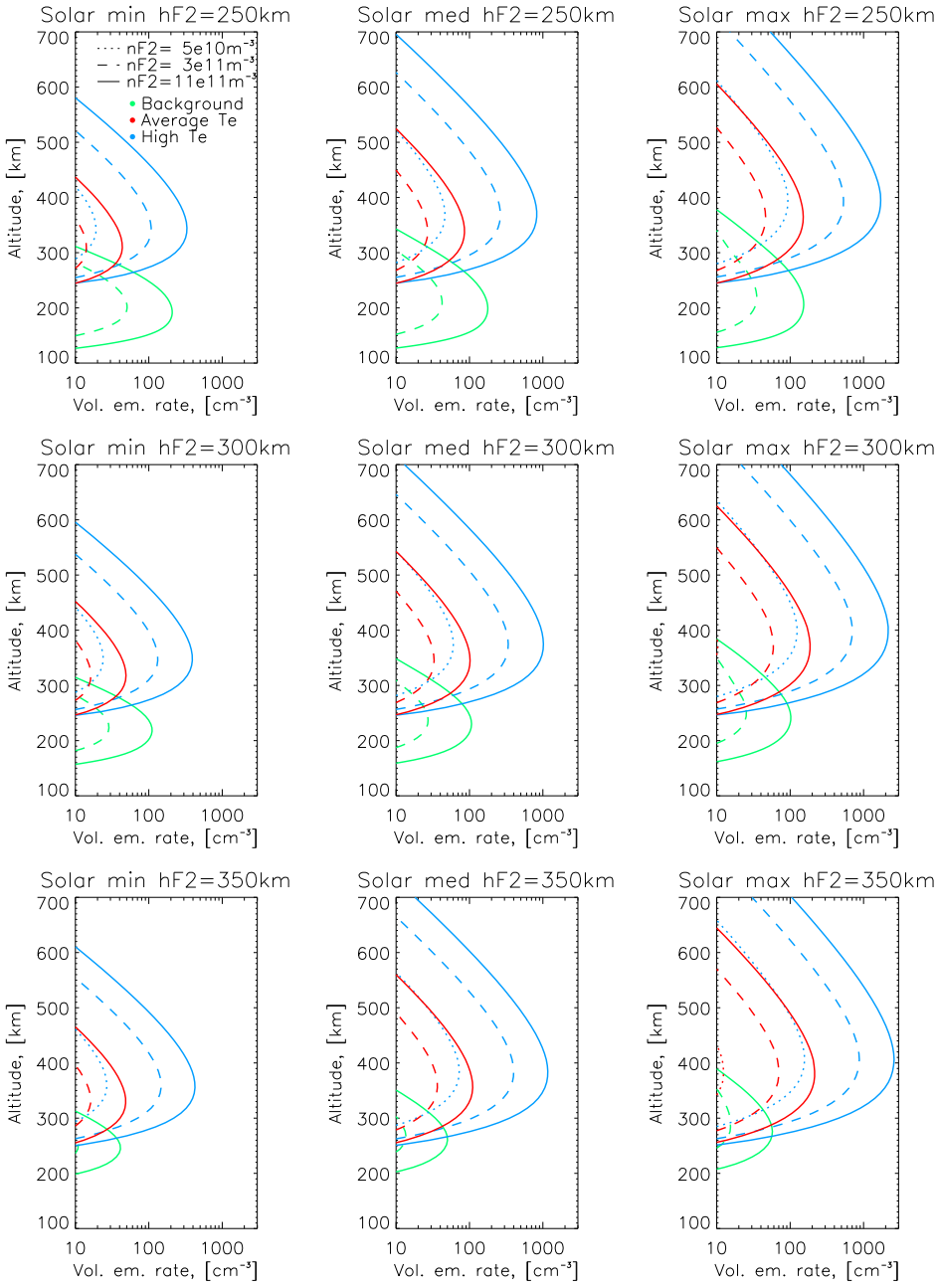

Figure 2.13: Modelled volume emission rate profiles of the 630.0 nm emission caused by background airglow (green curves) and excitation by thermal, ambient electrons (red and blue curves). The columns represent different stages of the solar cycle. The rows, from top to bottom, represent three different altitudes for the F-layer maximum [*Johnsen et al.*, 2012].

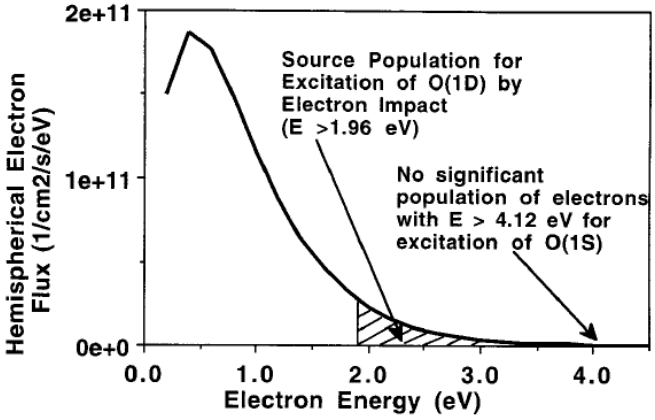

Figure 2.14: Thermal electron Maxwellian distribution typical of the ionosphere. The shaded region marks the population in the high energy tail, responsible for the thermally excited 630.0 nm emissions. Thermally excited emissions from higher energy levels like 557.7 nm, requiring energy >4 eV, are highly unlikely (*Kozyra et al.* [1997]).

Mantas and Carlson [1991] reassessed and compared the O(^{1}D) thermal excitation rate based on some of these cross-sections. A graphical representation of the excitation rates from their assessment is shown in Figure 2.16. This shows a strong dependence of the thermal excitation rate on the electron gas temperature. The steep increase of the excitation cross section with energy just above 2 eV, makes thermal electron impact component of 630.0 nm critically dependent on the electron gas temperature [*Lockwood et al.*, 1993]. As T_e increases from 2000 to 4000 K, the rate of O(1D) excitation increases by $2\frac{1}{2}$ orders of magnitude [e.g., *Lockwood et al.*, 1993; *Mantas and Carlson*, 1991]. From their assessment, *Mantas and Carlson* [1991] recommended using the thermal electron impact excitation rate based on the cross section by *Lan et al.* [1972],

$$\alpha(T_e) = 0.15 \times \sqrt{T_e} \times \frac{(8537 + T_e)}{(34191 + T_e)^3} \times e^{\left(\frac{-22756}{T_e}\right)} \quad (cm^3/s) \tag{2.7}$$

which they found to be most complete of the assessed cross sections.

Carlson et al. [2013] extended the result from *Mantas and Carlson* [1991], by suggesting cusp conditions when thermally excited emissions are likely to occur in the ionosphere, and provided a simple formula to calculate the altitude discriminated volume emission rate in Rayleigh/km,

$$I_{630}(h) = \alpha[T_e(h)] \times N_o(h) \times N_e(h) \quad (Rayleighs/km) \tag{2.8}$$

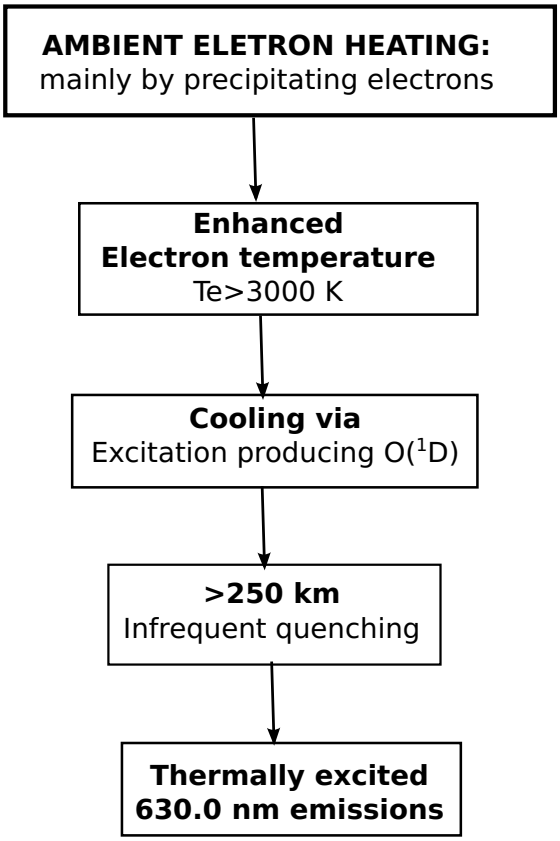

Figure 2.15: Processes leading to thermally excited emissions in the polar region ionosphere.

and line-of-sight integrated 630.0 nm intensity (kR)

$$I_{630} = \int_{250km}^{650km} I_{630}(h)dh \quad (Rayleighs) \tag{2.9}$$

where N_o and N_e are neutral and electron number density, measured in cm^{-3}, and T_e is the electron temperature in Kelvin. All the variables are functions of altitude (h) in kilometres. *Carlson et al.* [2013] presented Figure 2.17 as a guideline on the input parameter sensitivity on the 630.0 nm intensity derived from Equation 2.9, which showed T_e to have the greatest impact on the integrated intensity of thermal 630.0 nm emission and least sensitivity to N_e. We use Equations 2.8-2.9 in papers I, II and III, to derive the thermal component of the 630.0 nm emission. We apply these three formulae to incoherent scatter radar measurements, to calculate the intensity of thermally excited emissions. The data used in this thesis is described in the next chapter.

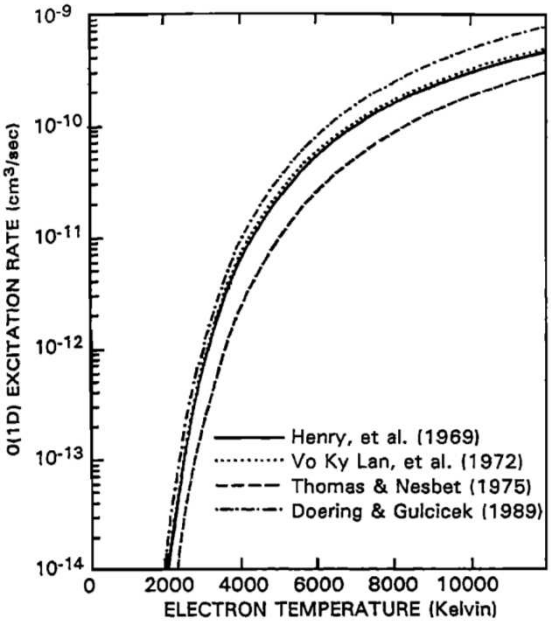

Figure 2.16: Thermal electron impact excitation rates of $O(^1D)$ for different electron temperatures [*Mantas and Carlson*, 1991].

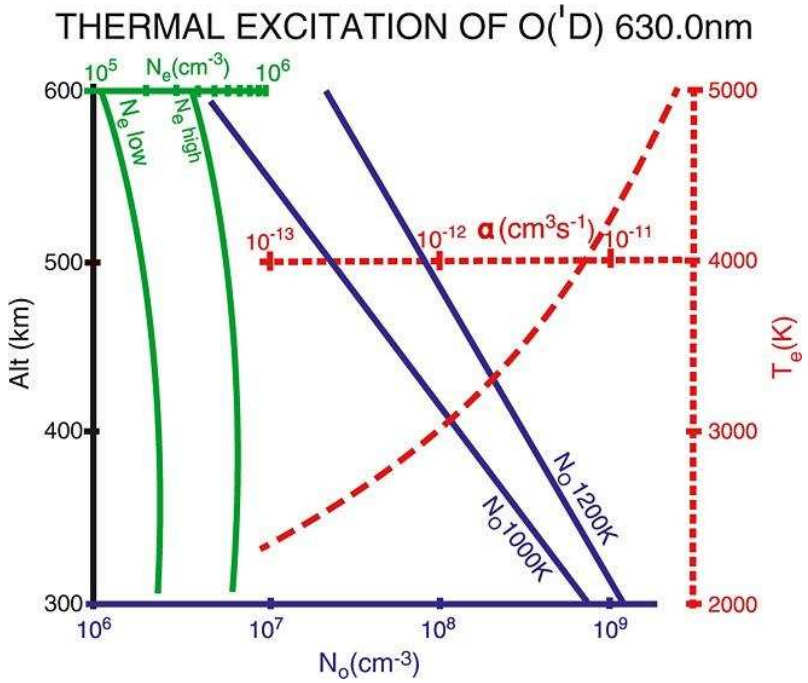

Figure 2.17: Thermal excitation of O(^{1}D) 630.0 nm parametric dependence on electron gas temperature T_e, electron density N_e, and atomic oxygen density N_o referenced to a standard model exospheric temperature. $\alpha(T_e)$, the O(^{1}D) thermal electron excitation rate (cm^3/s), is defined in Equation 2.7. With N_e, N_o, and $\alpha(T_e)$ all to the same scale for each order of magnitude change, this figure shows that the greatest input parameter sensitivity is to Te [*Carlson et al.*, 2013].

Chapter 3

Ground-based measurements and models

In this chapter, we describe the techniques and instruments used for the ionosphere measurements and optical observations in this thesis. They include ground-based meridian scanning photometer and the EISCAT Svalbard radar. In addition, the atomic oxygen density is a key requirement for the thermal excitation to occur. We have no measurements for the neutral atmosphere, so we used models to generate this density as described in this chapter. In all three papers, other data like solar wind, IMF, sunspot number, and solar F10.7 flux, were also used for interpretation of our results. For a description of these, the reader is referred to Papers I-III.

3.1 Ground-based measurements

3.1.1 Meridian Scanning Photometer (MSP)

The meridian scanning photometer (MSP) is an optical instrument which can record optical emission intensities along the magnetic meridian, at different desired wavelengths. The MSP at the Kjell Henriksen Observatory (KHO) on Svalbard is designed to measure optical emission intensities at five wavelengths; 630.0 nm, 427.8 nm, 557.7 nm, 486.1 nm, and 844.6 nm. The key wavelength used in this thesis, is the 630.0 nm.

The instrument is made up of a mirror, which rotates, scanning the sky from north to south along the magnetic meridian, hence the instrument's name 'meridian scanning photometer'. Each unit recording of a wavelength is referred to as a channel. Each channel consists of a photomultiplier tube, with a narrow bandpass filter for the desired wavelength, which is mounted onto a tilting frame. This unit is referred to as the tilting frame photometer, and is placed in front of the rotating mirror. A simplified illustration

of how a two-channel MSP works is shown in Figure 3.1. The MSP delivers optical emission intensity as a function of elevation angle, for the respective channels. It has a field-of-view of $\sim 1^\circ$ and takes 16 s to complete one meridian scan for the data used in this thesis, with a spectral resolution of 0.4 nm. The background intensity for each channel is obtained by tilting the filters from peak emission to an angle that transmits a wavelength representing the background emissions, which enables subtraction of the background [*Romick*, 1976]. The MSP is also absolutely calibrated in Rayleighs (R). For this reason, in Paper I, we are able to directly compare our calculated intensities in Rayleighs with the optical observations from the MSP. The MSP scans through the EISCAT Svalbard radar 42 m beam, which is fixed at an elevation of 81.6° from south.

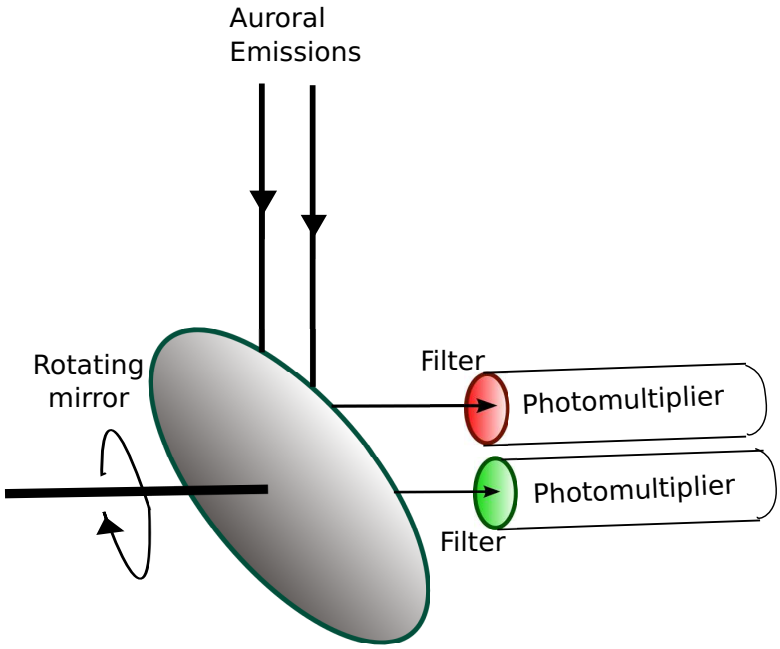

Figure 3.1: Illustration of how the meridian scanning photometer works. As the mirror rotates, it scans the sky along the magnetic meridian (north-south), collecting the auroral emissions. The incident auroral emissions are then transmitted through the filters, which allow only a specific wavelength to go through and be recorded by the photomultiplier. This figure shows a two-channel photometer, for red and green aurora. (Adapted from *Lorentzen and Egeland* [2011])

3.1.2 EISCAT Svalbard Radar (ESR)

EISCAT stands for European Incoherent SCATter, which is a scientific association currently operating incoherent radar systems near Tromsø (Norway), Sodankylä (Finland),

Kiruna (Sweden) and Longyearbyen (Svalbard). 'Radar' is an acronym for 'radar detection and ranging'. EISCAT is an international association supported by research organisations in China, Finland, Japan, Norway, Sweden, and the United Kingdom.

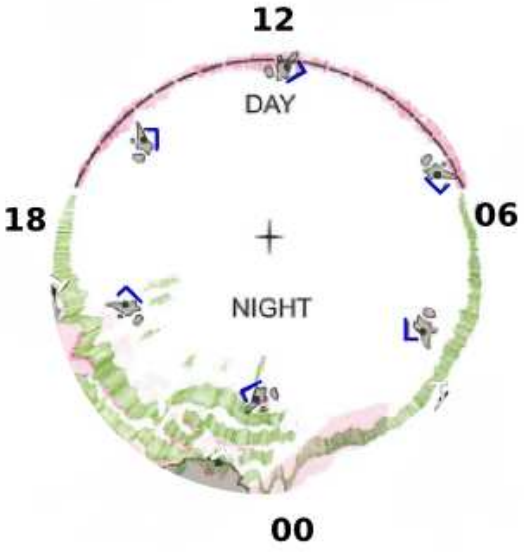

Figure 3.2: The position of Svalbard with respect to the auroral oval at different local times. L marks the location of Longyearbyen (Svalbard). (Adapted from *Lorentzen and Egeland* [2011] based on a figure by Willy Stoffregen).

Svalbard is located within the polar cap, most of the time, as illustrated in Figure 3.2. The figure shows the position of Longyearbyen (L) at Svalbard, with respect to the auroral oval at 6 different magnetic local times. This position makes Svalbard well suited for observation and studies of dynamics in the polar region ionosphere. We therefore use measurements from the EISCAT Svalbard Radar (ESR). ESR is located at Longyearbyen, Svalbard at geographic coordinates 78.15°N and 16.02°E, 75.12°N quasi-dipole magnetic latitude and magnetic local time $\sim$ UT+3. Such a high latitude makes optical observations possible on the dayside during winter, when the Sun is below the horizon.

ESR is located just 600 m north of KHO, favouring common volume measurements with optical instruments like the MSP. Figure 3.3 shows the measurement region for the MSP (black line) and ESR beam (red dot), used in this thesis. ESR consists of two antennae: a 32 m fully steerable parabolic dish and a fixed magnetic field-aligned 42

m parabolic dish. This thesis uses the field-aligned 42 m beam. The 42 m and 32 m antennae are shown in Figure 3.4. The ESR system operates at a frequency range of around 500 MHz, as a monostatic system, where both the transmitter and receiver are at the same location.

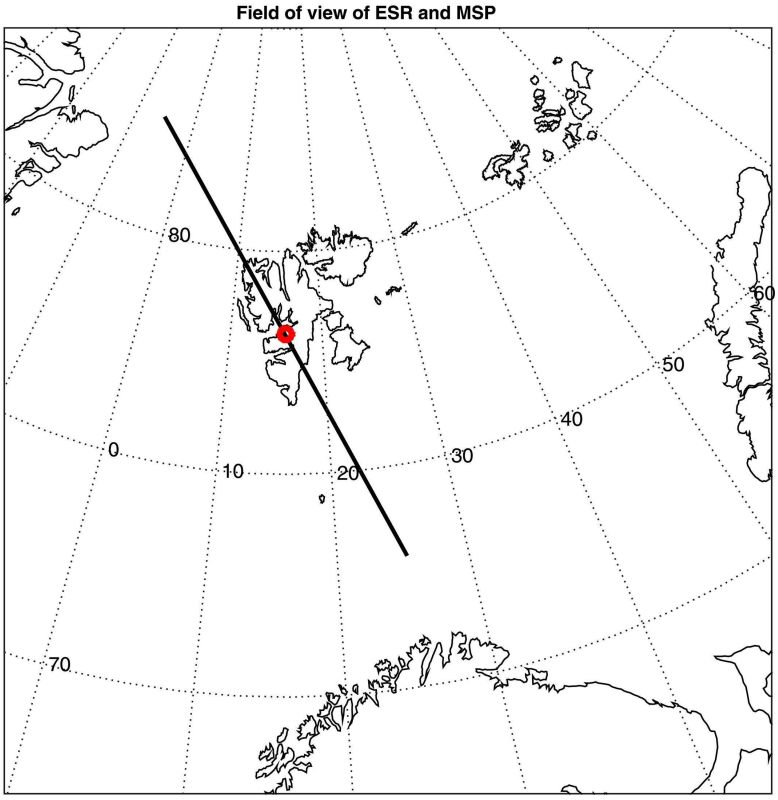

Figure 3.3: MSP (black line) and ESR 42 m (red dot) co-located measurement region. Figure from Paper I [*Kwagala et al.*, 2017].

Incoherent scatter from the ionosphere

A free charged particle has an effective distance beyond which it is shielded from the oppositely charged particles. This shielding layer is formed at a distance where the random thermal energy balances the electrostatic energy. In an ionized medium, like the ionosphere, free electrons will form a shielding layer of a radius called the Debye length, λ_D, around the ion, as illustrated in Figure 3.5. If a radio wave of a wavelength $\lambda_{radar} << \lambda_D$ is transmitted to the ionosphere, the scattering from individual free electrons shielding the ion, will be received back [e.g., *Gray and Farley*, 1973, and references therein]. However, if the transmitted radio wave is of a wavelength $\lambda_{radar} >> \lambda_D$

Figure 3.4: The EISCAT Svalbard Radar dishes, the fixed 42 m (left) and the steerable 32 m dish (right). Photo: Anja Strømme

a weak incoherent scattering from the cloud of free electrons shielding the ion is received back. Only very powerful and very sensitive radars, are capable of detecting the weak incoherent backscatter [*Gordon*, 1958]. This is the technique used by incoherent scattering radars (ISRs) like the ESR. More detailed information on the incoherent scatter theory is given by *Gordon* [1958].

Recieved ISR Power Spectrum

An important data product of the radar is it's Fourier transform equivalent, the autocorrelation function (ACF) that is generated through lagged product samples of the scattered signal, which is stored in a lag profile matrix [*Grydeland et al.*, 2004, 2008]. A power spectrum from a fairly well-defined and limited region of space is then formed from the lag profile matrix [*Grydeland et al.*, 2004, 2008]. A typical power spectrum from the ion gas, known as the ion line, is double humped as those shown in Figure 3.6. The characteristics of the power spectrum will depend on the plasma temperatures, ion composition and ion gas drift velocity, as illustrated in Figure 3.6. Typically measured parameters are electron density N_e, electron temperature T_e, ion temperature T_i and line-of-sight ion drift velocity V_i . A more detailed description of the coding schemes for ISR measurement are given by *Lehtinen and Huuskonen* [1996] and *Gry-*

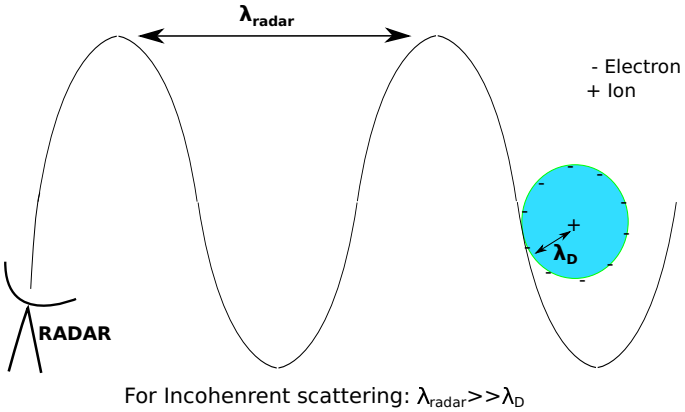

Figure 3.5: An illustration of the incoherent scattering technique used by the ESR. When the radar transmits a radio wave of wavelength λ_{radar}, which is much greater than the Debye length, λ_D, a weak incoherent scattering from the electron cloud that is surrounding an ion, is received back. The ion drifts with the cloud, which is measured by the radar as the line-of-site ion velocity.

deland et al. [2004, 2008].

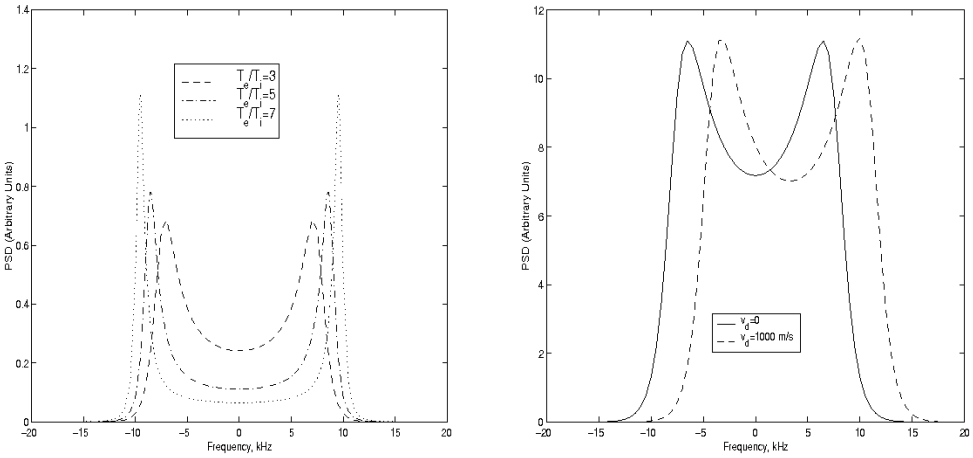

Figure 3.6: Typical power spectra for the ion line showing it's dependence on the electron temperature/ion temperature ratio T_e/T_i (left), and the effect of the plasma drift V_d (right). Figure from *Grydeland et al.* [2008].

The received radar signal also contains thermal noise from electronics and the surroundings, as well as clutter which is radar echoes from 'unwanted targets' (e.g., mountains, space debris) [e.g., *Turunen et al.*, 2000]. The signal-to-noise ratio (SNR) is the ratio of the instantaneous target signal power to the mean noise power. In the ESR

Table 3.1: An overview of EISCAT experiments used in this study. Table adapted from Paper II [*Kwagala et al.*, 2018]

			Raw Data		Processed Data	
Year	Experiment Name	Altitude coverage (km)	Time resolution (s)	Altitude resolution (km)	Time resolution (s)	Altitude resolution (km)
2000 - 2003	tau0	53 - 1144	6.4	3.0	64 - 128	3 - 37
2004 - 2006	steffe	34 - 800	6.0	2.2	60 - 120	3.7 - 30
2007 - 2015	ipy	28 - 383	6.0	2.2	60 - 120	3.7 - 30
		388 - 509		4.5		

system, the receiver noise is routinely monitored, producing accurate background estimates and making it possible to analyse even at very low SNR [*Wannberg et al.*, 1997]. A detailed description of the ESR is given by *Wannberg et al.* [1997].

ESR experiments

An experiment in our context refers to a set of instructions for the transmitters, receivers and digital signal processing units at the radar site. EISCAT experiments are categorised into common programs and special programs. The common programs are standardised experiments that run on a frequent basis, whereas special programs are experiments that are operated for a limited period to study specific science topics. The common programs are important for studying long-term variations and produce data coverage for statistical studies. Experiments mainly differ in space and time resolutions. Data used in the statistical studies in Paper II and Paper III are mainly from experiments called tau0, steffe, and ipy for the periods 2000-2003, 2004-2006, and 2007-2015, respectively, with time and altitude resolutions presented in Table 3.1. Since we use the fixed 42 m beam, data from all experiments can be used as long as they ran for approximately 24 hours. The tau0, steffe, and ipy are just the most common experiments in the respective periods. In Paper I, however, there was no restriction on the duration of experiments. The criterion for event selection, was the existence of the ionospheric condition approximately matching those suggested by *Carlson et al.* [2013] during which thermally exited emissions are likely to occur. The other condition was availability of optical observation of the same measurement volume as the ESR. The cases studied in Paper I, consist of a common program ipy experiment and a special program taro experiment. A more detailed overview of the EISCAT experiments can be found at the EISCAT website (`https://www.eiscat.se`).

ESR data analysis

A data analysis software tool called the Grand Unified Incoherent Scatter Design and Analysis Package (GUISDAP) is used to analyse the ESR data. It works by fitting theoretically calculated values to measured values [*Lehtinen and Huuskonen*, 1996]. The time resolutions of each experiment represents the shortest integration time of the sampled data, also called data dumps. This stage is also referred to as the pre-integration, and the result is stored as matlab mat files, which at this stage are called the raw data. The ISR measurements are highly based on the statistical accuracy, so GUISDAP also generates the variance of the data, which is the basis for the statistical error bars. For higher accuracy, longer integration times are used to include at least 10 raw data files, and such data products are referred to as the processed data. The processed data is usually what is available at the EISCAT Madrigal website. The longer the integration, the smaller the error bars, and therefore the higher the accuracy. However, for longer integration times, transient phenomena in the ionosphere are also likely to be averaged out. For this reason, one has to find a balance depending on the ionospheric dynamics one is studying. On this basis, we decided to use an integration time of $\sim$1-2 minutes in this thesis, as shown in Table 3.1 under the processed data specifications. We also note that GUISDAP does not fit the data if there is clutter. To improve the statistical accuracy only parameter measurements with error bars less than 25% are used in this study.

Limitation of fixed measurements

The fixed field aligned measurements enable longer integration times, like 1-2 min. However, the sweeping measurements like that used in *Carlson et al.* [2013] provide a wider spatial coverage. For example, Figure 3.7 shows derived thermal volume emission rates from *Carlson et al.* [2013]. Here the thermally excited emissions are shown to occur even outside the fixed field aligned beam (green line), both equatorward and poleward, or just move into or outside the field of view of the ESR fixed 42 m. This may be a source of bias in our dataset. However, the 3.2 s integration times required to map over an area of $\sim$600 km $\times$ 1200 km in $\sim$2 min led to large error bars in the study of *Carlson et al.* [2013].

The Naturally Enhanced Ion Acoustic Lines (NEIALs)

The GUISDAP analysis tool assumes that the ionospheric plasma is in thermal equilibrium and therefore has a Maxwellian distribution. However, distorted power spectra have sometimes been observed in EISCAT measurements, which have been attributed to non-Maxwellian velocity distributions [e.g., *Rietveld et al.*, 1991]. Such features

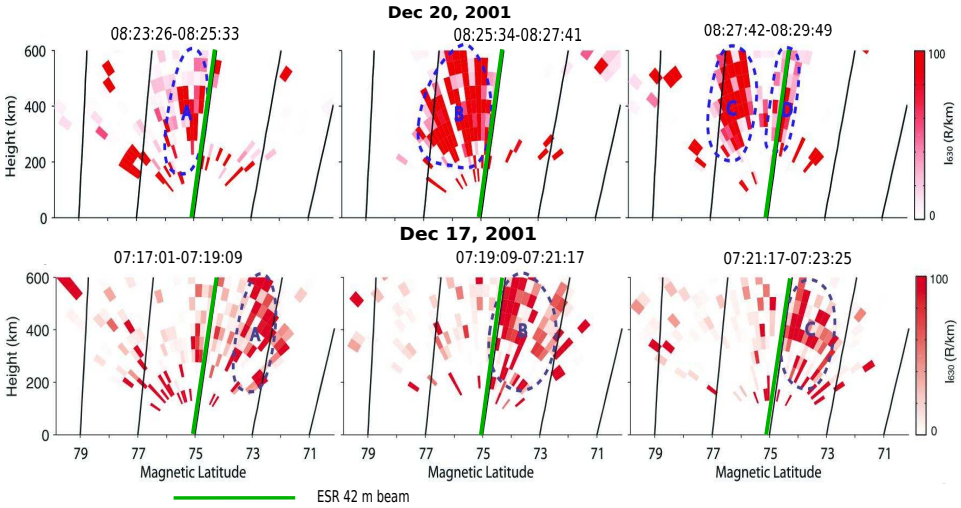

Figure 3.7: Volume emission rates of thermally excited emissions, in Rayleigh/km, calculated and presented by *Carlson et al.* [2013], based on the ESR 32 m beam scanning along the magnetic meridian, in the cusp region, on December 20th and 17th 2001, top and bottom panel, respectively. We have added the green line, to mark the location of the fixed field-aligned beam, which we use in this thesis. Figure adapted from *Carlson et al.* [2013].

have been referred to as naturally enhanced ion-acoustic lines (NEIALs) [e.g., *Collis et al.*, 1991; *Forme et al.*, 2001; *Foster et al.*, 1988; *Lunde et al.*, 2007; *Michell and Samara*, 2013, 2010; *Michell et al.*, 2009, 2014; *Ogawa et al.*, 2006]. GUISDAP fails in the presence of NEIALs. For this reason, sometimes the raw data has to be subjected to visual inspection. NEIALs may be seen in field-aligned measurements above $\sim$300 km, and are sometimes (but not always) detected by GUISDAP as clutter and not fitted. For this reason, for the case studies in Paper I, we visually inspect the raw data and eliminate the NEIALs. Since NEIALs are associated with enhancement of the typical power spectrum, they have been seen as extremely enhanced electron temperatures [e.g., *Foster et al.*, 1988; *Lunde et al.*, 2007]. A power spectrum during NEIALs enhancement is shown in Figure 3.8. In raw data, the NEIALs are identified as enhancements of either one or both shoulders of the ion lines as shown in Figure 3.9. As a precaution we eliminate any data with electron temperature exceeding 8000 K in Papers II and III. We however, believe that such cases will be averaged out in the statistical studies.

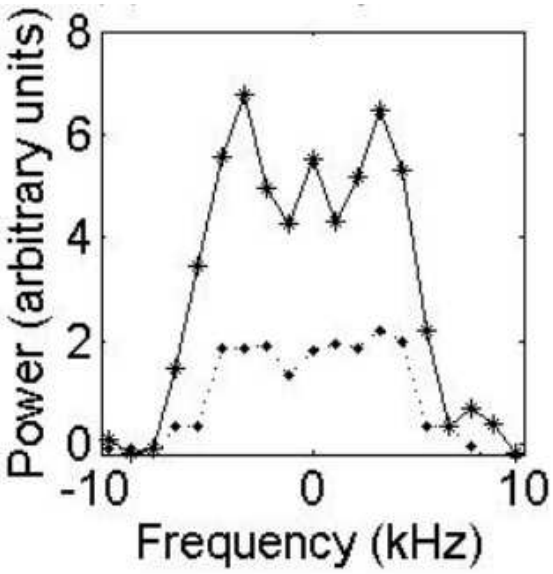

Figure 3.8: A power spectrum during a NEIALs enhancement (black line) and before the NEIALs enhancement (dotted line). Figure from *Michell et al.* [2009].

3.2 Neutral atmosphere models

The neutral atmosphere participates in the production of the thermally excited emissions, as it provides the source of the atomic oxygen to be excited. The measurements of the atomic oxygen are however very scarce and therefore models are usually used to generate the atomic oxygen density. The two models used in this thesis are described in this section.

3.2.1 NRLMSISE-00 model

NRLMISISE-00 is an acronym for the Naval Research Laboratory Mass Spectrometer and Incoherent Scatter 2000. The NRLMSISE-00 [*Picone et al.*, 2002] model is an empirical atmospheric model which extends from the ground to the exobase. The NRLMSISE-00 is the main source of the number atomic oxygen density used in this thesis. For almost three decades, the Mass Spectrometer Incoherent Scatter (MSIS-class) models have frequently been used for upper atmosphere studies. The NRLMSISE-00 is the most recent of the MSIS-class models. The model is based on a large database which includes ground-, rocket-, and satellite-based measurements extending up to year 1997 [*Picone et al.*, 2002]. The model is a statistical average with improved data coverage of more locations and dynamics than earlier models.

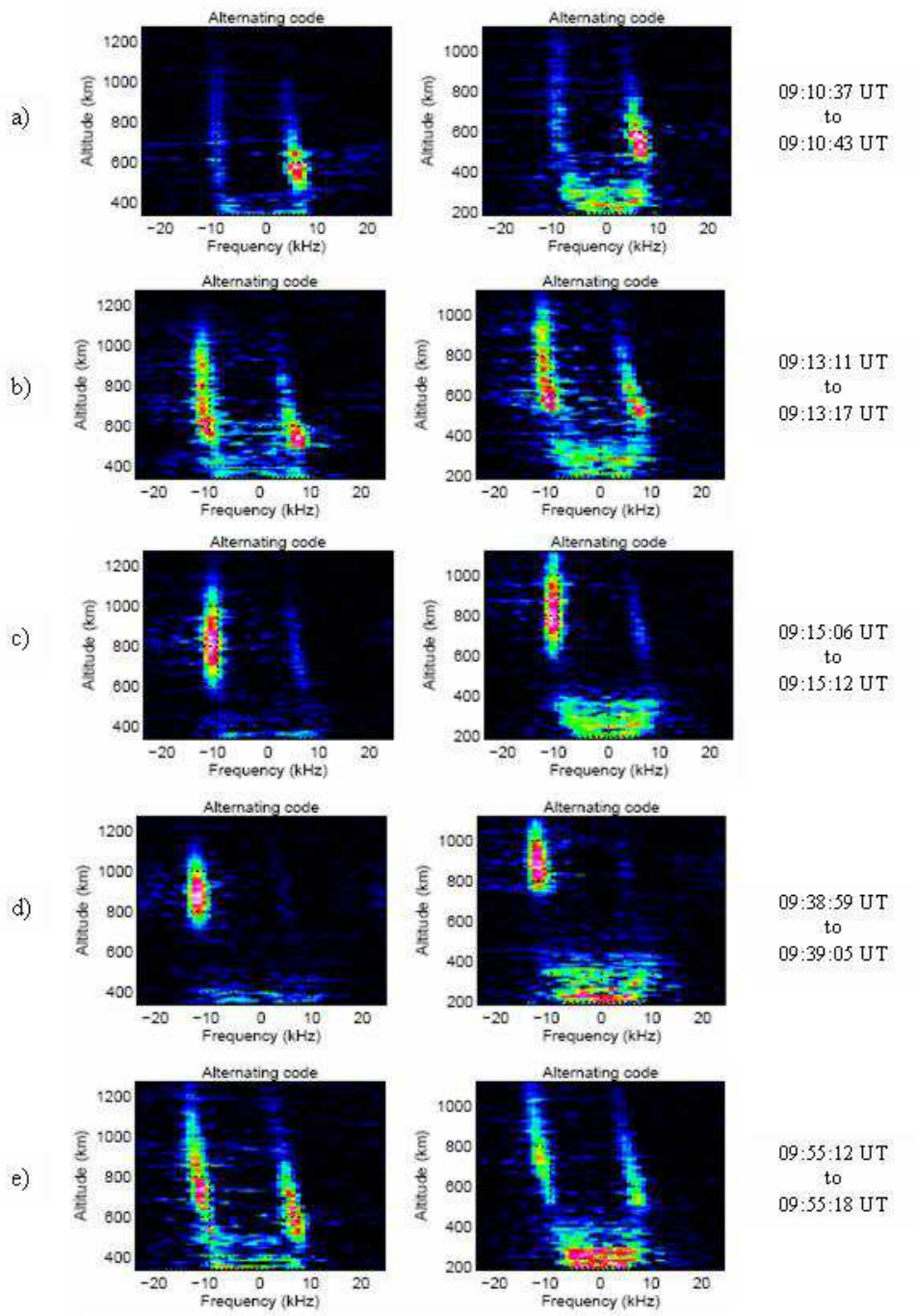

Figure 3.9: Examples of spectra of NEIALs on January 22nd 2004, showing either one (c,d) or both (a,b,e) shoulders enhanced. Figure from *Lunde et al.* [2007].

In literature, NRLMSISE-00 has been reported to underestimate the neutral density by ∼20-30% compared to CHAMP satellite measurements at solar maximum during both disturbed and quiet conditions [e.g., *Forbes et al.*, 2005; *Liu and Lühr*, 2005]. During the International Polar Year (IPY) [e.g., *Alfonsi et al.*, 2008] from March 2007 to February 2008, which is a big percentage of the data used in our study at solar minimum, *Vickers et al.* [2013] estimated the neutral density of the upper atmosphere above ∼250 km using the ESR measurements. They reported that the NRLMSISE-00 density was 1-1.5 times higher than the ESR estimates. We can therefore conclude that NRLMSISE-00 density is most likely a lower limit especially during solar maximum, but could be an overestimate at solar minimum. This implies that the thermal component we derive, generally and particularly at solar maximum, is just a lower limit. On the other hand, the thermal component could be overestimated at solar minimum, which would imply even lower occurrence rate at solar minimum.

In Papers I-III, the atomic oxygen density coincident with the ESR measurements were generated from the NRLMSISE-00 model. In Paper III, we compare the NRLMSISE-00 atomic oxygen density with that from a physics-based numerical model called TIE-GCM.

3.2.2 TIE-GCM model

The thermosphere-ionosphere-electrodynamics general circulation model (TIE-GCM) [*Dickinson et al.*, 1981; *Qian et al.*, 2009, 2014; *Richmond*, 1995; *Roble et al.*, 1977, 1982], is a global 3-D numerical model, developed at the National Center for Atmospheric Research (NCAR) High-Altitude Observatory (HAO) , that simulates the coupled thermosphere/ionosphere system from ∼97 to ∼600 km [*Qian et al.*, 2014]. It is a physics based and first principles model which self consistently solves the fully coupled, nonlinear, hydrodynamic, thermodynamic, and continuity equations of neutral gas, the ion and electron energy and momentum equations, the ion continuity equation, and neutral wind dynamo [*Qian et al.*, 2014]. The high-latitude potential imposed by the magnetospheric processes is specified by either the *Heelis et al.* [1982] or the *Weimer* [2005] empirical model, where the Heelis model is based on the *Kp* index as input and the Weimer model is based on solar wind and IMF data. In Paper III, we use the Heelis run TIE-GCM atomic oxygen density, and in Chapter 4 we use the Weimer run TIE-GCM atomic oxygen density to derive the thermal component.

Chapter 4

Results and discussion

This thesis investigates the importance and significance of thermally excited 630.0 nm emissions in the cusp and polar ionosphere. The main part of this work has been presented in three scientific papers, Papers I-III, which are included in the appendix. In this chapter, we first give a summary of each of the three papers separately and afterwards, discuss the papers as a whole.

4.1 Summary of papers

4.1.1 Paper 1: On the contribution of thermal excitation to the total 630.0 nm emissions in the northern cusp ionosphere

The first part of this investigation is to quantify the contribution and potential importance of thermal excitation in the cusp and polar ionosphere. *Wickwar and Kofman* [1984] calculated the thermal component in the cusp, when high electron temperatures prevailed, but did not have optical observations. At the same latitudes, *Carlson et al.* [2013] compared emission rates derived from two ESR scanning experiments, with coincident all-sky images, using boundary tracking. They emphasised the need for analysis with smaller error bars adequate to go beyond boundary tracking and enable more quantitative aeronomy applications. In Paper I, we use the ESR measurements from the fixed field-aligned beam, which have the smallest statistical error bars compared to earlier work [e.g., *Carlson et al.*, 2013; *Wickwar and Kofman*, 1984]. Two days were selected for investigation, on the basis of existence of high electron temperatures ($>$3000 K) as suggested in literature for thermal excitation to become important [e.g., *Kozyra et al.*, 1990; *Lockwood et al.*, 1993], and availability of coincident optical data from the MSP at KHO.

For both cases, the electron temperature exceeding 3000 K was found near magnetic

noon, in the cusp ionosphere over Svalbard. The electron temperature enhancements corresponded to electron density enhancements exceeding 10^{11} m^{-3} accompanied by intense 630.0 nm emissions in a field of view common to both the ESR, and the MSP. This offered an excellent opportunity to investigate the role of thermally excited O(^{1}D) 630.0 nm emissions in the cusp ionosphere. The thermal component was derived from the ESR measurements and compared with optical data. This paper presents the first direct comparison of thermally excited and observed 630.0 nm intensities. For both events the calculated thermal component was found to be highly correlated with the total observed 630.0 nm (correlation coefficient > 0.8), with an average contribution of $\sim$50% both for the disturbed and the quiet cusp. The peak emission altitude was found to be above $\sim$350 km. Despite fairly constant solar wind, the calculated thermal component intensity fluctuated, possibly due to dayside transients in the aurora.

4.1.2 Paper 2: How often do thermally excited 630.0 nm emissions occur in the polar ionosphere?

Up to, and including Paper I, all studies on thermal excitation at the cusp and polar latitudes have been case studies in the cusp, concentrating on very brief periods of a few minutes to a few hours. Paper I unleashed the potential and ability of using the ESR 42 m measurements to monitor and track the occurrence of thermally excited emissions. Paper II utilises this unique potential, and extends the technique from Paper I, to investigate thermal excitation at all MLTs, without any restriction on electron temperature and density. The only condition is that only ESR 42 m measurements from experiments that ran for $\sim$24 hours, are used. The whole ESR database for years 2000-2015, is searched for days that satisfy this condition. This paper provides the first statistical study of thermally excited emissions, based on ionospheric parameter measurements. Through this we are able to statically study the occurrence of thermally excited emissions. This paper provides an overview on magnetic local time distribution of these events, intensity levels, ionosphere, solar wind and IMF conditions, associated with the strong thermal component.

The peak occurrence of strong thermal component (Intensity$>$1 kR), is found around magnetic noon, where the radar observations show cusp-like characteristics. The associated ionospheric, interplanetary magnetic field and solar wind conditions, favor dayside magnetic reconnection as the dominant driving process. The thermal emissions are found to occur 10 times more frequently on the dayside than on the nightside, with an average intensity of 1-5 kR. For typical electron densities in the polar

ionosphere (2×10^{11} m^{-3}), we find the peak occurrence rate at extreme electron temperatures ($>$ 3000 K), which is consistent with assumptions in literature [e.g.., *Carlson et al.*, 2013; *Kozyra et al.*, 1990; *Lockwood et al.*, 1993]. However, for extreme electron densities ($>5\times10^{11}$ m^{-3}), a completely new population of thermal emissions, that may occur at much lower electron temperatures ($\sim$2300 K), was found. The empirical atmospheric model (NRLMSISE-00) suggests that the latter population is associated with enhanced neutral atomic oxygen densities.

4.1.3 Paper 3: Seasonal and solar cycle variations of thermally excited 630.0 nm emissions in the polar ionosphere.

Until this point, little is known about how and if the occurrence of thermally excited emissions varies with season and solar cycle. General statistics were gathered in Paper II, and a dataset was put together, which provides a platform for studying the seasonal and solar cycle variations. Statistical studies that have been done on other aspects, like geomagnetic activity, have reported to have seasonal and solar cycle variations [e.g., *Cliver et al.*, 2000; *Zhao and Zong*, 2012]. Some studies have also reported an equinoctial asymmetry in the high-latitude ionosphere [e.g., *Aruliah et al.*, 1996].

Paper III, therefore, sets out to investigate such variations in the occurrence of the strong thermal component. The dataset gathered in Paper II (only strong thermal) is categorised into seasons of the year and solar maximum and solar minimum, and analysed for the seasonal and solar cycle dependences.

Solar cycle and seasonal variations are found in the occurrence of strong thermally excited 630.0 nm emissions in the polar ionosphere. Thermally excited emissions are found to maximize at solar maximum with peak occurrence rate of $\sim$40% compared to $\sim$2% at solar minimum. These emissions are also found to have the highest occurrence in equinox and the lowest occurrence rate in summer and winter. There is an equinoctial asymmetry in the occurrence rate, which reverses with the solar cycle. This equinoctial asymmetry is attributed to variations of the solar wind-magnetosphere coupling, arising from the R-M effect. The occurrence rate of thermal excitation emission on the dayside, at Svalbard, has been found to be higher in autumn than spring at solar maximum and the reverse at solar minimum. Enhanced electron temperatures have been found to characterize the strong thermal component for solar minimum and winter, whereas enhanced electron densities characterize the thermal component for solar maximum. The results point to solar wind-magnetosphere-ionosphere coupling as the dominant controlling process.

4.2 Additional results

This section presents additional results that are not included in the papers.

Typical ionospheric conditions

The key parameters used to derive the thermal emission intensities in this thesis are electron temperature, electron density, and atomic oxygen density. The highest occurrence rate of the strong thermal component was seen at equinox in Paper III. The distribution of the three parameters during equinox is used to extract information on the typical parameter values for the strong thermal component. Figure 4.1 presents the occurrence rate of the three parameters at three altitude ranges, 250-300 km, 300-350 km, and 350-400 km, for autumn and spring. The peak occurrence at 3000 K confirms, and is in agreement with, literature [e.g., *Carlson et al.*, 2013; *Johnsen et al.*, 2012; *Kozyra et al.*, 1990, 1997; *Mantas*, 1994; *Wickwar and Kofman*, 1984] . The typical electron temperature ranges from 2500-4000 K. On the other hand the typical electron densities are (1-8)$\times 10^{11}$ m^{-3}, with the peak at 5×10^{11} m^{-3}.

We however note that there is no characteristic distribution for atomic oxygen (bottom panel). This indicates that the variations we see in Papers II and III, are because of the variation in the electron temperature and density. There was an equinoctial asymmetry observed in the occurrence rate of the strong thermal component in Paper III. However, no asymmetry is seen in the occurrence rates of individual parameters during autumn and spring.

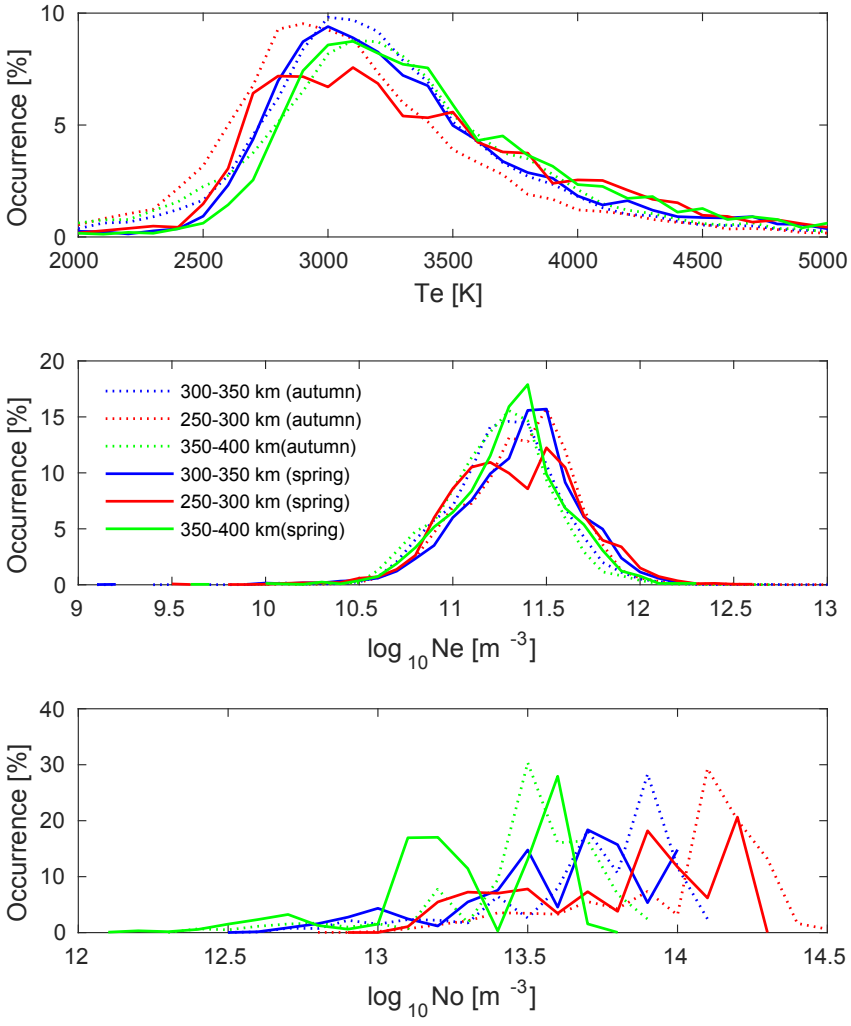

Figure 4.1: Distribution of electron temperature, electron density, and modelled atomic oxygen density at 3 different altitude ranges 250-300 km (red), 300-350 km (blue), and 350-400 km (green), for the strong thermal component at equinox, where we find the highest occurrence of the strong thermal component. The spring (bold lines) and autumn (dashed lines) are separated, and no equinoctial asymmetry is seen in the individual parameters.

Thermal component with TIEGCM atomic oxygen density

The atomic oxygen density that we have used, is only a statistical average as modelled by the NRLMSISE-00 model. In Paper III, we compare this atomic oxygen density to the TIEGCM model at winter and summer for solar minimum and solar maximum. We found that the NRLMSISE-00 gives lower densities than the TIEGCM for all compared densities, with a bigger difference in winter than summer, and for solar maximum than solar minimum. The thermal component derived using atomic oxygen density from the Weimer driven TIEGCM, for the two case studies in Paper I is shown in Figure 4.2 in comparison to the optical observations (black dashed line) and the thermal component based NRLMSISE-00 (red dashed line). The thermal component, derived based on TIEGCM atomic oxygen density, sometimes exceeds the optical measurements. We however, note that both cases are from winter, which showed the biggest discrepancy. On this basis, the thermal component based on NRLMSISE-00 atomic oxygen appears to be a better representation than the TIEGCM.

4.3 Discussion

How significant are thermally excited auroral emissions in the polar ionosphere?

The uncertainty surrounding the significance of thermal excitation in the cusp and polar ionosphere has existed for many years, as pointed out in Chapter 2. The main reason is that, it is not clear if the necessary electron gas temperature, electron density, and atomic oxygen density levels, for the production of 630.0 nm emission intensities of kR levels are achievable in the cusp and polar ionosphere [e.g., *Lockwood et al.*, 1993]. To a large extent, this thesis has focused on thermally excited 630.0 nm emissions intensities $>$1 kR, which we have used as the threshold for significant thermal excitation as discussed in Paper II. Papers I and II show the thermal excitation to give 630.0 nm emission intensities of 1-15 kR, and it could exceed 15 kR sometimes. The thermal excitation intensity of $\sim$7 kR reported by *Wickwar and Kofman* [1984] falls within our intensity range derived from statistics. These are significant intensity levels that are easily detectable by optical instruments [e.g., Paper I, *Wickwar and Kofman*, 1984].

Paper I has for the first time separated the thermal excitation component from the observed total 630.0 nm emission intensity. This has enabled us to estimate and quantify the contribution of the thermal excitation component. The estimations show that, when favourable conditions prevail, thermal excitation can contribute on average 50%

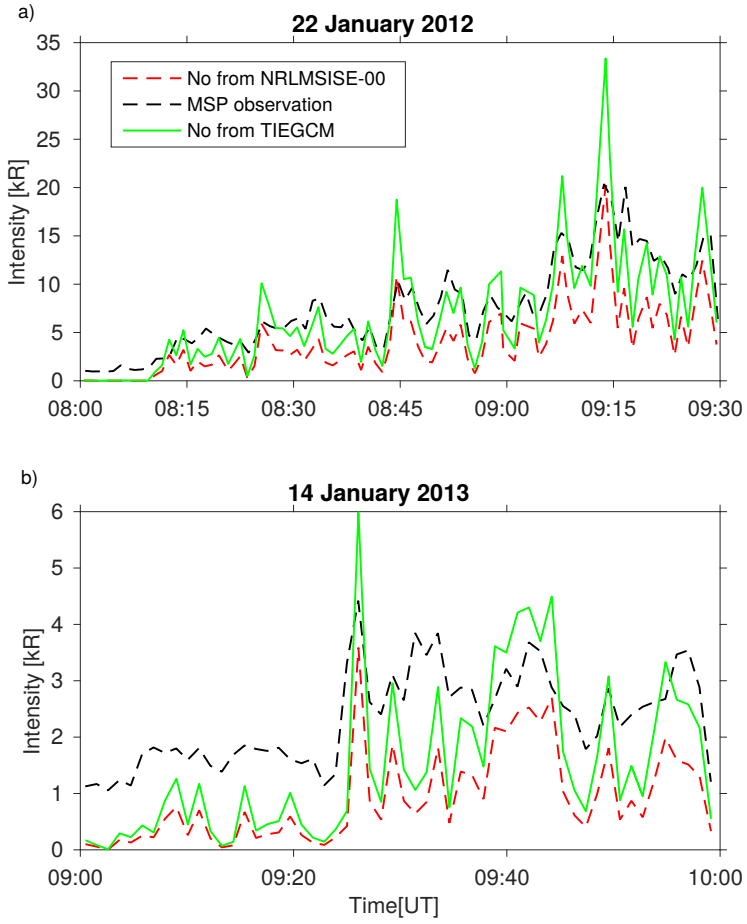

Figure 4.2: Comparison of the calculated thermally excited intensity with atomic oxygen density from the NRLMSISE-00 model (red dashed line) with the intensity calculated using atomic oxygen density from the TIEGCM model (green bold line) for January 22nd 2012 (a) and January 14th 2013 (b). The dashed black line is the optical measurements from the meridian scanning photometer at Kjell Henriksen Observatory

of the total observed 630.0 nm. Sometimes the contribution of thermal excitation has been found to even exceed 80% of the total 630.0 nm emission. When such contributions are found, the calculated thermal component highly correlates with the optical observations (with correlation coefficient >0.8). Such contributions indicate that thermal excitation can sometimes be a major and main source of the 630.0 nm emissions. As expected, the thermal component does not account for 100% of the observed 630.0 nm intensity, which implies that other processes like direct impact excitation occurs

at the same time. This is consistent with the fact that the precipitating soft electrons produce both thermal and impact emissions on the same magnetic flux tube, but the altitude of peak emission would differ [*Lockwood et al.*, 1993]. Our findings agree with *Egeland et al.* [1992] that the thermal excitation may be responsible for the 630.0 nm emissions at 350 km altitude and above.

When and where does thermal excitation become important in the polar ionosphere?

Generally, our study has shown thermal excitation to mainly occur on the dayside and peak around magnetic noon with a 10% occurrence rate. Both cases studied in Paper I were at this magnetic local time, and also both statistical studies in Papers II and III show peak occurrence at these magnetic local times. This could explain why most of the thermal excitation cases in literature are reported at these magnetic local times [e.g., *Carlson et al.*, 2013; *Wickwar and Kofman*, 1984]. The probability of occurrence is highest in the dayside cusp region.

In our study, the thermally excited emissions have been shown to have a peak emission altitude of $\sim$ 350 km, which is higher than the generally accepted emission altitude of 225-250 km for the 630.0 nm emission [e.g., *Lockwood et al.*, 1993]. This is in agreement with some of the thermal component peak emission altitudes reported in literatures [e.g., *Johnsen et al.*, 2012; *Wickwar and Kofman*, 1984], but $\sim$ 50 km lower than the peak emission altitude reported by *Carlson et al.* [2013].

Ionospheric conditions are also a key factor in identifying when and where to expect the thermal component to be important. Papers I-III have highlighted these conditions, which are to a large extent, in agreement with earlier studies [e.g., *Carlson et al.*, 2013; *Johnsen et al.*, 2012; *Wickwar and Kofman*, 1984]. The characteristic conditions have been summarised and discussed in the previous section. Our results generally show that the thermal component becomes important when the electron gas temperature exceeds $\sim$2500 K at electron densities of $\sim$(1-8)$\times 10^{11}$ m^{-3}. In Paper II, we found that the strong thermal component could even be important at a lower temperature ($\sim$2300 K) if the electron density exceeds 5×10^{11} m^3.

The results in this thesis show that the strong thermal component can occur for both southward and northward IMF conditions (Papers I and II). However, the statistical study in Paper II shows that there is a higher occurrence rate for southward IMF than for northward IMF. Furthermore, dayside magnetopause reconnection has been reported to be characterized by non zero IMF B_z [e.g., *Trattner et al.*, 2007], high solar wind dynamic pressure [e.g., *Fuselier et al.*, 2000], and enhanced electron temperature [e.g., *Lockwood et al.*, 1993]. To a large extent, the strong thermal component has been shown to occur during such conditions (e.g., Papers I and II), indicating dayside magnetic reconnection as a major driving mechanism. If the dayside magnetic reconnection is responsible for the strong thermal component, then the difference in occurrence rate for southward and northward IMF conditions that we find in Paper II, is in agreement with *Newell et al.* [2004] who report higher probability of dayside merging to occur for southward IMF than for northward IMF (35% versus 25%). In Paper I, the calculated thermal component fluctuated, despite the fairly constant solar wind, possibly due to the transient dayside magnetopause reconnection. If such cases are frequent in the statistical study in Paper II and III, then our study agrees with earlier studies [e.g., *Carlson*, 1998; *Carlson et al.*, 2013; *Lockwood et al.*, 1993] suggesting that the role of transient magnetopause reconnection in driving ionospheric convection could be greater than anticipated.

Furthermore, our study has found the strong thermal component to be most frequent at solar maximum and/or equinox. The occurrence rate is, however, not the same for spring and autumn. The equinoctial asymmetry is attributed to periodic variations in solar wind-magnetosphere coupling arising from the diurnal and seasonal variations of the Earth's dipole axis [*Aruliah et al.*, 1996, 1997; *Russell and McPherron*, 1973; *Zhao and Zong*, 2012]. This further points to the solar wind-magnetosphere coupling as a major driving process for the strong thermal excitation.

Finally, in this thesis, we take the results based on the fixed ESR 42 m beam to be a proxy or representative of the occurrence of thermally excited emissions in the cusp and polar region ionosphere. However, in the discussion in Paper III, we point out the fact that sometimes the red-line emission could be poleward of the ESR beam, and may not come into the ESR field aligned beam (see Chapter 3). *Johnsen and Lorentzen* [2012] found the red-line auroral to be located north of Longyearbyen, half of the time, for the cusp region. We have found the occurrence of thermally excited emissions to peak

around magnetic noon, the same local times as those studied by *Johnsen and Lorentzen* [2012]. Extending their results to our results, would imply that our result is mainly representative half of the time, and that the thermal emissions could be occurring north of the ESR beam, during the other half of the time. This introduces a potential bias in our dataset. It however, emphasizes that the results in this thesis are just a lower limit.

Chapter 5

Conclusion and future prospects

5.1 Conclusion

This thesis has investigated the importance of thermal excitation in the cusp and polar ionosphere. Ground-based incoherent scatter radar and optical measurements from Svalbard have been utilised in this study. The ESR measurements have been used to derive the thermal excitation component. The thermal excitation component has then been studied. Through both case and statistical studies, the thermal excitation component has been studied with the aim of answering the two open question which were stated in Chapter 1. The thesis key findings about the two questions, have been discussed in Section 4.3. Below, we summarize the main conclusions of this work.

→ Thermal excitation can be important in the cusp and polar ionosphere, particularly on the dayside. We therefore strongly recommend that any studies involving dayside 630.0 nm emissions and electron thermal balance in this region should take into account thermal excitation .

→ The strong thermal excitation component maximizes around magnetic noon, with an occurrence rate of $\sim$10%.

→ When the strong thermal component is present, it can contribute $>$50% of the total 630.0 nm emission intensity.

→ The thermally excited emissions have a relatively high peak emission altitude of $\sim$350 km, and could be responsible for the 630.0 nm emission at such altitudes and above.

→ Thermal excitation is most likely to give rise to 630.0 nm emission intensities of order of kRs when the electron gas temperature exceeds $\sim$2500 K for electron densities $\sim$(1-8)$\times 10^{11}$ m^{-3}.

→ Thermal excitation in the cusp and polar ionosphere maximizes during equinox and/or solar maximum.

→ Magnetic reconnection on the dayside is most likely the main driving process of the strong thermal excitation in the cusp and polar ionosphere.

5.2 Future prospects

The findings of this thesis have ignited more open questions, some of which are summarized below.

- What is the role of secondary electrons in the creation of thermally excited emissions? Both electron and proton precipitation creates secondary electrons when they ionize the ambient gas. These electrons may contribute to additional heating of the ambient electron gas.
- When precipitation is turned off, how long will the heated electrons prevail inside a flux-tube that convects into the polar cap? It is possible that some of the optical emissions from PMAFs could be remnants of very hot flux tubes that still have thermal emissions on them.
- What is the role of thermal emissions in polar cap arcs during northward IMF [e.g., *Carlson*, 1994; *van der Meeren et al.*, 2016]? Polar cap auroras are mostly located north of Svalbard when the IMF is northward and may not be detected by the EISCAT Svalbard Radar 42m beam. However, it should be possible to perform a similar study using data from the central polar cap (e.g. Resolute Bay ISR and all-sky cameras) in order to shed more light on this.
- What is the effect of polar cap patches on thermal emission? The generation of polar cap patches in the dayside high-density solar EUV plasma reservoir, is often a source for elevated plasma densities when these patches transit the intense electron heating region of the cusp/precipitation. It could lead to a dramatic change in the thermal balance on the affected flux tubes.
- What is the contribution of other 630.0 nm emission processes like direct impact excitation and dissociative recombination when significant thermal excitation prevails? This thesis has found that the thermal excitation component can contribute to $>$50% of the total 630.0 nm emission.

With the upcoming EISCAT_3D [e.g., *McCrea et al.*, 2015] we will get unique opportunities to study the 630.0 nm emissions processes in much greater detail. With

EISCAT_3D it should in principle also be possible to derive tomographic images in full 3-D of thermal emissions across a wide area of the auroral ionosphere.

Bibliography

Akasofu, S.-I., The latitudinal shift of the auroral belt, *Journal of Atmospheric and Terrestrial Physics*, *26*(12), 1167 – 1174, doi:https://doi.org/10.1016/0021-9169(64)90125-4, 1964. 19

Alfonsi, L., et al., Probing the high latitude ionosphere from ground-based observations: The state of current knowledge and capabilities during ipy (2007–2009), *Journal of Atmospheric and Solar-Terrestrial Physics*, *70*(18), 2293 – 2308, doi:https://doi.org/10.1016/j.jastp.2008.06.013, transport processes in the coupled solar wind-geospace system seen from a high-latitude vantage point, 2008. 42

Aruliah, A. L., A. D. Farmer, T. J. Fuller-Rowell, M. N. Wild, M. Hapgood, and D. Rees, An equinoctial asymmetry in the high-latitude thermosphere and ionosphere, *Journal of Geophysical Research: Space Physics*, *101*(A7), 15,713–15,722, doi:10.1029/95JA01102, 1996. 12, 13, 45, 51

Aruliah, A. L., J. Schoendorf, A. D. Aylward, and M. N. Wild, Modeling the high-latitude equinoctial asymmetry, *Journal of Geophysical Research: Space Physics*, *102*(A12), 27,207–27,216, doi:10.1029/97JA01991, 1997. 51

Bates, D. R., R. A. Buckingham, H. S. W. Massey, and J. J. Unwin, Dissociation, recombination and attachment processes in the upper atmosphere. ii. the rate of recombination, *Proceedings of the Royal Society of London A: Mathematical, Physical and Engineering Sciences*, *170*(942), 322–340, doi:10.1098/rspa.1939.0035, 1939. 15

Baumjohann, W., and R. Treumann, *Basic Space Plasma Physics*, Imperial College Press, London, 1996. 8, 14

Blanchard, G. T., L. R. Lyons, J. C. Samson, and F. J. Rich, Locating the polar cap boundary from observations of 6300 Å auroral emission, *Journal of Geophysical Research: Space Physics*, *100*(A5), 7855–7862, doi:10.1029/94JA02631, 1995. 20

Blelly, P.-L., C. Lathuillère, B. Emery, J. Lilensten, J. Fontanari, and D. Alcaydé, An extended transcar model including ionospheric convection: simulation of eiscat

observations using inputs from amie, *Annales Geophysicae*, *23*(2), 419–431, doi: 10.5194/angeo-23-419-2005, 2005. 4

Brekke, A., *Physics of the Upper Atmosphere*, 2 ed., Springer, Verlag Berlin Heidelberg, doi:10.1007/978-3-642-27401-5, 2013. 16

Carlson, H. C., The dark polar ionosphere: Progress and future challenges, *Radio Science*, *29*(1), 157–165, doi:10.1029/93RS02125, 1994. 54

Carlson, H. C., *Response of the Polar Cap Ionosphere to Changes in (Solar Wind) IMF*, pp. 255–270, Springer Netherlands, Dordrecht, doi:10.1007/978-94-011-5214-3-19, 1998. 51

Carlson, H. C., T. Spain, A. Aruliah, A. Skjaeveland, and J. Moen, First-principles physics of cusp/polar cap thermospheric disturbances, *Geophysical Research Letters*, *39*(19), doi:10.1029/2012GL053034, L19103, 2012. 14

Carlson, H. C., K. Oksavik, and J. I. Moen, Thermally excited 630.0nm O(1D) emission in the cusp: A frequent high-altitude transient signature, *Journal of Geophysical Research: Space Physics*, *118*(9), 5842–5852, doi:10.1002/jgra.50516, 2013. 4, 19, 21, 22, 23, 25, 27, 28, 30, 37, 38, 39, 43, 45, 46, 50, 51

Chapman, S., The absorption and dissociative or ionizing effect of monochromatic radiation in an atmosphere on a rotating earth, *Proceedings of the Physical Society*, *43*(1), 26–45, 1931. 8

Cliver, E. W., Y. Kamide, and A. G. Ling, Mountains versus valleys: Semiannual variation of geomagnetic activity, *Journal of Geophysical Research: Space Physics*, *105*(A2), 2413–2424, doi:10.1029/1999JA900439, 2000. 45

Collis, P. N., L. Häggström, K. Kaila, and M. T. Rietveld, EISCAT radar observations of enhanced incoherent scatter spectra; their relation to red aurora and field-aligned currents, *Geophysical Research Letters*, *18*(6), 1031–1034, doi:10.1029/91GL00848, 1991. 39

Cowley, S. W. H., and M. Lockwood, Excitation and decay of solar wind-driven flows in the magnetosphere-ionosphere system, *Annales Geophysicae*, *10*, 103–115, 1992. 12

Dickinson, R. E., E. C. Ridley, and R. G. Roble, A three-dimensional general circulation model of the thermosphere, *Journal of Geophysical Research: Space Physics*, *86*(A3), 1499–1512, doi:10.1029/JA086iA03p01499, 1981. 42

Doering, J., and E. Gulcicek, Absolute differential and integral electron excitation cross sections for atomic oxygyen 7. the $P^3 \rightarrow D^1$ and $P^3 \rightarrow S^1$ transitions from 4.0 to 30-eV, *Journal of Geophysical Research*, *94*, 1541–1546, doi:10.1029/JA094iA02p01541, 1989. 25

Dungey, J. W., Interplanetary magnetic field and the auroral zones, *Phys. Rev. Lett.*, *6*, 47–48, doi:10.1103/PhysRevLett.6.47, 1961. 9, 10

Egeland, A., and W. J. Burke, *Størmer's Auroral Studies*, pp. 29–107, Springer Berlin Heidelberg, Berlin, Heidelberg, doi:10.1007/978-3-642-31457-5_3, 2013. 3

Egeland, A., H. C. Carlson, W. F. Denig, K. Fukui, and E. Weber, Day-side auroral signatures based on simultaneous, coordinated observations at svalbard and greenland, *IEEE Transactions on Plasma Science*, *20*(6), 726–739, doi:10.1109/27.199521, 1992. 50

Fasel, G. J., Dayside poleward moving auroral forms: A statistical study, *Journal of Geophysical Research: Space Physics*, *100*(A7), 11,891–11,905, doi:10.1029/95JA00854, 1995. 21

Feldstein, Y., and G. Starkov, The auroral oval and the boundary of closed field lines of geomagnetic field, *Planetary and Space Science*, *18*(4), 501 – 508, doi:https://doi.org/10.1016/0032-0633(70)90127-3, 1970. 19

Forbes, J. M., G. Lu, S. Bruinsma, S. Nerem, and X. Zhang, Thermosphere density variations due to the 15-24 april 2002 solar events from champ/star accelerometer measurements, *Journal of Geophysical Research: Space Physics*, *110*(A12), doi:10.1029/2004JA010856, A12S27, 2005. 42

Forme, F., Y. Ogawa, and S. C. Buchert, Naturally enhanced ion acoustic fluctuations seen at different wavelengths, *Journal of Geophysical Research: Space Physics*, *106*(A10), 21,503–21,515, doi:10.1029/2000JA900164, 2001. 39

Foster, J. C., C. del Pozo, K. Groves, and J.-P. St. Maurice, Radar observations of the onset of current driven instabilities in the topside ionosphere, *Geophysical Research Letters*, *15*(2), 160–163, doi:10.1029/GL015i002p00160, 1988. 39

Frey, H. U., S. B. Mende, S. A. Fuselier, T. J. Immel, and N. Østgaard, Proton aurora in the cusp during southward imf, *Journal of Geophysical Research: Space Physics*, *108*(A7), doi:10.1029/2003JA009861, 2003. 10

Fuselier, S. A., K. J. Trattner, and S. M. Petrinec, Cusp observations of high- and low-latitude reconnection for northward interplanetary magnetic field, *Journal of Geophysical Research: Space Physics*, *105*(A1), 253–266, doi:10.1029/1999JA900422, 2000. 51

Fuselier, S. A., H. U. Frey, K. J. Trattner, S. B. Mende, and J. L. Burch, Cusp aurora dependence on interplanetary magnetic field bz, *Journal of Geophysical Research: Space Physics*, *107*(A7), doi:10.1029/2001JA900165, 2002. 10

Gault, W., R. Koehler, R. Link, and G. Shepherd, Observations of the optical spectrum of the dayside magnetospheric cleft aurora, *Planetary and Space Science*, *29*(3), 321 – 333, doi:https://doi.org/10.1016/0032-0633(81)90020-9, 1981. 4, 23

Gordon, W., Incoherent scattering of radio waves by free electrons with applications to space exploration by radar, *Proceedings of the IRE*, *46*(11), 1824–1829, doi:10.1109/JRPROC.1958.286852, 1958. 35

Gray, R. W., and D. T. Farley, Theory of incoherent-scatter measurements using compressed pulses, *Radio Science*, *8*(2), 123–131, doi:10.1029/RS008i002p00123, 1973. 34

Grydeland, T., A. Strømme, T. van Eyken, and C. La Hoz, The Capabilities of the EISCAT Svalbard Radar for Inter-hemispheric Coordinated Studies, *ArXiv Physics e-prints*, 2004. 35

Grydeland, T., A. Strømme, T. van Eyken, and C. L. Hoz, The Capabilities of the EISCAT Svalbard Radar for Inter-hemispheric Coordinated Studies, 2008. 35, 36

Hardy, D. A., M. S. Gussenhoven, and E. Holeman, A statistical model of auroral electron precipitation, *Journal of Geophysical Research: Space Physics*, *90*(A5), 4229–4248, doi:10.1029/JA090iA05p04229, 1985. 19

Heelis, R. A., J. K. Lowell, and R. W. Spiro, A model of the highlatitude ionospheric convection pattern, *Journal of Geophysical Research: Space Physics*, *87*(A8), 6339–6345, doi:10.1029/JA087iA08p06339, 1982. 42

Henry, R., P. Burke, and A.-L. Sinfailam, Scattering of Electrons by C, N, O, N^+, O^+, and O^{++}, *Phys. Rev.*, *178*, 218–225, doi:10.1103/PhysRev.178.218, 1969. 25

Hunten, D., F. Roach, and J. Chamberlain, A photometric unit for the airglow and aurora, *Journal of Atmospheric and Terrestrial Physics*, *8*(6), 345 – 346, doi:http://dx.doi.org/10.1016/0021-9169(56)90111-8, 1956. 22

Johnsen, M. G., and D. A. Lorentzen, A statistical analysis of the optical dayside open/closed field line boundary, *Journal of Geophysical Research: Space Physics*, *117*(A2), doi:10.1029/2011JA016984, A02218, 2012. 19, 20, 51, 52

Johnsen, M. G., D. A. Lorentzen, J. M. Holmes, and U. P. Løvhaug, A model based method for obtaining the open/closed field line boundary from the cusp auroral 6300 Å [OI] red line, *Journal of Geophysical Research: Space Physics*, *117*(A3), doi: 10.1029/2011JA016980, A03319, 2012. 4, 19, 20, 23, 26, 46, 50

Johnson, C. Y., Ion and neutral composition of the ionosphere., *Annals of the IQSY*, *5*, 197–213, 1969. 8

Kivelson, M. G., and C. T. Russell, *Introduction to Space Physics*, Cambridge University Press, New York, 1995. 8, 15

Kozyra, J. U., C. E. Valladares, H. C. Carlson, M. J. Buonsanto, and D. W. Slater, A theoretical study of the seasonal and solar cycle variations of stable aurora red arcs, *Journal of Geophysical Research: Space Physics*, *95*(A8), 12,219–12,234, doi: 10.1029/JA095iA08p12219, 1990. 22, 25, 43, 45, 46

Kozyra, J. U., A. F. Nagy, and D. W. Slater, High-altitude energy source(s) for stable auroral red arcs, *Reviews of Geophysics*, *35*(2), 155–190, doi:10.1029/96RG03194, 1997. 22, 27, 46

Kwagala, N. K., K. Oksavik, D. A. Lorentzen, and M. G. Johnsen, On the contribution of thermal excitation to the total 630.0 nm emissions in the northern cusp ionosphere, *Journal of Geophysical Research: Space Physics*, doi:10.1002/2016JA023366, 2016JA023366, 2017. 34

Kwagala, N. K., K. Oksavik, D. A. Lorentzen, and M. G. Johnsen, How Often Do Thermally Excited 630.0 nm Emissions Occur in the Polar Ionosphere?, *Journal of Geophysical Research: Space Physics*, *123*(1), 698–710, doi:10.1002/2017JA024744, 2017JA024744, 2018. 37

Lan, V. K., N. Feautrier, M. L. Dourneuf, and H. V. Regemorter, Cross sections calculations for electron oxygen scattering using the polarized orbital close coupling theory, *Journal of Physics B: Atomic and Molecular Physics*, *5*(8), 1506, 1972. 25, 27

Le, G., J. A. Slavin, and R. J. Strangeway, Space Technology 5 observations of the imbalance of regions 1 and 2 field-aligned currents and its implication to the cross-polar cap Pedersen currents, *Journal of Geophysical Research: Space Physics*, *115*(A7), doi:10.1029/2009JA014979, 2010. 21

Lehtinen, M. S., and A. Huuskonen, Selected papers from the sixth international Eiscat Workshop General incoherent scatter analysis and GUISDAP, *Journal of Atmospheric and Terrestrial Physics*, *58*(1), 435 – 452, doi:http://dx.doi.org/10.1016/0021-9169(95)00047-X, 1996. 35, 38

Lilensten, J., and P. Blelly, The TEC and F2 parameters as tracers of the ionosphere and thermosphere, *Journal of Atmospheric and Solar-Terrestrial Physics*, *64*(7), 775 – 793, doi:https://doi.org/10.1016/S1364-6826(02)00079-2, 2002. 4

Link, R., and L. L. Cogger, A reexamination of the o i 6300Å nightglow, *Journal of Geophysical Research: Space Physics*, *93*(A9), 9883–9892, doi:10.1029/JA093iA09p09883, 1988. 19

Link, R., J. McConnell, and G. Shepherd, A self-consistent evaluation of the rate constants for the production of the OI 6300 Å airglow, *Planetary and Space Science*, *29*(6), 589 – 594, doi:https://doi.org/10.1016/0032-0633(81)90106-9, 1981. 19

Link, R., J. C. McConnell, and G. G. Shepherd, An analysis of the spatial distribution of dayside cleft optical emissions, *Journal of Geophysical Research: Space Physics*, *88*(A12), 10,145–10,162, doi:10.1029/JA088iA12p10145, 1983. 23

Liu, H., and H. Lühr, Strong disturbance of the upper thermospheric density due to magnetic storms: CHAMP observations, *Journal of Geophysical Research: Space Physics*, *110*(A9), doi:10.1029/2004JA010908, A09S29, 2005. 42

Lockwood, M., Identifying the Open-Closed Field Line Boundary, in *Polar Cap Boundary Phenomena*, *NATO ASI Series*, vol. 509, edited by J. Moen, A. Egeland, and M. Lockwood, pp. 73–90, Springer Netherlands, doi:10.1007/978-94-011-5214-3_7, 1998. 11

Lockwood, M., H. C. Carlson, and P. E. Sandholt, Implications of the altitude of transient 630-nm dayside auroral emissions, *Journal of Geophysical Research: Space Physics*, *98*(A9), 15,571–15,587, doi:10.1029/93JA00811, 1993. 4, 19, 21, 22, 27, 43, 45, 48, 50, 51

Lorentzen, D. A., and A. Egeland, *Dayside aurora-the fingerprint of the polar ionosphere*, 13 pp., www.chiligroup.no, 2011. 32, 33

Lorentzen, D. A., C. S. Deehr, J. I. Minow, R. W. Smith, H. C. Stenbaek-Neielsen, F. Sigernes, R. L. Arnoldy, and K. Lynch, SCIFER-Dayside auroral signatures of magnetospheric energetic electrons, *Geophysical Research Letters*, *23*(14), 1885–1888, doi:10.1029/96GL00593, 1996. 20

Luhmann, J. G., *Introduction to Space Physics*, chap. 7, pp. I83–202, Cambridge University Press, New York, 1995. 8

Lühr, H., C. Xiong, N. Olsen, and G. Le, Near-Earth Magnetic Field Effects of Large-Scale Magnetospheric Currents, *Space Science Reviews*, *206*(1), 521–545, doi:10.1007/s11214-016-0267-y, 2017. 20

Lunde, J., B. Gustavsson, U. P. Løvhaug, D. A. Lorentzen, and Y. Ogawa, Particle precipitations during NEIAL events: simultaneous ground based observations at Svalbard, *Annales Geophysicae*, *25*(6), 1323–1336, doi:10.5194/angeo-25-1323-2007, 2007. 39, 41

Mantas, G. P., Large 6300-Å airglow intensity enhancements observed in ionosphere heating experiments are excited by thermal electrons, *Journal of Geophysical Research: Space Physics*, *99*(A5), 8993–9002, doi:10.1029/94JA00347, 1994. 24, 25, 46

Mantas, G. P., and H. C. Carlson, Reexamination of the O(3P→1D) excitation rate by thermal electron impact, *Geophysical Research Letters*, *18*(2), 159–162, doi:10.1029/91GL00019, 1991. 25, 27, 29

Mantas, G. P., and J. C. Walker, The penetration of soft electrons into the ionosphere, *Planetary and Space Science*, *24*(5), 409 – 423, doi:http://dx.doi.org/10.1016/0032-0633(76)90085-4, 1976. 12, 17

McCrea, I., et al., The science case for the EISCAT_3D radar, *Progress in Earth and Planetary Science*, *2*(1), 21, doi:10.1186/s40645-015-0051-8, 2015. 54

Meier, R. R., D. J. Strickland, J. H. Hecht, and A. B. Christensen, Deducing composition and incident electron spectra from ground-based auroral optical measurements: A study of auroral red line processes, *Journal of Geophysical Research: Space Physics*, *94*(A10), 13,541–13,552, doi:10.1029/JA094iA10p13541, 1989. 4, 18, 22

Michell, R., and M. Samara, Observability of NEIALs with the Sondrestrom and Poker Flat incoherent scatter radars, *Journal of Atmospheric and Solar-Terrestrial Physics*, *105–106*, 299 – 307, doi:10.1016/j.jastp.2012.12.008, 2013. 39

Michell, R. G., and M. Samara, High-resolution observations of naturally enhanced ion acoustic lines and accompanying auroral fine structures, *Journal of Geophysical Research: Space Physics*, *115*(A3), doi:10.1029/2009JA014661, A03310, 2010. 39

Michell, R. G., K. A. Lynch, C. J. Heinselman, and H. C. Stenbaek-Nielsen, High time resolution PFISR and optical observations of naturally enhanced ion acoustic lines, *Annales Geophysicae*, *27*(4), 1457–1467, doi:10.5194/angeo-27-1457-2009, 2009. 39, 40

Michell, R. G., T. Grydeland, and M. Samara, Characteristics of Poker Flat Incoherent Scatter Radar (PFISR) naturally enhanced ion-acoustic lines (NEIALs) in relation to auroral forms, *Annales Geophysicae*, *32*(10), 1333–1347, doi:10.5194/angeo-32-1333-2014, 2014. 39

Milan, S. E., M. Lester, S. W. H. Cowley, and M. Brittnacher, Convection and auroral response to a southward turning of the IMF: Polar UVI, CUTLASS, and IMAGE signatures of transient magnetic flux transfer at the magnetopause, *Journal of Geophysical Research: Space Physics*, *105*(A7), 15,741–15,755, doi:10.1029/2000JA900022, 2000. 21

Milan, S. E., M. Lester, S. W. H. Cowley, K. Oksavik, M. Brittnacher, R. A. Greenwald, G. Sofko, and J.-P. Villain, Variations in the polar cap area during two substorm cycles, *Annales Geophysicae*, *21*(5), 1121–1140, 2003. 10, 12

Newell, P. T., J. M. Ruohoniemi, and C.-I. Meng, Maps of precipitation by source region, binned by IMF, with inertial convection streamlines, *Journal of Geophysical Research: Space Physics*, *109*(A10), doi:10.1029/2004JA010499, a10206, 2004. 20, 51

Ogawa, Y., S. C. Buchert, R. Fujii, S. Nozawa, and F. Forme, Naturally enhanced ion-acoustic lines at high altitudes, *Annales Geophysicae*, *24*(12), 3351–3364, doi:10.5194/angeo-24-3351-2006, 2006. 39

Oksavik, K., J. Moen, and H. C. Carlson, High-resolution observations of the small-scale flow pattern associated with a poleward moving auroral form in the cusp, *Geophysical Research Letters*, *31*(11), doi:10.1029/2004GL019838, L11807, 2004. 21

Oksavik, K., J. Moen, H. C. Carlson, R. A. Greenwald, S. E. Milan, M. Lester, W. F. Denig, and R. J. Barnes, Multi-instrument mapping of the small-scale flow dynamics related to a cusp auroral transient, *Annales Geophysicae*, *23*(7), 2657–2670, doi:10.5194/angeo-23-2657-2005, 2005. 21

Picone, J. M., A. E. Hedin, D. P. Drob, and A. C. Aikin, NRLMSISE-00 empirical model of the atmosphere: Statistical comparisons and scientific issues, *Journal of Geophysical Research: Space Physics*, *107*(A12), doi:10.1029/2002JA009430, 1468, 2002. 40

Potemra, T. A., L. J. Zanetti, R. E. Erlandson, P. F. Bythrow, G. Gustafsson, M. H. Acuña, and R. Lundin, Observations of large-scale birkeland currents with viking, *Geophysical Research Letters*, *14*(4), 419–422, doi:10.1029/GL014i004p00419, 1987. 21

Qian, L., S. C. Solomon, and T. J. Kane, Seasonal variation of thermospheric density and composition, *Journal of Geophysical Research: Space Physics*, *114*(A1), doi:10.1029/2008JA013643, a01312, 2009. 42

Qian, L., et al., *The NCAR TIE-GCM*, pp. 73 – 83, John Wiley & Sons, Ltd, doi:10.1002/9781118704417.ch7, 2014. 42

Rees, M., J. C. Walker, and A. Dalgarno, Auroral excitation of the forbidden lines of atomic oxygen, *Planetary and Space Science*, *15*(7), 1097 – 1110, doi:10.1016/0032-0633(67)90096-7, 1967. 18, 19

Rees, M. H., and R. G. Roble, Observations and theory of the formation of stable auroral red arcs, *Reviews of Geophysics*, *13*(1), 201–242, doi:10.1029/RG013i001p00201, 1975. 17

Richmond, A. D., Ionospheric electrodynamics using magnetic apex coordinates, *Journal of geomagnetism and geoelectricity*, *47*(2), 191–212, doi:10.5636/jgg.47.191, 1995. 42

Rietveld, M. T., P. N. Collis, and J.-P. St.-Maurice, Naturally enhanced ion acoustic waves in the auroral ionosphere observed with the EISCAT 933-MHz radar, *Journal of Geophysical Research: Space Physics*, *96*(A11), 19,291–19,305, doi:10.1029/91JA01188, 1991. 38

Roble, R. G., R. E. Dickinson, and E. C. Ridley, Seasonal and solar cycle variations of the zonal mean circulation in the thermosphere, *Journal of Geophysical Research*, *82*(35), 5493–5504, doi:10.1029/JA082i035p05493, 1977. 42

Roble, R. G., R. E. Dickinson, and E. C. Ridley, Global circulation and temperature structure of thermosphere with high-latitude plasma convection, *Journal of Geophysical Research: Space Physics*, *87*(A3), 1599–1614, doi:10.1029/JA087iA03p01599, 1982. 42

Romick, G. J., The detection and study of the visible spectrum of the aurora and airglow, *Proc. SPIE*, *0091*, 63–70, doi:10.1117/12.955072, 1976. 32

Russell, C. T., and R. L. McPherron, Semiannual variation of geomagnetic activity, *Journal of Geophysical Research*, *78*(1), 92–108, doi:10.1029/JA078i001p00092, 1973. 12, 51

Sandholt, J. W., H. Carlson, and A. Egeland, Dayside and polar cap aurora, *Astrophysics and space science library*, *270*, 2002. 4, 10, 11, 17, 22

Sandholt, P. E., C. J. Farrugia, J. Moen, Noraberg, B. Lybekk, T. Sten, and T. Hansen, A classification of dayside auroral forms and activities as a function of interplanetary magnetic field orientation, *Journal of Geophysical Research: Space Physics*, *103*(A10), 23,325–23,345, doi:10.1029/98JA02156, 1998. 21

Schunk, R. W., and A. F. Nagy, Electron temperatures in the f region of the ionosphere: Theory and observations, *Reviews of Geophysics*, *16*(3), 355–399, doi:10.1029/RG016i003p00355, 1978. 21, 22

Shepherd, G. G., Dayside cleft aurora and its ionospheric effects, *Reviews of Geophysics*, *17*(8), 2017–2033, doi:10.1029/RG017i008p02017, 1979. 4

Shyn, T. W., and W. E. Sharp, Differential excitation cross section of atomic oxygen by electron impact: (^{3}P$-^1$D transition), *Journal of Geophysical Research: Space Physics*, *91*(A2), 1691–1697, doi:10.1029/JA091iA02p01691, 1986. 25

Siscoe, G. L., and T. S. Huang, Polar cap inflation and deflation, *Journal of Geophysical Research: Space Physics*, *90*(A1), 543–547, doi:10.1029/JA090iA01p00543, 1985. 12

Smith, K., R. J. W. Henry, and P. G. Burke, Calculations on the scattering of electrons by atomic systems with configurations $2p^q$, *Phys. Rev.*, *157*, 51–68, doi:10.1103/PhysRev.157.51, 1967. 25

Solomon, S. C., P. B. Hays, and V. J. Abreu, The auroral 6300 Å emission: Observations and modeling, *Journal of Geophysical Research: Space Physics*, *93*(A9), 9867–9882, doi:10.1029/JA093iA09p09867, 1988. 4

Southwood, D. J., The ionospheric signature of flux transfer events, *Journal of Geophysical Research: Space Physics*, *92*(A4), 3207–3213, doi:10.1029/JA092iA04p03207, 1987. 21

T. Russell, C., Geophysical coordinate transformations, *2*, 184–196, 1971. 10

Thomas, L. D., and R. K. Nesbet, Low-energy electron scattering by atomic oxygen, *Phys. Rev. A*, *11*, 170–173, doi:10.1103/PhysRevA.11.170, 1975. 25

Trattner, K. J., J. S. Mulcock, S. M. Petrinec, and S. A. Fuselier, Probing the boundary between antiparallel and component reconnection during southward interplanetary magnetic field conditions, *Journal of Geophysical Research: Space Physics*, *112*(A8), n/a–n/a, doi:10.1029/2007JA012270, a08210, 2007. 51

Turunen, T., J. Markkanen, and A. P. van Eyken, Ground clutter cancellation in incoherent radars: solutions for EISCAT Svalbard radar, *Annales Geophysicae*, *18*(9), 1242–1247, doi:10.1007/s00585-000-1242-0, 2000. 36

van der Meeren, C., K. Oksavik, D. A. Lorentzen, L. J. Paxton, and L. B. N. Clausen, Scintillation and irregularities from the nightside part of a Sunaligned polar cap arc, *Journal of Geophysical Research: Space Physics*, *121*(6), 5723–5736, doi:10.1002/2016JA022708, 2016. 54

Vickers, H., M. J. Kosch, E. Sutton, Y. Ogawa, and C. La Hoz, Thermospheric atomic oxygen density estimates using the EISCAT Svalbard Radar, *Journal of Geophysical Research: Space Physics*, *118*(3), 1319–1330, doi:10.1002/jgra.50169, 2013. 42

Vontrat-Reberac, A., D. Fontaine, P.-L. Blelly, and M. Galand, Theoretical predictions of the effect of cusp and dayside precipitation on the polar ionosphere, *Journal of Geophysical Research: Space Physics*, *106*(A12), 28,857–28,865, doi:10.1029/2001JA900131, 2001. 9

Wannberg, G., et al., The EISCAT Svalbard radar: A case study in modern incoherent scatter radar system design, *Radio Science*, *32*(6), 2283–2307, doi:10.1029/97RS01803, 1997. 37

Weimer, D. R., Improved ionospheric electrodynamic models and application to calculating joule heating rates, *Journal of Geophysical Research: Space Physics*, *110*(A5), doi:10.1029/2004JA010884, 2005. 42

Wickwar, V. B., and W. Kofman, Dayside red auroras at very high latitudes: The importance of thermal excitation, *Geophysical Research Letters*, *11*(9), 923–926, doi:10.1029/GL011i009p00923, 1984. 5, 19, 22, 23, 24, 43, 46, 48, 50

Xiong, C., H. Lühr, H. Wang, and M. G. Johnsen, Determining the boundaries of the auroral oval from CHAMP field-aligned current signatures – Part 1, *Annales Geophysicae*, *32*(6), 609–622, doi:10.5194/angeo-32-609-2014, 2014. 19, 20

Zhao, H., and Q.-G. Zong, Seasonal and diurnal variation of geomagnetic activity: Russell-McPherron effect during different IMF polarity and/or extreme solar wind conditions, *Journal of Geophysical Research: Space Physics*, *117*(A11), doi:10.1029/2012JA017845, a11222, 2012. 12, 45, 51

Paper I

On the contribution of thermal excitation to the total 630.0 nm emissions in the northern cusp ionosphere

N. K. Kwagala, K. Oksavik, D. A. Lorentzen and M. G. Johnsen

Journal of Geophysical Research, Vol. 122, doi:10.1002/2016JA023366 (2017)

AGU PUBLICATIONS

JGR

Journal of Geophysical Research: Space Physics

RESEARCH ARTICLE
10.1002/2016JA023366

Key Points:
- Thermally excited emissions at 630.0 nm can be important in the cusp ionosphere
- These emissions can occur both in the active and disturbed cusp
- The peak emission altitude for these emissions is above 350 km

Correspondence to:
N. K. Kwagala,
norah.kwagala@uib.no

Citation:
Kwagala, N. K., K. Oksavik, D. A. Lorentzen, and M. G. Johnsen (2017), On the contribution of thermal excitation to the total 630.0 nm emissions in the northern cusp ionosphere, *J. Geophys. Res. Space Physics*, *122*, doi:10.1002/2016JA023366.

Received 19 AUG 2016
Accepted 23 NOV 2016
Accepted article online 7 DEC 2016

On the contribution of thermal excitation to the total 630.0 nm emissions in the northern cusp ionosphere

Norah Kaggwa Kwagala[1,2], Kjellmar Oksavik[1,2], Dag A. Lorentzen[2], and Magnar G. Johnsen[3]

[1]Birkeland Centre for Space Science, University of Bergen, Bergen, Norway, [2]University Centre in Svalbard, Longyearbyen, Norway, [3]Tromsø Geophysical Observatory, Arctic University of Norway, Tromsø, Norway

Abstract Direct impact excitation by precipitating electrons is believed to be the main source of 630.0 nm emissions in the cusp ionosphere. However, this paper investigates a different source, 630.0 emissions caused by thermally excited atomic oxygen O(^{1}D) when high electron temperature prevail in the cusp. On 22 January 2012 and 14 January 2013, the European Incoherent Scatter Scientific Association (EISCAT) radar on Svalbard measured electron temperature enhancements exceeding 3000 K near magnetic noon in the cusp ionosphere over Svalbard. The electron temperature enhancements corresponded to electron density enhancements exceeding 10^{11} m^{-3} accompanied by intense 630.0 nm emissions in a field of view common to both the EISCAT Svalbard radar and a meridian scanning photometer. This offered an excellent opportunity to investigate the role of thermally excited O(^{1}D) 630.0 nm emissions in the cusp ionosphere. The thermal component was derived from the EISCAT Radar measurements and compared with optical data. For both events the calculated thermal component had a correlation coefficient greater than 0.8 to the total observed 630.0 nm intensity which contains both thermal and particle impact components. Despite fairly constant solar wind, the calculated thermal component intensity fluctuated possibly due to dayside transients in the aurora.

1. Introduction

The prominent dayside emission in the cusp ionosphere is the 630.0 nm resulting from the O(^{1}D) state of atomic oxygen [*Rees et al.*, 1967; *Cogger et al.*, 1980]. The cusps are the regions where the solar wind has direct entry into the Earth's ionosphere. The highest probability of observing low-altitude cusp-like particle precipitation [e.g., *Newell and Meng*, 1988, 1992, 1994] and dayside cusp aurora [*Sandholt et al.*, 1998a, 2004] is between 10:30–13:30 magnetic local time (MLT) and around 75–80° magnetic latitude (MLAT), which is the MLAT range for Svalbard. For this reason, our study will focus on 12 ± 2 MLT over Svalbard, which we define as the area of the cusp ionosphere. Direct impact excitation of the O(^{1}D) by precipitating electrons is believed to be the main source of the 630.0 nm emissions in the cusp ionosphere [*Solomon et al.*, 1988; *Meier et al.*, 1989]. However, the O(^{1}D) state can also be excited by energetic electrons from the tail of the thermal electron distribution when the electron temperature is sufficiently high [*Meier et al.*, 1989; *Lockwood et al.*, 1993; *Mantas*, 1994; *Carlson et al.*, 2013]. Under such conditions, the thermal excitation component is anticipated to contribute significantly to the 630.0 nm emission although it is not well documented in literature.

The ambient electron gas in the ionosphere is believed to have a thermal or Maxwellian energy distribution where the population decreases exponentially with increasing energy. Therefore, the number of electrons above a particular energy is greatly dependent on the electron temperature. The O(^{1}D) state has a low excitation threshold of 1.96 eV. If the electron temperature exceeds 3000 K, there may be enough electrons in the high-energy tail to excite observable emissions from the O(^{1}D) state. At an electron temperature of 2000 K only 0.01% of a Maxwellian electron population has sufficient energy to excite the O(^{1}D) state. At an electron temperature of 4000 and 6000 K this fraction increases to 1.5% and 7.3%, respectively [*Mantas*, 1994].

The 630.0 nm emission in the cusp is the result of soft (hundreds of eV) electron precipitation into the ionosphere [*Eather et al.*, 1979]. When a soft electron flux is incident in the atmosphere, half of the incident energy is carried out of the atmosphere [*Schunk and Nagy*, 1978]. The remaining energy is used to ionize and excite the neutral constituents mainly atomic oxygen in the *F* region and to heat the ambient electron gas by Coulomb collisions. The electron temperature can rise well above the ion and neutral temperatures to the point when

AGU Journal of Geophysical Research: Space Physics 10.1002/2016JA023366

the collision with ions can no longer effectively cool the electron gas. When the electron density is high, the electron gas cools by collision with ions, and thermal balance is attained at much lower electron temperature [*Lockwood et al.*, 1993]. This is because the rate of cooling to the ions is proportional to electron density N_e times atomic oxygen density N_o and $N_o = N_e$ in the *F* layer. Therefore, the rate of cooling to the ions is proportional $(N_e)^2$. The electron temperature is expected to be low and in good thermal contact when the electron density is enhanced. A combination of the electron temperature exceeding 3000 K and an electron density enhancement would indicate poor thermal balance. In such cases another cooling mechanism, collisional excitation of the $O(^1D)$ state, which can lead to 630.0 nm emissions, becomes important [*Carlson et al.*, 2013].

Wickwar and Kofman [1984] carried out a similar study to ours; however, their measurements were during sunlit conditions. In our study, we overcome this by using measurements from Svalbard during winter where we can make simultaneous optical measurements to also verify their results.

It is also important to note that echoes from non-Maxwellian distributions have been reported in incoherent scatter radar experiments at high latitude. Such events are referred to as naturally enhanced ion acoustic lines (NEIALs) [*Foster et al.*, 1988; *Michell et al.*, 2009; *Michell and Samara*, 2013; *Kontar and Pécseli*, 2005; *Strømme et al.*, 2005]. NEIALs are captured as echoes which enhance one or both ion line shoulders in the typical power spectrum by 1–2 orders of magnitude [*Rietveld et al.*, 1991; *Collis et al.*, 1991], and enhancements up to 5 orders of magnitude have been reported as well [*Schlatter et al.*, 2013]. NEIALs have been observed in field-aligned measurements of incoherent scatter radars (ISRs). *Schlatter et al.* [2015] reported the NEIAL echoes to occur on field lines with particle precipitation. NEIALs have been observed in the *F* and even *E* regions during magnetically disturbed conditions [*Foster et al.*, 1988; *Rietveld et al.*, 1991; *Ogawa et al.*, 2006] with very high electron temperatures and 630.0 nm emission intensities at levels roughly above 15 kR [*Lunde et al.*, 2007; *Collis et al.*, 1991]. Standard analysis of ISR data, Grand Unified Incoherent Scatter Design and Analysis Package (GUISDAP) [*Lehtinen and Huuskonen*, 1996] assumes a Maxwellian distribution of the plasma. Consequently, the ISR parameters derived during NEIALs are unreliable.

In this paper we investigate the contribution of thermal excitation to the 630.0 nm emission in the cusp ionosphere. We derive the 630.0 nm emission rate due to thermal excitation using incoherent scatter radar measurements from Svalbard and compare it with optical observations from the same location. The instrumentation is described in section 2, and the observations are given in section 3. The discussion and conclusions are found in sections 4 and 5.

2. Instrumentation

2.1. The Meridian Scanning Photometer

The meridian scanning photometer (MSP) at the Kjell Henriksen Observatory (KHO) at Longyearbyen, Svalbard, is the main optical instrument used in this study. The KHO is located at 78.148°N, 16.043°E, and 520 m altitude. The MSP has five detector channels, where each channel consists of a narrow optical band-pass filter mounted onto a tilting frame. The tilting filter photometers are placed in front of a rotating mirror which scans the sky from north to south along the magnetic meridian and delivers intensity as a function of elevation angle in the meridian plane. The field of view is approximately one angular degree, and it takes 16 s to assemble one meridian scan with a typical spectral resolution of 0.4 nm. The five wavelengths include 630.0 nm, 427.8 nm, 557.7 nm, 486.1 nm, and 844.6 nm. For this study we mainly use the 630.0 nm channel which is the red line from the $O(^1D)$ excited state of atomic oxygen. The background is obtained by tilting each filter away from the peak emissions to an angle that transmits wavelengths representing the background emissions. The method of tilting enables the subtraction of the background from the peak emission [*Romick*, 1976]. Data from the MSP are absolutely calibrated in units of Rayleigh (R) which enables us to directly compare our calculations with observations. For studies of the dayside aurora, the MSP requires clear dark periods, which for Svalbard occurs in the winter months from late November to late January.

2.2. EISCAT Svalbard Radar

The EISCAT Svalbard Radar (ESR) is located 12 km southeast of Longyearbyen, Svalbard, at 78.15°N, 16.02°E, and 445 m altitude about 600 m north of KHO. The ESR operates in the 500 MHz band with a peak transmitted power of 1.0 MW. It has two dish antennas: a fully steerable parabolic 32 m dish and a fixed field-aligned 42 m dish. The ESR is ideal for studies of the cusp and polar cap. The MSP at KHO scans through the field of view of the 42 m dish at 81.6° elevation from the south. The geographic location of the ESR and MSP are shown in Figure 1. The black line shows the scanning field of view of the MSP, and the red circle marks the ESR 42 m

AGU Journal of Geophysical Research: Space Physics 10.1002/2016JA023366

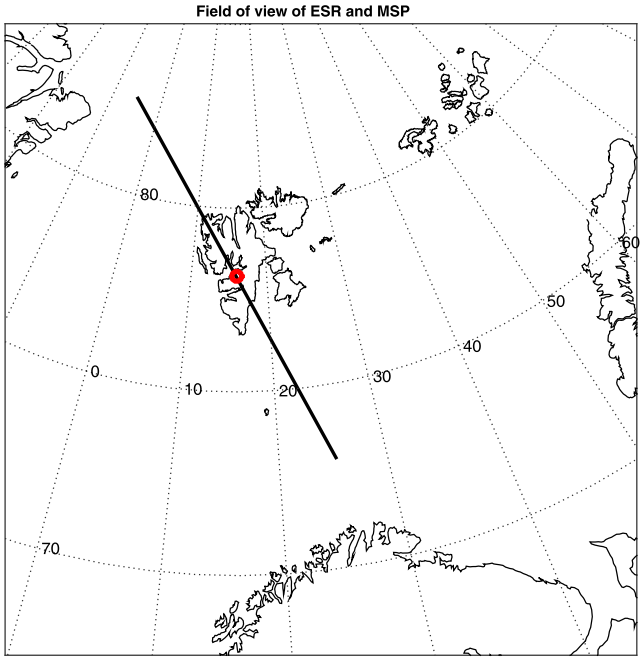

Figure 1. The black line indicates the field of view of the MSP, and the red circle indicates the ESR 42 m beam over Svalbard.

beam which is colocated with the MSP. We searched the entire ESR 42 m data archive for periods when both the electron density and electron temperatures were enhanced with the electron temperature exceeding 3000 K. Two events, 22 January 2012 and 14 January 2013, satisfied the preceding conditions with available optical data.

2.3. Solar Wind Data

Solar wind and interplanetary magnetic field (IMF) parameters were obtained from the GSFC/SPDF OMNI web interface. We used the high-resolution 5 min data which have already been time shifted to the magnetopause. The data include the 5 min averages of IMF components in GSM coordinates, solar wind speed, and proton density.

2.4. The Empirical Atmosphere Model

The density of atomic oxygen was generated from the empirical atmospheric model called the Naval Research Laboratory Mass Spectrometer and Incoherent Scatter Radar 2000 model (NRLMSISE-00) [*Picone et al.*, 2002].

2.5. Numerical Model: Calculation of Thermal Emission Rates

Mantas and Carlson [1991] reassessed the $O(^1D)$ thermal electron excitation rate putting into consideration both theoretical cross-section calculations [*Lan et al.*, 1972; *Thomas and Nesbet*, 1975] and experimental measurements of the cross section [*Doering and Gulcicek*, 1989]. They came up with a simple parametric equation for the thermal electron impact excitation rate α as a function of the electron temperature T_e. The cross-section calculations by *Lan et al.* [1972] have been reported to be the most complete so far. Using the cross sections presented by *Lan et al.* [1972], *Mantas and Carlson* [1991] recommended the equation

$$\alpha\left(T_e\right) = 0.15 \times \sqrt{T_e} \times \frac{\left(8537 + T_e\right)}{\left(34191 + T_e\right)^3} \times e^{\left(\frac{-22756}{T_e}\right)} \quad \left(\mathrm{cm}^3/\mathrm{s}\right) \tag{1}$$

Journal of Geophysical Research: Space Physics 10.1002/2016JA023366

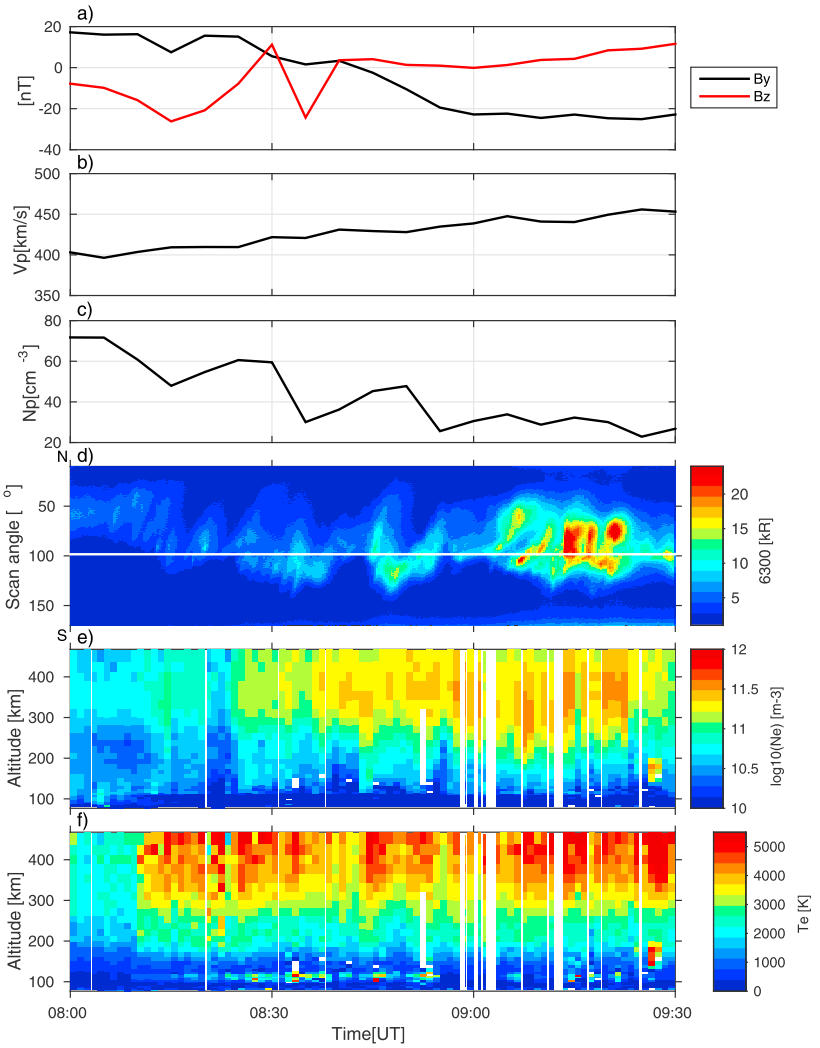

Figure 2. Solar wind and ionospheric data for Event 1 on 22 January 2012. (a) The interplanetary magnetic field components B_y and B_z. (b) The solar wind speed. (c) The solar wind density. (d) Keogram from the meridian scanning photometer for the 630.0 nm emission line and the white line indicates the location of the ESR 42 m beam. (e) Electron density profiles. (f) Electron temperature profiles.

for the thermal electron impact $O(^1D)$ excitation rate $\alpha(T_e)$, where T_e is the electron temperature in kelvin. The thermal excitation component depends on the electron density (N_e) and the number density of atomic oxygen (N_o) which are available to excite by collision, hence the excitation rate $\alpha(T_e)$. *Carlson et al.* [2013] employed equation (1) and derived the altitude (h) discriminated volume emission rate per kilometer (Rayleighs/km) of emission at 630.0 nm:

$$I_{630}(h) = \alpha\left[T_e(h)\right] \times N_o(h) \times N_e(h) \quad \text{(Rayleighs/km)} \tag{2}$$

AGU Journal of Geophysical Research: Space Physics 10.1002/2016JA023366

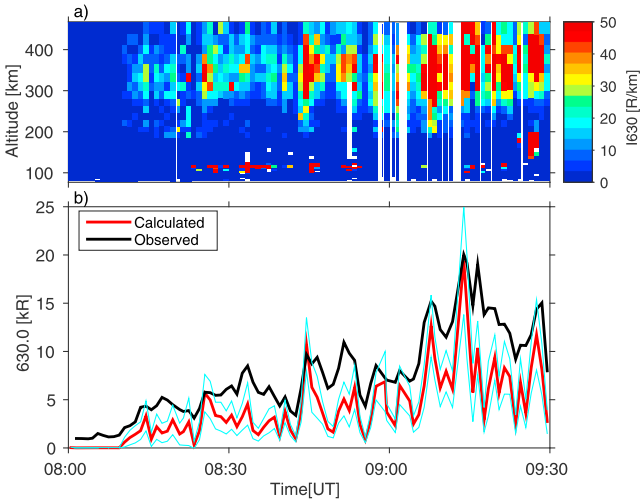

Figure 3. (a) The calculated volume emission rate versus height and (b) a comparison of the calculated thermal component with the MSP observations for event 1 on 22 January 2012. The cyan lines mark the upper and lower limits of the the error bars of the calculated thermal component.

which when integrated over the line of sight gives the total vertical column intensity for the emission at 630.0 nm:

$$I_{630} = \int_{250\text{km}}^{650\text{km}} I_{630}(h)\mathrm{d}h \quad \text{(Rayleighs)} \tag{3}$$

where $N_o(h)$ and $N_e(h)$ are measured in cm^{-3}, $T_e(h)$ in kelvin, and all variables are functions of altitude (h) in kilometers. For more details, see *Carlson et al.* [2013, and references therein].

3. Observations and Results

3.1. Event 1: 22 January 2012

Our first event is the interval 08:00–09:30 UT on 22 January 2012. Earlier on 22 January 2012 at 06:17 UT, the Earth was hit by a coronal mass ejection which led to very large interplanetary magnetic field and solar wind density compared to average values. Generally, this event is associated with disturbed conditions. In Figure 2a, the interplanetary magnetic field (IMF) B_z component was southward at 08:00–08:28 UT. The interval 08:31–08:40 UT was dominated by a southward B_z, whereas the interval 08:40–09:30 UT was dominated by a negative B_y. The solar wind speed in Figure 2b gradually increased from 400 to 450 km/s throughout the interval of interest. In Figure 2c, there was a three-step decrease in the proton density from 70 cm^{-3} at the beginning to 25 cm^{-3} by the end of the interval of interest. We also observe that the solar wind parameters do not fluctuate much between 08:50 and 09:30 UT.

In the ionosphere, the ESR 42 m beam sampled 32 ranges at ~77–470 km altitude along the magnetic field line, and the data were analyzed using a 60 s integration time. In Figure 2e and starting at 08:10 UT electron density enhancements exceeding 10^{11} m^{-3} were observed at altitudes above 250 km throughout the period of interest. The electron density enhancement is accompanied by corresponding electron temperature enhancements (Figure 2f) exceeding 3000 K at altitudes above 300 km within the same time interval, as well as ion upflow (not shown). The white vertical regions are data gaps due to lack of data, bad fits, or NEIALs. The MSP (Figure 2d) observed 630.0 nm dominated emissions from 08:10 UT and throughout the period of interest. The 557.7 nm intensity (not shown) was around 3 kR, whereas the 630.0 nm intensity reached above 20 kR. The emissions migrated from higher-latitude characteristic of type 2 aurora to latitudes characteristic

Journal of Geophysical Research: Space Physics 10.1002/2016JA023366

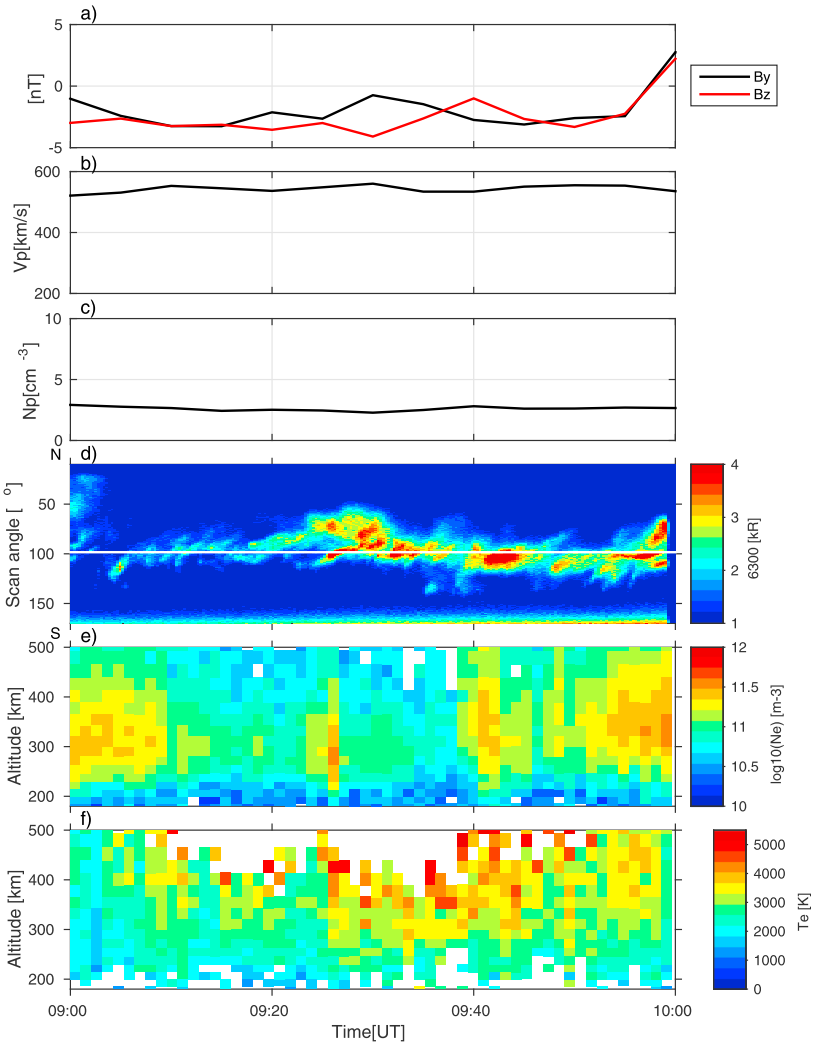

Figure 4. Solar wind and ionospheric data for event 2 on 14 January 2013. (a) The interplanetary magnetic field components B_y and B_z. (b) The solar wind speed. (c) The solar wind density. (d) Keogram from the meridian scanning photometer for the 630.0 nm emission line, and the white line indicates the location of the ESR 42 m beam. (e) Electron density profiles. (f) Electron temperature profiles.

of type 1 aurora [*Sandholt et al.*, 1998a] where it remained in the ESR 42 m field of view (white line) from 08:10 to 09:30 UT. The strongest 630.0 nm emission was observed between 09:05 and 09:25 UT. There were no observations from the MSP after 09:30 UT due to twilight.

Figure 3a displays the thermally excited O(^{1}D) 630.0 nm volume emission rate in Rayleighs per kilometer (R/km) calculated using equation (2). The 630.0 nm volume emission rate intensifies between 08:12 and 09:30 UT at altitudes above 250 km. The volume emission rate fluctuates possibly due to the horizontal

Journal of Geophysical Research: Space Physics 10.1002/2016JA023366

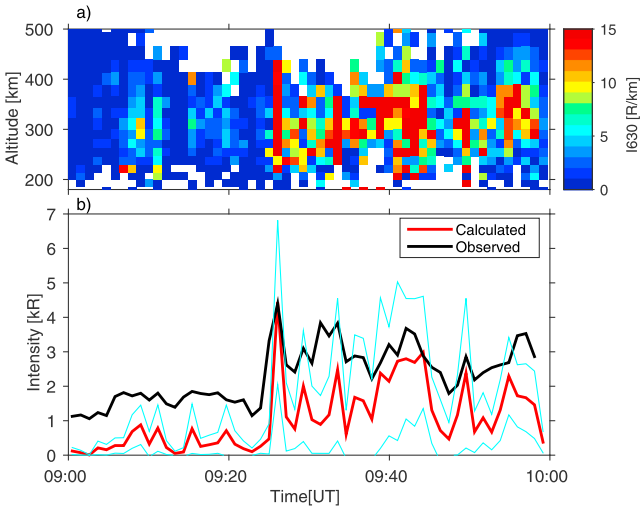

Figure 5. (a) The calculated volume emission rate versus height and (b) a comparison of the calculated thermal component with the MSP observations for event 2 on 14 January 2013. The cyan lines mark the upper and lower limits of the the error bars of the calculated thermal component.

motion of the aurora as a result magnetic reconnection events in the cusp [*Lockwood and Carlson*, 1992]. Using equation (3), we calculated the total column emission intensity resulting from the thermal excitation. Figure 3b shows the calculated thermal component and the total observed intensity from the MSP. After 08:15 UT, the thermal component on average contributes more than 50% of the total observed intensity by the MSP, which exceeds 10 kR at times.

3.2. Event 2: 14 January 2013

Our second event is 14 January 2013 between 09:00 and 10:00 UT. The solar wind and IMF conditions were more quiet. With regard to the solar wind, it is more of an average situation. Event 2 was characterized by a weak interplanetary magnetic field, high solar wind speed but low solar wind density. From Figure 4a, we see that B_z and B_y were ∼−3 nT most of the time. The solar wind speed (Figure 4b) is fairy stable between 520 and 560 km/s, while the proton density (Figure 4c) is ∼2.5 cm^{-3}.

In the ionosphere, the ESR recorded enhanced electron density (Figure 4e) exceeding 10^{11} m^{-3} accompanied by corresponding electron heating to a temperature exceeding 3000 K (Figure 4f) and ion upflow (not shown) at altitudes above 350 km. The white vertical regions are data gaps. Figure 4d shows the MSP keogram for the 630.0 nm emission, and we see that the emission remained in the field of view of the radar most of the time. The observed aurora was dominated by the 630.0 nm emission, which is an indication of soft electron precipitation and heating of the ambient electron gas. Higher intensity was observed after 09:25 UT. Figure 5a displays the calculated volume emission rate for the thermally excited 630.0 nm emission. Figure 5b presents the comparison of the calculated total column intensity with the MSP observations. Generally, we see that the thermal component was on average ∼2 kR after 09:25 UT which contributed to around 50% of the total observed 630.0 nm emission by the MSP in 200–400 km altitude.

4. Discussion

This study has been limited to 630 nm emissions resulting from excitation of the $O(^1D)$ state by the heated ambient electron gas. The other important source of the 630.0 nm emission in the cusp is direct impact excitation of the $O(^1D)$ state from particle precipitation. We also calculated the estimated contribution from dissociative recombination (not shown) which was negligible during the period of interest.

AGU Journal of Geophysical Research: Space Physics 10.1002/2016JA023366

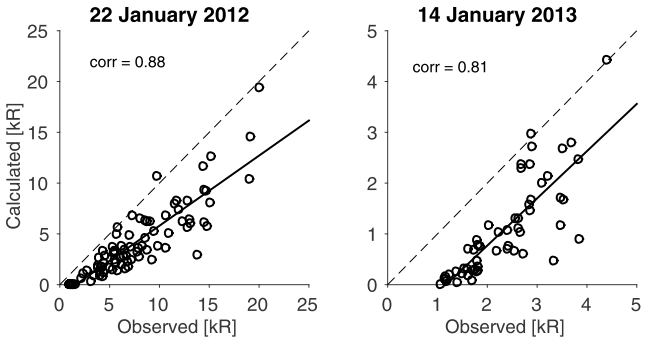

Figure 6. The calculated thermal component versus the total observed 630.0 nm MSP intensity on 22 January 2012 and 14 January 2013. The dashed line shows the one-to-one gradient line.

Wickwar and Kofman [1984] calculated the thermal component when the cusp was over Sondrestrom, and they measured high electron temperature. However, they did not have optical observations. *Carlson et al.* [2013] presented the first direct detection of the thermal component by applying the formula to ESR scan data and coincident all-sky images for the same latitudes as *Wickwar and Kofman* [1984]. We note that they used boundary tracking of the emission rate per kilometer altitude and not the total intensity. The scanning experiments of *Carlson et al.* [2013] are associated with large statistical error bars. In our study, we have used measurements from the fixed field-aligned 42 m ESR dish, which allows the data to be integrated in time in order to reduce statistical error bars at the expense of observation area. We made a general assumption that the thermal electron gas and the emitted thermal component remain in the ESR beam from excitation to emission of the 630.0 nm line. On this basis we have used the formula provided by *Carlson et al.* [2013] with smaller observational error bars, enabling us to better separate the thermal component from the total observed 630 nm intensities.

Figure 6 shows the correlation between the observed total emission and the calculated thermal component. The black line is a least squares fit to the compared intensities, with correlation coefficients of 0.88 and 0.81 for 22 January 2012 and 14 January 2013, respectively. The dotted line shows the slope of 1. This indicates that for both events the thermal component is a significant part of the observed 630.0 nm emission.

Carlson et al. [2013] emphasized magnetic reconnection as a major cause of electron heating in the cusp. During event 1, brief optical flashes were observed at 08:20:00, 08:25:30–08:26:00, and 08:32:00–08:35:00 UT in all-sky images from the University of Oslo camera at KHO (not shown). Unfortunately, these flashes were outside the field of view of the ESR and the MSP, so we could not test all the physical processes necessary for magnetic reconnection signatures [*Carlson*, 2012; *Carlson et al.*, 2004]. There were no optical flashes after 08.35:00 UT, which was mainly dominated by a strong B_y component, $B_z \sim 0$ nT, and intense 630.0 nm emissions in the ESR beam. Using the same data set, *Ronksley* [2016] reported episodes of strong neutral upwelling after 08:25 UT to the end of our study period. Between 08:43 and 08:53 UT while B_y changed from ~0 nT to ~−20 nT, the maximum vertical wind velocity of 200 ms^{-1} was reported [*Ronksley*, 2016, Figure 7.2c] which coincides with one of the periods when the calculated thermal component contributed ~100% of the observed emission. The soft particle precipitation from the previously reconnected magnetic filed line may be contributing to the heating process, but another physical process may be participating as well. Low-latitude dayside magnetopause reconnection is not favored for the period between 09:05 and 09:25 UT, although the highest intensity from the thermal component is observed then. The ambient electrons are clearly heated by another physical process during this period. Lobe cell magnetic reconnection is a possibility under such IMF configuration [*Sandholt et al.*, 1998b], but we would expect it to occur at higher latitudes than the ones we are looking at. We also do not expect precipitation from lobe cell reconnection to heat the ambient electron gas to such a high temperature as measured during the time of consideration. The ambient electrons could also be heated by ions when there is intense frictional heating in the *F* region. However, this requires that the ions are hotter than the electrons, yet for the period of interest here, the electrons are hotter than the ions.

AGU Journal of Geophysical Research: Space Physics 10.1002/2016JA023366

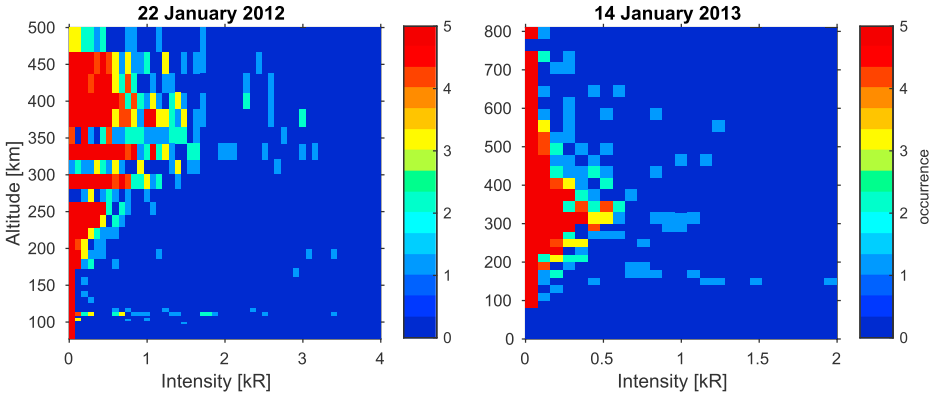

Figure 7. Occurrence of thermal emissions versus altitude and intensity for the events on 22 January 2012 and 14 January 2013.

Therefore, it is less likely for the ions to be the heating source of the ambient electrons. Given that event 1 is a highly disturbed period, as discussed above the specific heating process is not clear.

Event 2 had southward B_z with some 630 nm flashes both in the MSP and the all-sky images. An outstanding example but weak signature is seen in Figure 4 between 09:23 and 09:29 UT. During this period, a poleward moving auroral form [e.g., *Fasel*, 1995; *Sandholt and Farrugia*, 1999; *Milan et al.*, 2000; *Sandholt et al.*, 2004; *Oksavik et al.*, 2004; 2005; *Carlson et al.*, 2006; *Moen et al.*, 2008; *Lorentzen et al.*, 2010] crosses the ESR beam at 09:25 UT seen in the 630.0 nm keogram, and at the same time the electron density is enhanced below 200 km with an electron temperature enhancement near and above 300 km, all of which are signatures highlighted by *Carlson et al.* [2004] but not isolated from the background structure. Therefore, this event has greater possibility to be driven by magnetic reconnection pulses [*Carlson et al.*, 2004], but no clear signatures were confirmed. We also note that for both events the magnitude of B_y was greater than zero, and the greatest thermal component intensity was during event 1 on 22 January 2012 when B_z was northward. This emphasizes the effectiveness of the IMF B_y component in the high-latitude ionospheric processes as suggested in previous studies [e.g., *Knipp et al.*, 2011; *Li et al.*, 2011].

The peak emission altitude has an implication on the magnetic reconnection energy entering the cusp ionosphere, since the estimate of reconnection voltage varies as the square of the assumed emission altitude [*Lockwood et al.*, 1993]. An estimate of the altitude of the thermal component for both events is shown in Figure 7. Instead of integrating over the whole altitude of interest as in equation (3), we integrate over each range gate separately. Bins of intensity and altitudes are made. The occurrence of the resulting intensities at different altitudes is presented in Figure 7. We assume that the $O(^1D)$ below 250 km is greatly quenched. The altitude with the highest occurrence is used as the estimate for the peak emission altitude. The estimated peak emission altitude was 378 ± 35 km for event 1 and 330 ± 30 km for event 2. Theoretically, *Kozyra et al.* [1990] suggested that the emission altitude for the thermal component should be expected near 500 km which is higher than the estimated peak emission altitudes for the events studied here. However, the peak emission altitude for the event on 22 January 2012 is closer to 400–450 km reported by *Carlson et al.* [2013]. The estimated peak emission altitudes for both events studied in our work are in agreement with thermal component emission peak near 350 km reported by *Wickwar and Kofman* [1984]. As expected, the thermal component did not contribute to all the observed 630.0 nm emission, which implies that the total emission is due to a combination of different processes like direct impact excitation in addition to the thermal excitation. Hence, consistent with the fact that the precipitating soft electrons produce both thermal and impact emissions on the same flux tube, however, the peak emission altitude would differ [*Lockwood et al.*, 1993].

It is important to point out that the ESR 42 m data were checked for the whole dayside, but the thermal component only became significant when the cusp was over Svalbard. In the scanning experiment used by *Carlson et al.* [2013], thermally excited 630.0 nm emissions were also detected in the cusp sector. We note that

AGU Journal of Geophysical Research: Space Physics 10.1002/2016JA023366

we were limited to the winter period due to optical observations, but such events may in principal also exist in other seasons. We leave that for future work.

When we consider the errors associated with the measured electron temperature and electron density we get the upper and lower error boundaries in the calculated thermal component. These boundaries are indicated by the cyan lines in Figures 3 and 5. For event 1, the error boundaries do not deviate greatly from the final thermal component. However, for event 2 where the intensity is generally low the error boundaries are greater in comparison to the calculated thermal component. We have also assumed that the empirical atmospheric model produces reasonable results which is more uncertain for the disturbed ionospheric conditions [*Vickers et al.*, 2013]. A 20–30% underestimate of the atmospheric density at cusp latitudes from the empirical model was reported near solar maximum [*Liu and Lühr*, 2005; *Forbes et al.*, 2005]. Based on this, the contribution presented here is the lower limit. When we redo our analysis with an atomic oxygen density that is 30% higher than the model predictions, the resulting thermal excitation component will only be increased by 10–15%. Previous studies have also suggested that during large IMF B_y conditions, the empirical models may be unable to respond and hence could potentially underestimate the neutral density by 100% [e.g., *Crowley et al.*, 2010]. This further emphasizes that the atomic oxygen density used herein is the lower limit.

5. Summary and Conclusion

We have presented the first direct comparison between calculated thermally excited and observed 630 nm intensities. For the two events studied, the thermal component was highly correlated (correlation coefficient ~0.8) with the MSP observations with an average contribution of ~ 50% for both a disturbed and a relatively quiet cusp. The specific source of the electron gas heating is not certain, but the cooling by thermal excitation appears clear.

In agreement with earlier studies, the thermal component was significant when the electron temperature exceeded 3000 K with electron density enhancements between $(1-5) \times 10^{11}$ m^{-3} [*Egeland et al.*, 1992]. In agreement with earlier studies [*Carlson et al.*, 2013; *Johnsen et al.*, 2012; *Kozyra et al.*, 1990; *Egeland et al.*, 1992], our estimated emission altitude for the thermal component is higher than the generally accepted emission altitude of 225–250 km for the 630.0 nm emission [*Lockwood et al.*, 1993]. Our findings agree with *Egeland et al.* [1992] that the thermal excitation may be responsible for the 630.0 nm emission at 350 km and above.

Acknowledgments
The EISCAT data were accessed from https://www.eiscat.se and processed using GUISDAP. The Meridian Scanning Photometer (MSP) data at Kjell Henriksen Observatory (KHO) were provided by Dag Lorentzen. The interplanetary magnetic field and solar wind data were provided by the NASA OMNIWeb service (https:omniweb.gsfc.nasa.gov/). The NRLMSISE-00 Atmospheric model was accessed from https://ccmc.gsfc.nasa.gov/modelweb/models/nrlmsise00.php. This project has been funded by the Norwegian Research Council under contracts 223252 and 212014.

References

Carlson, H. C. (2012), Sharpening our thinking about polar cap ionospheric patch morphology, research, and mitigation techniques, *Radio Sci.*, *47*, RS0L21, doi:10.1029/2011RS004946.
Carlson, H. C., K. Oksavik, J. Moen, and T. Pedersen (2004), Ionospheric patch formation: Direct measurements of the origin of a polar cap patch, *Geophys. Res. Lett.*, *31*, L08806, doi:10.1029/2003GL018166.
Carlson, H. C., J. Moen, K. Oksavik, C. P. Nielsen, I. W. McCrea, T. R. Pedersen, and P. Gallop (2006), Direct observations of injection events of subauroral plasma into the polar cap, *Geophys. Res. Lett.*, *33*, L05103, doi:10.1029/2005GL025230.
Carlson, H. C., K. Oksavik, and J. I. Moen (2013), Thermally excited 630.0 nm O(1D) emission in the cusp: A frequent high-altitude transient signature, *J. Geophys. Res. Space Physics*, *118*, 5842–5852, doi:10.1002/jgra.50516.
Cogger, L., J. Walker, J. Meriwether, and R. Burnside (1980), F region airglow: Are ground-based observations consistent with recent satellite results?, *J. Geophys. Res. Space Physics*, *85*(A6), 3013–3020, doi:10.1029/JA085iA06p03013.
Collis, P. N., L. Häggström, K. Kaila, and M. T. Rietveld (1991), EISCAT radar observations of enhanced incoherent scatter spectra; Their relation to red aurora and field-aligned currents, *Geophys. Res. Lett.*, *18*(6), 1031–1034, doi:10.1029/91GL00848.
Crowley, G., D. J. Knipp, K. A. Drake, J. Lei, E. Sutton, and H. Lühr (2010), Thermospheric density enhancements in the dayside cusp region during strong B_y conditions, *Geophys. Res. Lett.*, *37*, L07110, doi:10.1029/2009GL042143.
Doering, J., and E. Gulcicek (1989), Absolute differential and integral electron excitation cross sections for atomic oxygyen.7. The $^3P \rightarrow {}^1D$ and $^3P \rightarrow {}^1S$ transitions from 4.0 to 30-eV, *J. Geophys. Res.*, *94*, 1541–1546, doi:10.1029/JA094iA02p01541.
Eather, R., S. Mende, and E. Weber (1979), Dayside aurora and relevance to substorm current systems and dayside merging, *J. Geophys. Res. Space Physics*, *84*(NA7), 3339–3359, doi:10.1029/JA084iA07p03339.
Egeland, A., H. C. Carlson, W. F. Denig, K. Fukui, and E. Weber (1992), Day-side auroral signatures based on simultaneous, coordinated observations at Svalbard and Greenland, *IEEE Trans. Plasma Sci.*, *20*(6), 726–739, doi:10.1109/27.199521.
Fasel, G. J. (1995), Dayside poleward moving auroral forms: A statistical study, *J. Geophys. Res.*, *100*(A7), 11,891–11,905, doi:10.1029/95JA00854.
Forbes, J. M., G. Lu, S. Bruinsma, S. Nerem, and X. Zhang (2005), Thermosphere density variations due to the 15–24 April 2002 solar events from CHAMP/STAR accelerometer measurements, *J. Geophys. Res.*, *110*, A12S27, doi:10.1029/2004JA010856.
Foster, J. C., C. del Pozo, K. Groves, and J.-P. St. Maurice (1988), Radar observations of the onset of current driven instabilities in the topside ionosphere, *Geophys. Res. Lett.*, *15*(2), 160–163, doi:10.1029/GL015i002p00160.
Johnsen, M. G., D. A. Lorentzen, J. M. Holmes, and U. P. Løvhaug (2012), A model based method for obtaining the open/closed field line boundary from the cusp auroral 6300-Å[OI] red line, *J. Geophys. Res.*, *117*, A03319, doi:10.1029/2011JA016980.
Knipp, D., S. Eriksson, L. Kilcommons, G. Crowley, J. Lei, M. Hairston, and K. Drake (2011), Extreme Poynting flux in the dayside thermosphere: Examples and statistics, *Geophys. Res. Lett.*, *38*, L16102, doi:10.1029/2011GL048302.

AGU Journal of Geophysical Research: Space Physics 10.1002/2016JA023366

Kontar, E. P., and H. L. Pécseli (2005), Nonlinear wave interactions as a model for naturally enhanced ion acoustic lines in the ionosphere, *Geophys. Res. Lett.*, *32*, L05110, doi:10.1029/2004GL022182.

Kozyra, J. U., C. E. Valladares, H. C. Carlson, M. J. Buonsanto, and D. W. Slater (1990), A theoretical study of the seasonal and solar cycle variations of stable aurora red arcs, *J. Geophys. Res.*, *95*(A8), 12,219–12,234, doi:10.1029/JA095iA08p12219.

Lan, V. K., N. Feautrier, M. L. Dourneuf, and H. V. Regemorter (1972), Cross sections calculations for electron-oxygen scattering using the polarized orbital close coupling theory, *J. Phys. B: At. Mol. Phys.*, *5*(8), 1506–1516, doi:10.1088/0022-3700/5/8/016.

Lehtinen, M. S., and A. Huuskonen (1996), General incoherent scatter analysis and GUISDAP, *J. Atmos. Terr. Phys.*, *58*(1), 435–452, doi:10.1016/0021-9169(95)00047-X.

Li, W., D. Knipp, J. Lei, and J. Raeder (2011), The relation between dayside local Poynting flux enhancement and cusp reconnection, *J. Geophys. Res.*, *116*, A08301, doi:10.1029/2011JA016566.

Liu, H., and H. Lühr (2005), Strong disturbance of the upper thermospheric density due to magnetic storms: CHAMP observations, *J. Geophys. Res.*, *110*, A09S29, doi:10.1029/2004JA010908.

Lockwood, M., and H. C. Carlson (1992), Production of polar cap electron density patches by transient magnetopause reconnection, *Geophys. Res. Lett.*, *19*(17), 1731–1734, doi:10.1029/92GL01993.

Lockwood, M., H. C. Carlson, and P. E. Sandholt (1993), Implications of the altitude of transient 630-nm dayside auroral emissions, *J. Geophys. Res.*, *98*(A9), 15,571–15,587, doi:10.1029/93JA00811.

Lorentzen, D. A., J. Moen, K. Oksavik, F. Sigernes, Y. Saito, and M. G. Johnsen (2010), In situ measurement of a newly created polar cap patch, *J. Geophys. Res.*, *115*, A12323, doi:10.1029/2010JA015710.

Lunde, J., B. Gustavsson, U. P. Løvhaug, D. A. Lorentzen, and Y. Ogawa (2007), Particle precipitations during NEIAL events: Simultaneous ground based observations at Svalbard, *Ann. Geophys.*, *25*(6), 1323–1336, doi:10.5194/angeo-25-1323-2007.

Mantas, G. P. (1994), Large 6300-AA airglow intensity enhancements observed in ionosphere heating experiments are excited by thermal electrons, *J. Geophys. Res.*, *99*(A5), 8993–9002, doi:10.1029/94JA00347.

Mantas, G. P., and H. C. Carlson (1991), Reexamination of the $O(^3P \rightarrow {}^1D)$ excitation rate by thermal electron impact, *Geophys. Res. Lett.*, *18*(2), 159–162, doi:10.1029/91GL00019.

Meier, R. R., D. J. Strickland, J. H. Hecht, and A. B. Christensen (1989), Deducing composition and incident electron spectra from ground-based auroral optical measurements: A study of auroral red line processes, *J. Geophys. Res.*, *94*(A10), 13,541–13,552, doi:10.1029/JA094iA10p13541.

Michell, R., and M. Samara (2013), Observability of NEIALs with the Sondrestrom and Poker Flat incoherent scatter radars, *J. Atmos. Sol. Terr. Phys.*, *105–106*, 299–307, doi:10.1016/j.jastp.2012.12.008.

Michell, R. G., K. A. Lynch, C. J. Heinselman, and H. C. Stenbaek-Nielsen (2009), High time resolution PFISR and optical observations of naturally enhanced ion acoustic lines, *Ann. Geophys.*, *27*(4), 1457–1467, doi:10.5194/angeo-27-1457-2009.

Milan, S. E., M. Lester, S. W. H. Cowley, and M. Brittnacher (2000), Convection and auroral response to a southward turning of the IMF: Polar UVI, CUTLASS, and IMAGE signatures of transient magnetic flux transfer at the magnetopause, *J. Geophys. Res.*, *105*(A7), 15,741–15,755, doi:10.1029/2000JA900022.

Moen, J., Y. Rinne, H. C. Carlson, K. Oksavik, R. Fujii, and H. Opgenoorth (2008), On the relationship between thin Birkeland current arcs and reversed flow channels in the winter cusp/cleft ionosphere, *J. Geophys. Res.*, *113*, A09220, doi:10.1029/2008JA013061.

Newell, P. T., and C.-I. Meng (1988), The cusp and the cleft/boundary layer: Low-altitude identification and statistical local time variation, *J. Geophys. Res.*, *93*(A12), 14,549–14,556, doi:10.1029/JA093iA12p14549.

Newell, P. T., and C.-I. Meng (1992), Mapping the dayside ionosphere to the magnetosphere according to particle precipitation characteristics, *Geophys. Res. Lett.*, *19*(6), 609–612, doi:10.1029/92GL00404.

Newell, P. T., and C.-I. Meng (1994), Ionospheric projections of magnetospheric regions under low and high solar wind pressure conditions, *J. Geophys. Res.*, *99*(A1), 273–286, doi:10.1029/93JA02273.

Ogawa, Y., S. C. Buchert, R. Fujii, S. Nozawa, and F. Forme (2006), Naturally enhanced ion-acoustic lines at high altitudes, *Ann. Geophys.*, *24*(12), 3351–3364, doi:10.5194/angeo-24-3351-2006.

Oksavik, K., J. Moen, and H. C. Carlson (2004), High-resolution observations of the small-scale flow pattern associated with a poleward moving auroral form in the cusp, *Geophys. Res. Lett.*, *31*, L11807, doi:10.1029/2004GL019838.

Oksavik, K., J. Moen, H. C. Carlson, R. A. Greenwald, S. E. Milan, M. Lester, W. F. Denig, and R. J. Barnes (2005), Multi-instrument mapping of the small-scale flow dynamics related to a cusp auroral transient, *Ann. Geophys.*, *23*(7), 2657–2670, doi:10.5194/angeo-23-2657-2005.

Picone, J. M., A. E. Hedin, D. P. Drob, and A. C. Aikin (2002), NRLMSISE-00 empirical model of the atmosphere: Statistical comparisons and scientific issues, *J. Geophys. Res.*, *107*(A12), 1468, doi:10.1029/2002JA009430.

Rees, M., J. C. Walker, and A. Dalgarno (1967), Auroral excitation of the forbidden lines of atomic oxygen, *Planet. Space Sci.*, *15*(7), 1097–1110, doi:10.1016/0032-0633(67)90096-7.

Rietveld, M. T., P. N. Collis, and J.-P. St.-Maurice (1991), Naturally enhanced ion acoustic waves in the auroral ionosphere observed with the EISCAT 933-MHz radar, *J. Geophys. Res.*, *96*(A11), 19,291–19,305, doi:10.1029/91JA01188.

Romick, G. J. (1976), The detection and study of the visible spectrum of the aurora and airglow, *Proc. SPIE*, *0091*, 63–70, doi:10.1117/12.955072.

Ronksley, A. (2016), Optical remote sensing of mesoscale thermospheric dynamics above Svalbard and Kiruna, PhD thesis, Univ. College London.

Sandholt, P. E., and C. J. Farrugia (1999), On the dynamic cusp aurora and IMF B_y, *J. Geophys. Res.*, *104*(A6), 12,461–12,472, doi:10.1029/1999JA900126.

Sandholt, P. E., C. J. Farrugia, J. Moen, Ø. Noraberg, B. Lybekk, T. Sten, and T. Hansen (1998a), A classification of dayside auroral forms and activities as a function of interplanetary magnetic field orientation, *J. Geophys. Res.*, *103*(A10), 23,325–23,345, doi:10.1029/98JA02156.

Sandholt, P. E., C. J. Farrugia, and S. W. H. Cowley (1998b), Pulsating cusp aurora for northward interplanetary magnetic field, *J. Geophys. Res.*, *103*(A11), 26,507–26,520, doi:10.1029/98JA02433.

Sandholt, P. E., C. J. Farrugia, and W. F. Denig (2004), Dayside aurora and the role of IMF $|B_{z|/|}B_z|$: Detailed morphology and response to magnetopause reconnection, *Ann. Geophys.*, *22*(2), 613–628, doi:10.5194/angeo-22-613-2004.

Schlatter, N. M., N. Ivchenko, T. Sergienko, B. Gustavsson, and B. U. E. Brändström (2013), Enhanced EISCAT UHF backscatter during high-energy auroral electron precipitation, *Ann. Geophys.*, *31*(10), 1681–1687, doi:10.5194/angeo-31-1681-2013.

Schlatter, N. M., V. Belyey, B. Gustavsson, N. Ivchenko, D. Whiter, H. Dahlgren, S. Tuttle, and T. Grydeland (2015), Auroral ion acoustic wave enhancement observed with a radar interferometer system, *Ann. Geophys.*, *33*(7), 837–844, doi:10.5194/angeo-33-837-2015.

Schunk, R. W., and A. F. Nagy (1978), Electron temperatures in the F region of the ionosphere: Theory and observations, *Rev. Geophys.*, *16*(3), 355–399, doi:10.1029/RG016i003p00355.

AGU Journal of Geophysical Research: Space Physics 10.1002/2016JA023366

Solomon, S. C., P. B. Hays, and V. J. Abreu (1988), The auroral 6300 Å emission: Observations and modeling, *J. Geophys. Res. Space Physics*, *93*(A9), 9867–9882, doi:10.1029/JA093iA09p09867.

Strømme, A., V. Belyey, T. Grydeland, C. La Hoz, U. P. Løvhaug, and B. Isham (2005), Evidence of naturally occurring wave-wave interactions in the polar ionosphere and its relation to naturally enhanced ion acoustic lines, *Geophys. Res. Lett.*, *32*, L05103, doi:10.1029/2004GL020239.

Thomas, L. D., and R. K. Nesbet (1975), Low-energy electron scattering by atomic oxygen, *Phys. Rev. A*, *11*, 170–173, doi:10.1103/PhysRevA.11.170.

Vickers, H., M. J. Kosch, E. Sutton, Y. Ogawa, and C. La Hoz (2013), Thermospheric atomic oxygen density estimates using the EISCAT Svalbard radar, *J. Geophys. Res. Space Physics*, *118*, 1319–1330, doi:10.1002/jgra.50169.

Wickwar, V. B., and W. Kofman (1984), Dayside red auroras at very high latitudes: The importance of thermal excitation, *Geophys. Res. Lett.*, *11*(9), 923–926, doi:10.1029/GL011i009p00923.

II

Paper II

How often do thermally excited 630.0 nm emissions occur in the polar ionosphere?

N. K. Kwagala, K. Oksavik, D. A. Lorentzen, and M. G. Johnsen

Journal of Geophysical Research, Vol. 123, doi:10.1002/2017JA024744 (2018)

AGU PUBLICATIONS

JGR

Journal of Geophysical Research: Space Physics

RESEARCH ARTICLE
10.1002/2017JA024744

Key Points:
- Thermally excited emissions maximize in the cusp around magnetic noon
- Peak occurrence at electron temperatures exceeding 3000 K
- Peak occurrence at electron densities exceeding 5×10^{11} m^{-3} for lower electron temperatures (2300–3000 K)

Correspondence to:
N. K. Kwagala,
norah.kwagala@uib.no

Citation:
Kwagala, N. K., Oksavik, K., Lorentzen, D. A., & Johnsen, M. G. (2017). How often do thermally excited 630.0 nm emissions occur in the polar ionosphere? *Journal of Geophysical Research: Space Physics*, *122*. https://doi.org/10.1002/2017JA024744

Received 5 SEP 2017
Accepted 28 NOV 2017
Accepted article online 18 DEC 2017

How Often Do Thermally Excited 630.0 nm Emissions Occur in the Polar Ionosphere?

Norah Kaggwa Kwagala[1,2], Kjellmar Oksavik[1,2,3], Dag A. Lorentzen[2], and Magnar G. Johnsen[4]

[1]Birkeland Centre for Space Science, University of Bergen, Bergen, Norway, [2]Birkeland Centre for Space Science, University Centre in Svalbard, Longyearbyen, Norway, [3]Now at Center for Space Science and Engineering Research (Space@VT), Virginia Polytechnic Institute and State University, Blacksburg, VA, USA, [4]Tromsø Geophysical Observatory, UiT-Arctic University of Norway, Tromso, Norway

Abstract This paper studies thermally excited emissions in the polar ionosphere derived from European Incoherent Scatter Svalbard radar measurements from the years 2000–2015. The peak occurrence is found around magnetic noon, where the radar observations show cusp-like characteristics. The ionospheric, interplanetary magnetic field and solar wind conditions favor dayside magnetic reconnection as the dominant driving process. The thermal emissions occur 10 times more frequently on the dayside than on the nightside, with an average intensity of 1–5 kR. For typical electron densities in the polar ionosphere (2×10^{11} m^{-3}), we find the peak occurrence rate to occur for extreme electron temperatures (>3000 K), which is consistent with assumptions in literature. However, for extreme electron densities ($> 5 \times 10^{11}$ m^{-3}), we can now report on a completely new population of thermal emissions that may occur at much lower electron temperatures (~2300 K). The empirical atmospheric model (NRLMSISE-00) suggests that the latter population is associated with enhanced neutral atomic oxygen densities.

1. Introduction

The 630.0 and 557.7 nm lines are common emissions in the polar ionosphere, both arising from the excited states of atomic oxygen ^{1}D and ^{1}S, respectively. The lower energy ^{1}D state makes the 630.0 nm a possible emission from low-energy processes like thermal excitation. Thermal excitation of atomic oxygen in the polar ionosphere can sometimes lead to noticeable 630.0 nm emission intensities (i.e, exceeding 1 kR). This happens when the ambient electron gas is heated. If there are enough electrons in the high-energy tail of the energy distribution exceeding 1.96 eV, then the electron gas may cool by exciting atomic oxygen to the ^{1}D state, which then emits 630.0 nm photons on deexcitation. In the polar ionosphere the soft precipitating electrons are believed to be the heating source of the ambient electron gas. More detailed explanations of the theory of thermal excitation can be found in literature (e.g., Carlson et al., 2013; Kozyra et al., 1990; Kwagala et al., 2017; Lockwood, Carlson, & Sandholt, 1993; Wickwar & Kofman, 1984).

Thermally excited 630.0 nm emissions in the cusp have been reported in a number of case studies (e.g., Carlson et al., 2013; Johnsen et al., 2012; Kwagala et al., 2017; Wickwar & Kofman, 1984). To our knowledge, no studies have investigated thermally excited emissions outside the cusp region or in a statistical sense. The aim of our study is therefore to obtain a broader understanding of the overall role of thermally excited emissions in the polar ionosphere.

Our study sets out to statistically analyze the occurrence of thermal emissions in the polar ionosphere based on data from the European Incoherent Scatter (EISCAT) Svalbard Radar for the years of 2000 to 2015. Our objective is to identify when and where thermal emissions are potentially important for analyses, interpretations, and modeling of auroral emissions in the polar ionosphere.

Our approach is described in section 2, and our observations are presented in section 3. Our discussion and conclusions are found in sections 4 and 5.

2. Approach

This study is based on ionospheric measurements of electron temperature and electron density by the EISCAT Svalbard Radar (ESR) during the years from 2000 to 2015. ESR is located at 445 m altitude, 75.12°N magnetic latitude, and magnetic local time is UT + 3 (geographic coordinates: 78.15°N, 16.02°E). In order to get an

AGU Journal of Geophysical Research: Space Physics 10.1002/2017JA024744

Table 1
An Overview of Time and Altitude Resolutions for the EISCAT Experiments Used in This Study

			Raw data		Processed data	
Year	Experiment name	Altitude coverage	Time resolution	Altitude resolution	Time resolution	Altitude resolution
		(km)	(s)	(km)	(s)	(km)
2000–2003	tau0	53–1144	6.4	3.0	64–128	3–37
2004–2006	steffe	34–800	6.0	2.2	60–120	3.7–30
2007–2015	ipy	28–383	6.0	2.2	60–120	3.7–30
		388–509		4.5		

unbiased database, we only use experiments for which the radar ran continuously for approximately 24 h. Measurements from the fixed magnetic field-aligned 42 m parabolic dish are used. ESR has a number of standard experiments through which measurements can be made. An overview of typical experiments in our database is shown in the Table 1. A postintegration time of 1–2 min was used for the postanalysis. The raw data consist of lag profiles that have been preintegrated for a few seconds. The processed data are postintegrated data for longer periods (e.g., 1–2 min) using the Grand Unified Incoherent Scatter Design and Analysis Package (GUISDAP) (Lehtinen & Huuskonen, 1996).

The Naval Research Laboratory Mass Spectrometer and Incoherent Scatter Radar 2000 model (NRLMSISE-00) (Picone et al., 2002) was used to generate the number density of atomic oxygen. We obtained the solar wind and interplanetary field (IMF) parameters from the GSFC/SPDF OMNI database. This data is already time shifted to the magnetopause. The GSM coordinates and 1 h averages were used. The solar wind dynamic pressure (P) is given by $P = M{\times}N_p \times V_p^2$, where M is the proton mass, N_p is the solar wind density, and V_p is the solar wind speed. All data used in the present study was obtained through the Madrigal database which is composed of upper atmospheric scientific data.

Mantas and Carlson (1991) reassessed different values of cross sections provided in literature (e.g., Doering and Gulcicek, 1989; Henry et al., 1969; Lan et al., 1972; Thomas and Nesbet, 1975). An earlier excitation rate, based on the cross section by Henry et al. (1969), was derived by Link (1982) and was used in some studies (e.g., Solomon et al., 1988). Mantas and Carlson (1991) found that the rates derived from the cross section by Henry et al. (1969) and Lan et al. (1972) were almost identical for practical purposes, but the cross section by Lan et al. (1972) appeared more complete based on theoretical grounds and was therefore recommended. Based on these recommendations, Carlson et al. (2013) provided a set of formulae that can be applied to incoherent scatter radar measurements to calculate and separate thermally excited 630.0 nm emissions from the total 630.0 nm emissions.

In the current study, a numerical model employing the formulae provided by Carlson et al. (2013) is used to derive the thermally excited emission rates and total intensity. For electron density N_e, electron temperature T_e, and atomic oxygen density N_o, the volume emission rate is given by

$$I_{630}(h) = \alpha\left[T_e(h)\right] \times N_o(h) \times N_e(h) \quad \text{(Rayleighs/km)} \tag{1}$$

where

$$\alpha(T_e) = 0.15 \times \sqrt{T_e} \times \frac{(8537 + T_e)}{(34191 + T_e)^3} \times e^{\left(\frac{-22756}{T_e}\right)} \quad (\text{cm}^3/\text{s}) \tag{2}$$

and the total vertical column intensity is found by integrating the volume emission rate along the line of sight

$$I_{630} = \int_{250\text{km}}^{650\text{km}} I_{630}(h)\mathrm{d}h \quad \text{(Rayleighs)} \tag{3}$$

Mantas and Carlson (1991) provided equation (2) based on cross section by Lan et al. (1972), whereas Carlson et al. (2013) provided equations (1) and (3). All the parameters, N_e, T_e, and N_o are functions of the altitude h in kilometers. N_e and N_o are measured in cm^{-3} and T_e in Kelvin.

After generating the emission rates for the whole data set, we analyze the intensities for occurrence rate and probability. First, we categorize our data into two categories: strong and weak thermal components.

Journal of Geophysical Research: Space Physics 10.1002/2017JA024744

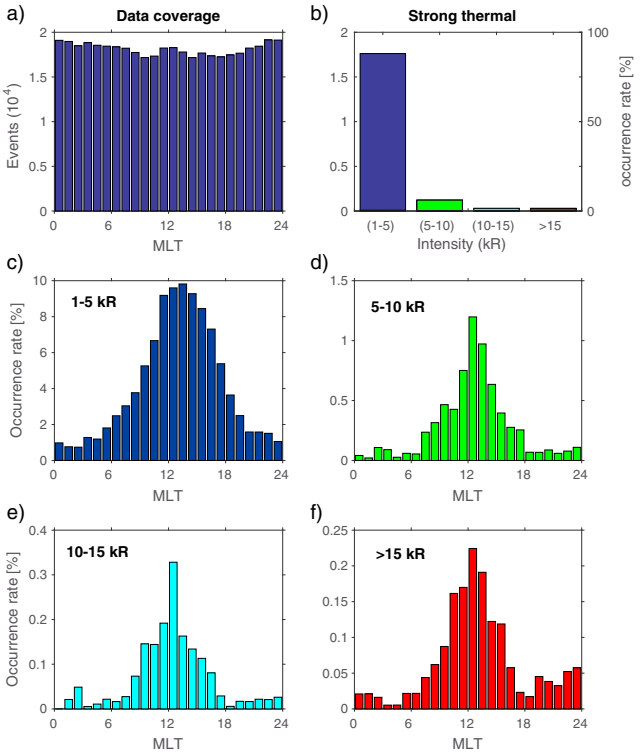

Figure 1. (a) Data coverage for the study with respect to magnetic local time. The data consists of ESR 42 m experiments that ran continuously for approximately 24 h during the years 2000–2015. (b) The occurrence rate of different intensity categories of 1–5, 5–10, 10–15, and >15 kR and the vertical axis on the left shows the number of events, while that on the right shows the occurrence rate in percentage. The magnetic local time distribution of the intensity categories for (c) 1–5, (d) 5–10, (e) 10–15, and (f) >15 kR, respectively. The vertical axes show the occurrence rate.

The "strong thermal" refers to all results which give a total intensity of 1 kR or more, whereas the "weak thermal" refers to all the remaining data (i.e., with a total intensity less than 1 kR).

Chamberlain (1961) described typical intensity levels as 250 R for airglow and 1 kR for aurora emissions. The 1 kR has since been used in studies as a threshold for emissions generally assumed to be associated with direct impact excitation by precipitating particles (e.g., Frank & Craven, 1988; Kamide et al., 1999; Sims et al., 2012). In addition, the distributions of ionospheric parameters were almost the same when the threshold was raised above 1 kR but varied when lower thresholds were used. In our study, the focus is on the strong thermal component, and we consider the thermal excitation to be significant if it exceeds the airglow intensity levels and produces aurora intensity levels. For this reason we use a 1 kR threshold to separate out the strong thermal component.

We further analyze the ionospheric, solar wind and interplanetary magnetic field parameters during the two categories and for different magnetic local times (MLT).

3. Observations and Results

A general overview of the data used in the study is presented in Figure 1. Figure 1a shows the magnetic local time distribution of the data coverage. There is a relatively even distribution at all magnetic local times. In addition to the data coverage in Figure 1a, the distribution of the strong thermal component intensities is shown

Journal of Geophysical Research: Space Physics 10.1002/2017JA024744

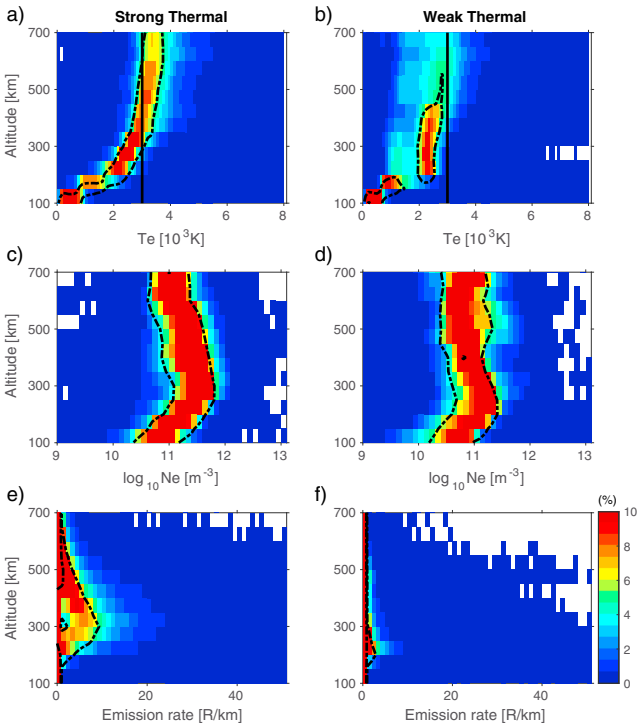

Figure 2. Distribution of electron temperature (T_e), electron density (N_e), and the calculated volume emission rate of the thermally excited 630.0 nm, respectively, normalized at each altitude step. (a, c, and e) The parameters associated with the strong thermally excited emission (>1 kR). (b, d, and f) The parameters associated with the weak thermally excited emissions (<1 kR). The color bar indicates the relative distribution in percentage. The black dotted line marks the 5% level. The black vertical lines in Figures 2a and 2b mark 3000 K.

in Figure 1b. The bins in Figure 1b contain data points with intensities 1–5, 5–10, 10–15, and >15 kR from left to right, respectively. Each bin in Figures 1a and 1c–1f contains data points for 1 h MLT. Figure 1b shows that the 1–5 kR bin contains ~85% of the strong thermal component. The MLT distribution of the intensity bins in Figure 1b is given in Figures 1c–1f, respectively. From Figure 1c which is representative of the strong thermal component, we see that generally, the occurrence rate is higher on the dayside (06:00–18:00 MLT) compared to the nightside (18:00–06:00). The peak occurrence rate is observed near magnetic noon, where ~10% of the data have a strong thermal component, which is 10 times higher than the occurrence rate found on the nightside. All the intensity categories show a similar MLT distribution with the 1–5 kR as the dominant intensity level.

We now analyze the distributions of measured electron temperature, density, and calculated thermal excitation rates at different altitudes. Figure 2 shows the distribution of electron temperature (T_e), electron density (N_e), and volume emission rate normalized at each 50 km altitude step, for the strong thermal events (a, c, e) and weak thermal events (b, d, f). The black dotted line marks the 5% level of the distribution, while the vertical black lines in Figures 2a and 2b mark 3000 K. The electron temperature is generally low at the low altitudes for both weak and strong thermal component (Figures 2a and 2b) distributions, and both distributions are similar. At higher altitudes (>250 km), however, the two distributions become different with the weak thermal component temperature mainly remaining low (below 3000 K) and the strong thermal component temperature exceeds 3000 K. Similarly, there is no big difference in the electron density at low altitudes, but at higher altitudes, the electron density associated with the strong thermal component is generally higher than that

Journal of Geophysical Research: Space Physics 10.1002/2017JA024744

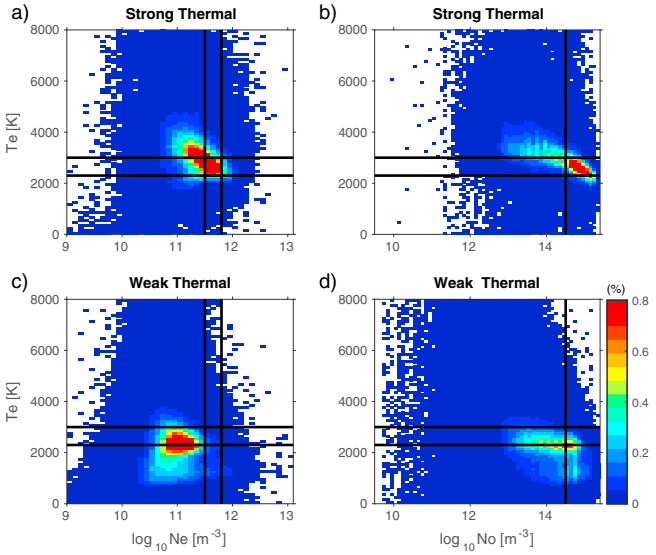

Figure 3. Distribution of densities associated with the strong and weak thermal populations at different electron temperatures. (a and c) The electron density distributions. (b and d) The modeled neutral atomic oxygen densities. The two vertical lines in Figures 3a and 3c mark electron density 5×10^{11} and 8×10^{11} m^{-3}, respectively, while that in Figures 3b and 3d marks atomic oxygen number density 5×10^{14} m^{-3}. The two horizontal lines mark electron temperature 2300 and 3000 K, respectively, in all the panels. The color bar shows the distribution in percentage.

associated with the weak thermal component population. The derived thermal excitation emission rates are shown in Figures 2e and 2f. This was calculated for both weak and strong thermal distributions in order to get a general picture and comparison between the two. From the presented weak thermal component distribution (Figure 2f), we notice that the peak occurrence rate is at less than 1 R/km at all altitudes, and the distribution generally extends to 5 R/km. On the other hand, the strong thermal emission rate distribution (Figure 2e) below 250 km is less than 1 R/km as well but it is enhanced at altitudes above 250 km. The highest emission rate is found at 300–350 km altitude for the strong thermal component.

The distribution of the electron and modeled atomic oxygen densities at different electron temperatures for both strong and weak thermal populations is presented in Figure 3. The color bar gives the distribution in percentage. The black horizontal lines mark the 2300 and 3000 K electron temperatures. The two vertical lines in Figures 3a and 3c mark electron density $5{\times}10^{11}$ and $8{\times}10^{11}$ m^{-3}, respectively, while that in Figures 3b and 3d marks atomic oxygen number density 5×10^{14} m^{-3}, respectively. The peak population is found between 2300 and 4000 K for electron density, and the model suggests that the peak population for the neutral atomic oxygen is only between 2300 and 3000 K for the strong thermal component distributions (Figures 3a and 3b). The peak population we find below 3000 K is unexpected. On comparison with the weak thermal component distribution, both the electron and modeled neutral atomic oxygen densities peak at relatively lower densities and electron temperatures compared to the strong thermal component distribution. When we normalize the densities at each electron temperature step, we get the distributions in Figure 4. The region with the peak populations in the strong thermal distributions just show very low occurrence in the weak thermal distributions, particularly for the regions enclosed by all the four (three) lines in the four panels.

Figure 5 shows the probability of having strong thermally excited emissions given the different electron temperature, density, atomic oxygen density, emission rates, and altitudes. The two horizontal lines mark the same temperatures as in the previous two figures. The same temperature levels are marked by the vertical lines in Figure 5c. Generally, Figure 5 shows the probability for strong thermally excited emissions to occur

Journal of Geophysical Research: Space Physics 10.1002/2017JA024744

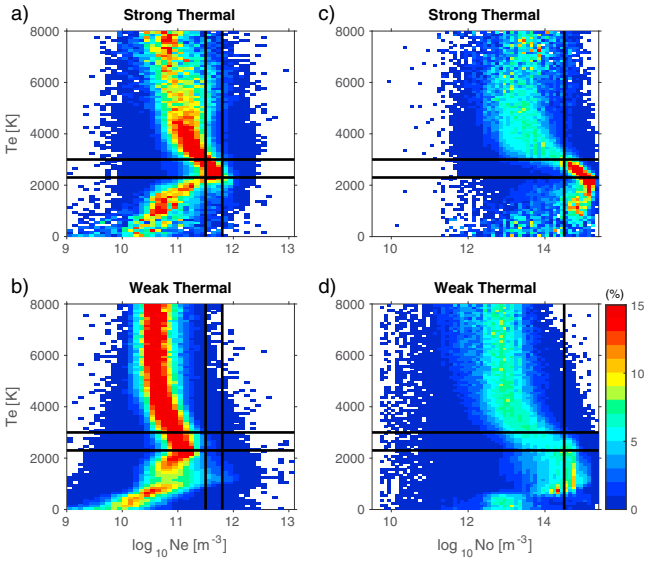

Figure 4. Normalized distribution of (a, c) electron density and (b, d) modeled neutral atomic oxygen density in each electron temperature step. The two vertical lines in Figures 4a and 4c mark electron density 5×10^{11} and 8×10^{11} m^{-3}, respectively, while that in Figures 4b and 4d marks atomic oxygen number density 5×10^{14} m^{-3}. The two horizontal lines mark electron temperature 2300 and 3000 K, respectively, in all the panels. The color bar shows the distribution in percentage.

to be high when electron temperature exceeds 2300 K, electron density exceeds 2×10^{11}, and the model suggests neutral atomic oxygen density exceeding 1×10^{14} m^{-3} for altitudes above 250 km.

We now analyze the prevailing interplanetary magnetic field and solar wind conditions during the strong thermally excited emissions which are then compared to the occurrence for the full data set. Figure 6 shows the occurrence rate of IMF B_y, B_z, and B_x for the full data set (a, c, e). Figures 6b, 6d, and 6f show the percentage of the full data set (a, c, e) which is simultaneous with a strong thermal component in the ionosphere. Of the simultaneous IMF components, negative B_z shows the highest occurrence rate (see Figure 6d) while the positive B_z shows a higher occurrence rate than the near-zero values. There is no difference in occurrence rate seen in the different configurations of B_x. Also, nonzero B_y shows a higher occurrence rate compared to the near-zero B_y. Figure 7 has the same structure as Figure 6 but instead shows the solar wind parameters: solar wind density, speed, and dynamic pressure, from top to bottom, respectively. For these solar wind parameters, the relatively high dynamic pressure shows the highest occurrence rate (see Figure 7f) followed by the high solar wind density and solar wind speed.

4. Discussion

A few case studies on thermal excitation have been done in the past. In some studies thermal excitation has been suggested as the possible source for observed emissions, whereas other theoretical studies have provided theoretical explanations for the same process. Intense 630.0 nm emissions associated with enhanced electron temperature and density have been reported at high latitudes centered at magnetic noon, since four decades ago (e.g., Shepherd, 1979). In efforts of understanding these emissions, Wickwar and Kofman (1984) investigated and calculated the thermal component during the periods of enhanced electron temperature and found that thermal excitation dominated the production of the 630.0 nm emission. However, due to the sunlit conditions, they lacked optical data for comparison. Later, Carlson et al. (2013) reported detection of thermal 630.0 nm emissions in the cusp using time/space agreement between calculations and observations. Using the same formulae, Kwagala et al. (2017) presented a direct comparison between the calculations and

Journal of Geophysical Research: Space Physics 10.1002/2017JA024744

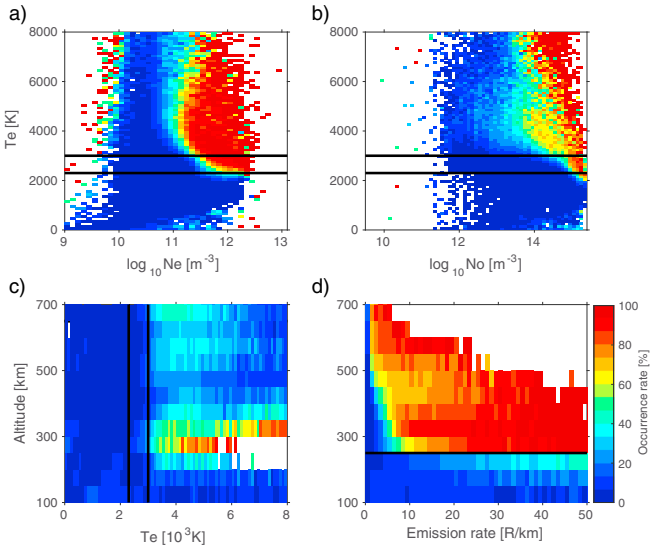

Figure 5. Occurrence rate of the strong thermally excited emissions at different electron temperatures, densities, modeled neutral atomic oxygen densities, emission rates, and altitudes. Electron temperature versus density for (a) electrons and (b) atomic oxygen. (c, d) Occurrence rate at different electron temperatures and emission rates at different altitudes. The vertical lines in Figure 5c mark electron temperatures 2300 and 3000 K. In Figures 5a and 5b, the horizontal lines mark electron temperatures 2300 and 3000 K, respectively, while that in Figure 5d marks the 250 km altitude. The color bar shows the occurrence rate.

the optical observations. All these case studies suggest that the thermal component can be dominant at the polar latitudes. Not until the present study has anyone carried out an extensive study on the thermal excitation involving large data sets. The availability of current state-of-the-art ground-based instrumentation on Svalbard has provided the possibility for our study. We now discuss the results presented in the previous section with focus on the strong thermal component.

4.1. MLT Distribution

Statistically, our study records a peak occurrence around magnetic noon and generally a higher occurrence on the dayside by a factor of 10 than on the nightside. Based on a statistical study, Zhou et al. (2000) reported the cusp to be located between 0800 and 1600 MLT, which is coincident with the highest occurrence rate in our study. This also backs up the fact that all the cases reported in literature (e.g., Carlson et al., 2013; Kwagala et al., 2017; Wickwar & Kofman, 1984) were in the cusp region, since our results suggest higher probability of such events at this location compared to the other magnetic local times. This may also be linked to the difference between the typical average energies of precipitating electrons on the nightside and dayside in the polar ionosphere, which are hard and soft, respectively (e.g., Newell et al., 2004). Although the cusp does not extend over the whole dayside where we see a relatively high occurrence rate, the magnetic merging exists throughout the dayside magnetopause and not only in the region that produces the cusp precipitation (Lockwood, Denig, et al., 1993; Newell et al., 2004).

4.2. Ionospheric Conditions

4.2.1. Prevailing Conditions

From the observations in the previous section, the electron density and temperature distributions are shown to differ between the strong and weak thermal components. We can take the weak thermal data as a representation of the average ionosphere when the contribution thermal excitation is insignificant and refer to it as the average ionosphere. Our observations show the peak occurrence rate of the strong thermal component to occur at electron temperatures 2300–4200 K (see Figures 3 and 4). According to literature, we would expect the lower limit to be ~3000 K. For the purposes of our discussion, we divide the temperature range

Journal of Geophysical Research: Space Physics 10.1002/2017JA024744

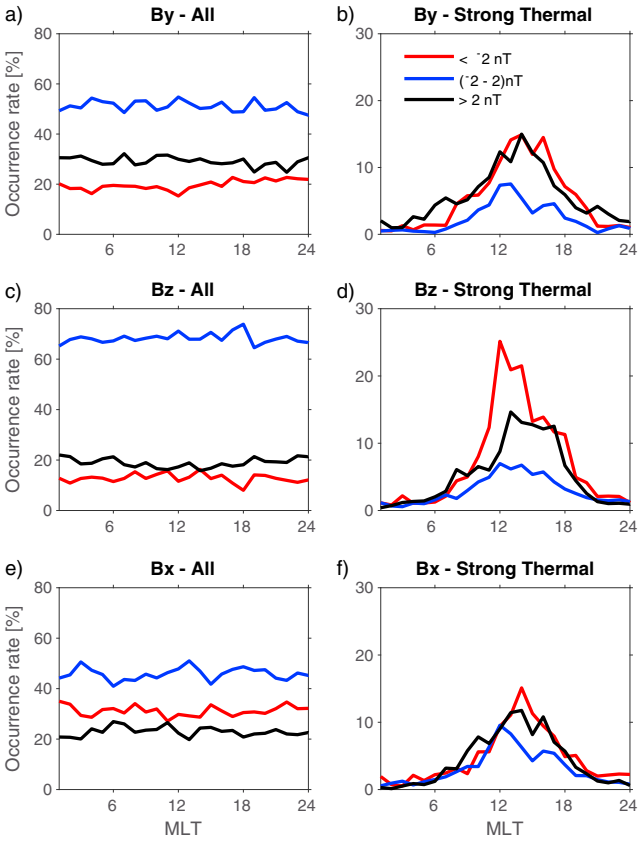

Figure 6. MLT distribution of the interplanetary magnetic field parameters B_y, B_z, and B_x. (a, c, and e) The distribution for the whole data set. (b, d, and f) The percentage of the IMF component occurring at the same time as the strong thermal component in the ionosphere. The vertical axes show the occurrence rate in percentage.

into two categories and use terms lower and high to extreme to refer to temperature ranges 2300–3000 and >3000 K, respectively. We also use terms typical and extreme for the associated electron density levels of 2×10^{11} and $>5\times10^{11}$ m^{-3}, respectively. With this in mind, looking at the electron temperature distribution in Figure 2, we find that above 250 km altitude, the electron temperatures associated with strong thermally excited emissions generally exceed those of the average ionosphere. At these altitudes, our results show that the strong thermal component is associated with high to extreme electron temperatures. These temperatures are in agreement with literature (e.g., Carlson, 1998; Carlson et al., 2013; Johnsen et al., 2012; Kozyra et al., 1990; Kwagala et al., 2017; Lockwood, Carlson, & Sandholt, 1993; Wickwar & Kofman, 1984), which suggests 3000 K as a key temperature for thermal emissions to become important. It is expected that at this temperature, the energy distribution of the electron gas can have high enough number of electrons in its high-energy tail to excite atomic oxygen to ^{1}D state.

However, we also observe a new population where an outstanding high occurrence of strong thermal emissions is present, at lower electron temperatures for extreme electron densities. The empirical atmospheric model suggests that this new population is associated with enhanced neutral atomic oxygen densities. The peak occurrence at extreme neutral atomic oxygen densities for lower electron temperatures in the strong

Journal of Geophysical Research: Space Physics 10.1002/2017JA024744

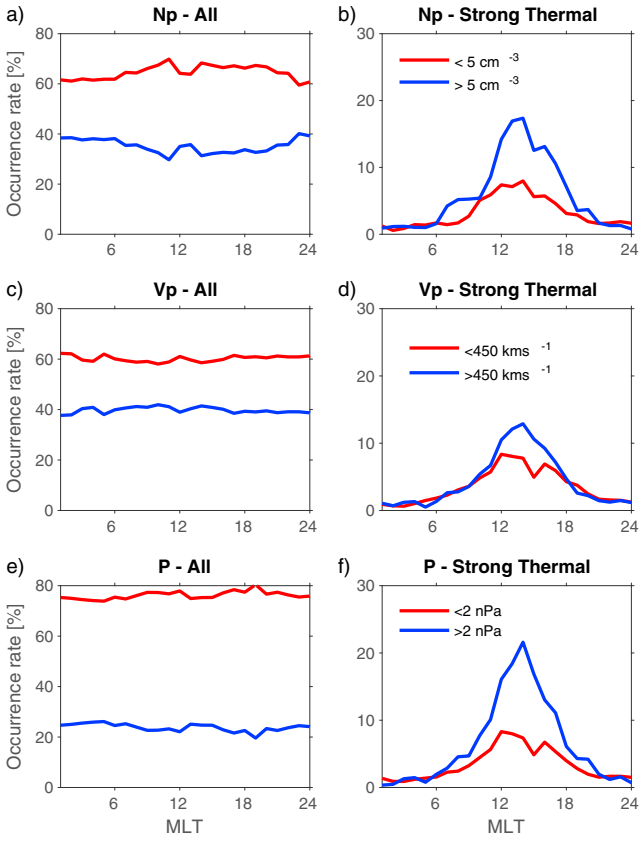

Figure 7. MLT distribution of solar wind parameters solar wind density, speed, and dynamic pressure. (a, c, and e) The distribution for the whole data set. (b, d, and f) The percentage of the solar wind parameters occurring at the same time as the strong thermal component in the ionosphere. The vertical axes show the occurrence rate in percentage.

thermal component distribution is absent in a similar distribution for the weak thermal. Generally, the rest of the model atomic oxygen densities are more evenly distributed over the different electron temperatures. There is a possibility that the generation mechanisms for the lower electron temperatures are different from those of the extreme electron temperatures. In both cases the electron density plays an equal role.

4.2.2. Electron Thermal Balance

The electron temperature in the ionosphere is determined by a thermal balance between heating and cooling rates. The heating and cooling processes in the ionosphere are equally important. Generally, the heating of the electrons is dominated by collisions between thermal and photoelectrons, which is proportional to the electron density. The electron thermal balance gets more complicated at the polar and high latitudes. There are additional heat sources like the particle precipitation and frictional heating due to the convective plasma in the polar cap which leads to frictional heating for ions which transfer part of the heat to the electrons (Schunk & Nagy, 1978). The electron gas is normally expected to cool by collisions with ambient neutrals for altitudes below 200 km and with ambient ions at higher altitudes (Brace & Theis, 1978; Kozyra et al., 1990; Schunk & Nagy, 1978; Su et al., 2015). Our study focusses on the higher altitudes and therefore interested in the latter cooling process which is proportional to the square of the electron density (Brace & Theis, 1978; Kozyra et al., 1990; Schunk & Nagy, 1978). Therefore, the ionosphere is expected to be in good thermal contact

AGU Journal of Geophysical Research: Space Physics 10.1002/2017JA024744

whenever the electron density is high. Several studies have reported the expected negative correlation between the electron density and electron temperature in the ionosphere (e.g., Brace & Theis, 1978; Bilitza, 1975; Bilitza et al., 2007; Su et al., 2015).

However, a positive correlation has also been reported in some literature (e.g., Bilitza et al., 2007). Since a positive correlation implies that the heating increases more rapidly than the electron density, an additional heat source might be required to fully account for the positive correlation (Kakinami et al., 2011). In our results (Figures 2a and 2c), we observe a high occurrence for electron temperatures of 3000 K and electron density above 10^{11} m^{-3}. This could be a positive correlation between electron temperature and density. If so, it would indicate a faster heating rate than the cooling. Carlson et al. (2013) suggests that when the ion-electron collisions are not fast enough, to achieve a thermal balance at higher electron temperatures, the electron gas cools via collisions with neutral atomic oxygen, exciting it to the ^{1}D state which deexcites by emission of 630.0 nm photons. This gives rise to the thermally excited emissions which have been reported in the polar and high-latitude ionosphere (e.g., Carlson, 1998; Carlson et al., 2013; Johnsen et al., 2012; Kwagala et al., 2017; Wickwar & Kofman, 1984).

The ^{1}D can, however, be quenched mainly by collisions with molecular nitrogen. The amount of 630.0 nm emission from thermal excitation is dependant on the neutral atmosphere densities of atomic oxygen and molecular nitrogen in addition to the electron density and temperature. Significant 630.0 nm emissions only arise at altitudes where the molecular nitrogen is infrequent. Above 250 km altitude, the molecular nitrogen density decreases significantly with altitude and the lighter atomic oxygen dominates. So in our work we consider the quenching to be negligible.

4.3. Likely Driving Mechanism

Dayside magnetopause reconnection has been reported to be characterized by nonzero IMF B_z (e.g., Trattner et al., 2007), high solar wind dynamic pressure (e.g., Fuselier et al., 2000), and enhanced ionospheric electron temperature in the ionosphere (e.g., Lockwood, Denig, et al., 1993). Our results show to a great extent these characteristics, hence indicating dayside magnetopause reconnection as a possible major driving mechanism responsible for the heating of ambient electrons in the ionosphere. Also, the high occurrence rate shown for the high solar wind density could imply increase in the magnetosheath density which on magnetic reconnection would lead to high number flux of soft precipitation in the cusp. The increase in number flux of soft precipitation implies more Coulomb collisions with the ambient electrons in the ionospheric cusp which increase the electron temperature and hence the occurrence of thermal emissions. In addition, our results suggest a strong association of the strong thermal component to the cusp signature in the ionosphere. For example, we find a strong similarity between the cusp signatures in the ionosphere reported by Nilsson et al. (1996) and the ionospheric condition we observe where there is a high occurrence rate. Vontrat-Reberac et al. (2001) estimated that the cusp electron precipitations heat the ambient electron gas to much higher temperatures compared to precipitations from other source regions. Further, Newell et al. (2004) report a 35% (25%) of the dayside merging to occur in the cusp for the southward (northward) IMF, respectively. On comparison, our study shows a possible 25% (15%) peak occurrence rate for the southward (northward) IMF configurations around magnetic noon. This could imply one of two conditional situations: either (1) if all the strong thermally exited emissions (at peak |Bz|) result from dayside merging, then 25% (15%) of southward (northward) dayside merging ends in strong thermal emission, or (2) if all strong thermal emissions arise from the cusp, then ~10% of it does not give rise to strong thermal emissions (i.e., ~ 90% of the cusp precipitation ends up in strong thermal emissions). Provided that the 630.0 nm emissions in the cusp arise from thermal excitation versus direct electron impact excitation, then we agree with earlier studies that the role of transient magnetopause reconnection in driving the global ionospheric convection could be greater than earlier anticipated (Carlson, 1998; Carlson et al., 2013; Kwagala et al., 2017; Lockwood, Carlson, & Sandholt, 1993).

4.3.1. Peak Emission Altitude

Provided that the electron precipitation from the dayside magnetic reconnection is the heating source of the electron gas in the polar ionosphere, the emission altitude of the 630.0 nm emissions has been associated with the amount of energy entering the ionosphere (Lockwood, Carlson, & Sandholt, 1993). For example, the authors point out that if the peak emission altitude doubled, it could imply that the entry area of the energy is bigger by an order of 4. Based on the distribution of emission rates at different altitude in Figure 2e, we note that the peak for the strong thermal emission is in the 300–350 km bin. This is very similar to the emission rates' altitudes in the model presented by Johnsen et al. (2012, Figure 6), where the peak volume emission rate

Journal of Geophysical Research: Space Physics 10.1002/2017JA024744

for thermal excitation was at ~350 km altitude. This peak emission altitude (~350 km) for thermally excited emission also agrees with other studies (e.g., Egeland et al., 1992; Kwagala et al., 2017; Wickwar and Kofman, 1984), however, a little lower than 400–500 km from some studies (e.g., Carlson et al., 2013; Kozyra et al., 1990).

4.4. Potential Driving Mechanisms

From the above discussion, our results suggest that the ambient electrons are, to a large extent, heated by particle precipitation originating from dayside magnetic reconnection. However, this is not the only driving process for thermal excitation in the upper polar ionosphere. Other processes, like vertical/horizontal transport and waves, could also be driving the thermal emissions as well. At midlatitudes, traveling ionospheric disturbances which are the atmospheric gravity waves' signature in the ionosphere have been reported to increase the electron density by an order of 2–4 but decrease the electron temperature by ~40% (e.g., Huang et al., 2005). With such low electron temperatures we can rule out gravity waves, and most of the horizontal transports have the same effect on electron temperature (e.g., Liu et al., 2016, and references therein). However, wave-particle interaction like the thermomagnetic mechanism described by Kagan et al. (1996) could be a potential mechanism leading to thermal excitation. On the other hand, vertical transport may potentially contribute to the heating of ambient electrons in the polar ionosphere. For example, downward heat flow in the polar cap has been reported to heat the ambient electron gas to high temperature on the nightside (e.g., David et al., 2011), however, above 800 km altitude. Our study does not go into details of these possible driving processes. Kwagala et al. (2017) also reported significant thermal component during upwelling (e.g., Ronksley, 2016; Sojka et al., 2001) for one of their case studies.

4.4.1. Neutral Upwelling

There seems to be an association between thermal excitation and neutral upwelling or density enhancements in the cusp and polar ionosphere. The neutral upwelling is believed to lead to neutral density enhancements at high altitudes, and the first observations of this were reported by Lühr et al. (2004). Soft particle precipitation from magnetic reconnection has been suggested as a major driving mechanism of upwelling (e.g., Carlson et al., 2012; Horvath & Lovell, 2017; Lühr et al., 2004; Schlegel et al., 2005). Our results also suggest the same driving mechanism for the strong thermally exited emissions. Particularly, the atomic oxygen density enhancement suggested by the model at the lower electron temperatures could indicate neutral upwelling during strong thermally excited emissions. Whether the two processes just happen to occur at the same time, or one leads to another, that remains unclear.

4.5. Assumptions and Limitations

We now discuss the uncertainty and assumptions associated with and made in our study. We used an empirical atmospheric model to derive the atomic oxygen number density. The NRLMSISE-00 model estimates the neutral number density by interpolating and extrapolating data sets for periods and geophysical conditions that are not covered by the available database which includes ground-based, rocket, and satellite measurements. Therefore, we use the model because we have no measurements of the atomic density and also neutral constituents in the thermosphere are believed to vary quite uniformly compared to their charged counterparts. However, the model is not always accurate but remains a statistical average although the database now includes more data covering extreme locations and forcing (Picone et al., 2002). Some studies have reported underestimates of 20–30% during an active high-latitude ionosphere (e.g., Forbes et al., 2005; Liu & Lühr, 2005). When Kwagala et al. (2017) accounted for the 30% underestimate, the calculated thermal component increased by 10–15% and therefore concluded that the neutral density from the model gives a lower limit of the thermal component. On a general view of the NRLMSISE-00 model compared to the other atmospheric models, Pardini et al. (2012) investigated uncertainty and bias in upper atmosphere models during the solar cycle 23 and found that the NRLMSISE-00 model had the minimum biases at all altitudes among the models that were analyzed. We therefore believe that the NRLMSISE-00 model is one of the best we could use to get the atomic oxygen density. Another model that can be used for the same purpose is the National Center for Atmospheric Research thermosphere-ionosphere-electrodynamic general circulation model (NCAR/TIE-GCM) (Qian et al., 2009, 2014; Richmond et al., 1992). We plan to look at TIE-GCM simulations in the future.

We specifically use the stationary radar beam (i.e., a fixed observation geometry), and therefore, all our data comes from a fixed area in magnetic latitude. With the 1–2 min data postintegration time, we assume that the emitting oxygen atoms and the ambient electrons remain in the same integrated area. The lifetime of the 630.0 nm emissions, which is ~110 s (Rees & Roble, 1975), is in the same ballpark as the postintegration time of the radar data (see Table 1). We further point out that the cusp is not always above Svalbard. The location

AGU Journal of Geophysical Research: Space Physics 10.1002/2017JA024744

of the cusp with respect to Svalbard is believed to be dependant on the IMF B_z configuration. When B_z is southward, then the cusp is south and more likely to be in the ESR beam; on the other hand, when the IMF is northward, the cusp most likely moves north of Svalbard, out of the ESR beam (Sandholt et al., 1998). In a statistical study on the location of the open/closed boundary, Johnsen and Lorentzen (2012) showed that the cusp would be located north of the ESR beam half of the time. For this reason, not all strong thermal emissions observed around magnetic noon will necessarily be from the cusp precipitation. Thermal excitation which leads to strong thermal emissions could be occurring outside the ESR beam as well.

5. Summary and Conclusion

We have carried out the first statistical study of thermally excited emissions based on the ESR radar measurements from the years of 2000–2015. Our study agrees with literature on the ionospheric conditions necessary for the thermally excited emissions. These conditions require the electron temperature to exceed 3000 K and electron density of $(1-5)\times10^{11}$ m^{-3} for the thermal component to be important, which we find in our study as well. However, we report a new population at relatively lower temperatures between 2300 and 3000 K when the electron density is relatively enhanced $(5-8)\times10^{11}$ m^{-3}. This could be associated with neutral upwelling or density enhancement since the neutral atmosphere model suggests that the neutral atomic oxygen density is enhanced during this new population. It remains unclear what the connection between neutral upwelling and thermal excitation is. In conclusion, we strongly recommend that all studies involving dayside 630.0 nm emissions and thermal balance in the polar and cusp ionosphere should take into account thermal excitation.

Acknowledgments
The EISCAT data were accessed from https://www.eiscat.se and processed using GUISDAP. EISCAT is an international association supported by research organizations in China (CRIRP), Finland (SA), Japan (NIPR and STEL), Norway (NFR), Sweden (VR), and the United Kingdom (NERC). The interplanetary magnetic field and solar wind data were provided by the NASA OMNIWeb service (https:omniweb.gsfc.nasa.gov/). The NRLMSISE-00 Atmospheric model was accessed from https://ccmc.gsfc.nasa.gov/modelweb/models/nrlmsise00.php. This project has been funded by the Norwegian Research Council under the contract 223252. Kjellmar Oksavik is also grateful for being selected as the 2017–2018 Fulbright Arctic Chair, and his sabbatical at Virginia Tech is sponsored by the U.S. Norway Fulbright Foundation for Educational Exchange.

References

Bilitza, D. (1975). Models for the relationship between electron density and temperature in the upper ionosphere. *Journal of Atmospheric and Terrestrial Physics*, *37*(9), 1219–1222. https://doi.org/10.1016/0021-9169(75) 90193-2

Bilitza, D., Truhlik, V., Richards, P., Abe, T., & Triskova, L. (2007). Solar cycle variations of mid-latitude electron density and temperature: Satellite measurements and model calculations. *Advances in Space Research*, *39*(5), 779–789. https://doi.org/10.1016/j.asr.2006.11.022

Brace, L. H., & Theis, R. F. (1978). An empirical model of the interrelationship of electron temperature and density in the daytime thermosphere at solar minimum. *Geophysical Research Letters*, *5*(4), 275–278. https://doi.org/10.1029/GL005i004p00275

Carlson, H. C. (1998). Response of the polar cap ionosphere to changes in (Solar Wind) IMF. In J. Moen, A. Egeland, & M. Lockwood (Eds.), *Polar cap boundary phenomena* (Vol. 509, pp. 255–270). Netherlands, Dordrecht: Springer. https://doi.org/10.1007/978-94-011-5214-3-19

Carlson, H. C., Spain, T., Aruliah, A., Skjaeveland, A., & Moen, J. (2012). First-principles physics of cusp/polar cap thermospheric disturbances. *Geophysical Research Letters*, *39*, L19103. https://doi.org/10.1029/2012GL053034

Carlson, H. C., Oksavik, K., & Moen, J. I. (2013). Thermally excited 630.0 nm O (1D) emission in the cusp: A frequent high-altitude transient signature. *Journal of Geophysical Research: Space Physics*, *118*, 5842–5852. https://doi.org/10.1002/jgra.50516

Chamberlain, J. W. (1961). Chapter 9. The airglow spectrum. In J. W. Chamberlain (Ed.), *Physics of the Aurora and Airglow, International Geophysics* (pp. 345–392). New York: Academic Press. https://doi.org/10.1016/S0074-6142(08)60657-9

David, M., Schunk, R., & Sojka, J. (2011). The effect of downward electron heat flow and electron cooling processes in the high-latitude ionosphere. *Journal of Atmospheric and Solar-Terrestrial Physics*, *73*(16), 2399–2409. https://doi.org/10.1016/j.jastp.2011.08.009

Doering, J., & Gulcicek, E. (1989). Absolute differential and integral electron excitation cross sections for atomic oxygen.7. The $^3P\rightarrow{}^1D$ and $^3P\rightarrow{}^1S$ transitions from 4.0 to 30 eV. *Journal of Geophysical Research*, *94*, 1541–1546. https://doi.org/10.1029/JA094iA02p01541

Egeland, A., Carlson, H. C., Denig, W. F., Fukui, K., & Weber, E. (1992). Day-side auroral signatures based on simultaneous, coordinated observations at Svalbard and Greenland. *IEEE Transactions on Plasma Science*, *20*(6), 726–739. https://doi.org/10.1109/27.199521

Forbes, J. M., Lu, G., Bruinsma, S., Nerem, S., & Zhang, X. (2005). Thermosphere density variations due to the 15–24 April 2002 solar events from CHAMP/STAR accelerometer measurements. *Journal of Geophysical Research*, *110*, A12S27. https://doi.org/10.1029/2004JA010856

Frank, L. A., & Craven, J. D. (1988). Imaging results from Dynamics Explorer 1. *Reviews of Geophysics*, *26*(2), 249–283. https://doi.org/10.1029/RG026i002p00249

Fuselier, S. A., Trattner, K. J., & Petrinec, S. M. (2000). Cusp observations of high- and low-latitude reconnection for northward interplanetary magnetic field. *Journal of Geophysical Research*, *105*(A1), 253–266. https://doi.org/10.1029/1999JA900422

Henry, R., Burke, P., & Sinfailam, A.-L. (1969). Scattering of electrons by C, N, O, N^+, O^+, and O^{++}. *Physical Review*, *178*, 218–225. https://doi.org/10.1103/PhysRev.178.218

Horvath, I., & Lovell, B. C. (2017). Investigating the polar ionosphere during the development of neutral density enhancements on 24–25 September 2000. *Journal of Geophysical Research: Space Physics*, *122*(4), 4600–4616. https://doi.org/10.1002/2016JA023799

Huang, C.-S., Foster, J. C., Goncharenko, L. P., Erickson, P. J., Rideout, W., & Coster, A. J. (2005). A strong positive phase of ionospheric storms observed by the Millstone Hill incoherent scatter radar and global GPS network. *Journal of Geophysical Research*, *110*, A06303. https://doi.org/10.1029/2004JA010865

Johnsen, M. G., & Lorentzen, D. A. (2012). A statistical analysis of the optical dayside open/closed field line boundary. *Journal of Geophysical Research*, *117*, A02218. https://doi.org/10.1029/2011JA016984

Johnsen, M. G., Lorentzen, D. A., Holmes, J. M., & Løvhaug, U. P. (2012). A model based method for obtaining the open/closed field line boundary from the cusp auroral 6300 Å[OI] red line. *Journal of Geophysical Research*, *117*, A03319. https://doi.org/10.1029/2011JA016980

Kagan, L. M., Kelley, M. C., & Doe, R. A. (1996). Ionospheric electron heating by structured electric fields: Theory and experiment. *Journal of Geophysical Research*, *101*, 10,893–10,907. https://doi.org/10.1029/96JA00298

Kakinami, Y., Watanabe, S., Liu, J.-Y., & Balan, N. (2011). Correlation between electron density and temperature in the topside ionosphere. *Journal of Geophysical Research*, *116*, A12331. https://doi.org/10.1029/2011JA016905

Kamide, Y., Kokubun, S., Bargatze, L., & Frank, L. (1999). The size of the polar cap as an indicator of substorm energy. *Physics and Chemistry of the Earth*, *24*, 119–127.

Journal of Geophysical Research: Space Physics 10.1002/2017JA024744

Kozyra, J. U., Valladares, C. E., Carlson, H. C., Buonsanto, M. J., & Slater, D. W. (1990). A theoretical study of the seasonal and solar cycle variations of stable aurora red arcs. *Journal of Geophysical Research*, *95*(A8), 12,219–12,234. https://doi.org/10.1029/JA095iA08p12219

Kwagala, N. K., Oksavik, K., Lorentzen, D. A., & Johnsen, M. G. (2017). On the contribution of thermal excitation to the total 630.0 nm emissions in the northern cusp ionosphere. *Journal of Geophysical Research: Space Physics*, *122*, 1234–1245. https://doi.org/10.1002/2016JA023366

Lan, V. K., Feautrier, N., Dourneuf, M. L., & Regemorter, H. V. (1972). Cross sections calculations for electron oxygen scattering using the polarized orbital close coupling theory. *Journal of Physics B: Atomic and Molecular Physics*, *5*(8), 1506–1516.

Lehtinen, M. S., & Huuskonen, A. (1996). General incoherent scatter analysis and GUISDAP. *Journal of Atmospheric and Terrestrial Physics*, *58*(1), 435–452. https://doi.org/10.1016/0021-9169(95)00047-X

Link, R. (1982). Dayside magnetospheric cleft auroral processes (PhD Thesis). Canada: York University.

Liu, H., & Lühr, H. (2005). Strong disturbance of the upper thermospheric density due to magnetic storms: CHAMP observations. *Journal of Geophysical Research*, *110*, A09S29. https://doi.org/10.1029/2004JA010908

Liu, J., Wang, W., Burns, A., Solomon, S. C., Zhang, S., Zhang, Y., & Huang, C. (2016). Relative importance of horizontal and vertical transports to the formation of ionospheric storm-enhanced density and polar tongue of ionization. *Journal of Geophysical Research: Space Physics*, *121*, 8121–8133. https://doi.org/10.1002/2016JA022882

Lockwood, M., Carlson, H. C., & Sandholt, P. E. (1993). Implications of the altitude of transient 630-nm dayside auroral emissions. *Journal of Geophysical Research*, *98*(A9), 15,571–15,587. https://doi.org/10.1029/93JA00811

Lockwood, M., Denig, W., Farmer, A., Davda, V., Cowley, S., & Lühr, H. (1993). Ionospheric signatures of pulsed reconnection at the Earth's magnetopause. *Nature*, *361*(6411), 424–428.

Lühr, H., Rother, M., Köhler, W., Ritter, P., & Grunwaldt, L. (2004). Thermospheric up-welling in the cusp region: Evidence from CHAMP observations. *Geophysical Research Letters*, *31*, L06805. https://doi.org/10.1029/2003GL019314

Mantas, G. P., & Carlson, H. C. (1991). Reexamination of the O(3P→1D) excitation rate by thermal electron impact. *Geophysical Research Letters*, *18*(2), 159–162. https://doi.org/10.1029/91GL00019

Newell, P. T., Ruohoniemi, J. M., & Meng, C.-I. (2004). Maps of precipitation by source region, binned by IMF, with inertial convection streamlines. *Journal of Geophysical Research*, *109*, A10206. https://doi.org/10.1029/2004JA010499

Nilsson, H., Yamauchi, M., Eliasson, L., Norberg, O., & Clemmons, J. (1996). Ionospheric signature of the cusp as seen by incoherent scatter radar. *Journal of Geophysical Research*, *101*(A5), 10,947–10,963. https://doi.org/10.1029/95JA03341

Pardini, C., Moe, K., & Anselmo, L. (2012). Thermospheric density model biases at the 23rd sunspot maximum. *Planetary and Space Science*, *67*(1), 130–146. https://doi.org/10.1016/j.pss.2012.03.004

Picone, J. M., Hedin, A. E., Drob, D. P., & Aikin, A. C. (2002). NRLMSISE-00 empirical model of the atmosphere: Statistical comparisons and scientific issues. *Journal of Geophysical Research*, *107*(A12), 1468. https://doi.org/10.1029/2002JA009430

Qian, L., Solomon, S. C., & Kane, T. J. (2009). Seasonal variation of thermospheric density and composition. *Journal of Geophysical Research*, *114*, A01312. https://doi.org/10.1029/2008JA013643

Qian, L., Burns, A. G., Emery, B. A., Foster, B., Lu, G., Maute, A., … Wang, W. (2014). The NCAR TIE-GCM. In J. Huba, R. Schunk, & G. Khazanov (Eds.), *Modeling the ionosphere-thermosphere system* (pp. 73–83). Chichester, UK: John Wiley. https://doi.org/10.1002/9781118704417.ch7

Rees, M. H., & Roble, R. G. (1975). Observations and theory of the formation of stable auroral red arcs. *Reviews of Geophysics*, *13*(1), 201–242. https://doi.org/10.1029/RG013i001p00201

Richmond, A. D., Ridley, E. C., & Roble, R. G. (1992). A thermosphere/ionosphere general circulation model with coupled electrodynamics. *Geophysical Research Letters*, *19*(6), 601–604. https://doi.org/10.1029/92GL00401

Ronksley, A. (2016). Optical remote sensing of mesoscale thermospheric dynamics above Svalbard and Kiruna (PhD Thesis). UK: University College London.

Sandholt, P. E., Farrugia, C. J., Moen, J., Noraberg, Ø., Lybekk, B., Sten, T., & Hansen, T. (1998). A classification of dayside auroral forms and activities as a function of interplanetary magnetic field orientation. *Journal of Geophysical Research*, *103*(A10), 23,325–23,345. https://doi.org/10.1029/98JA02156

Schlegel, K., Lühr, H., St.-Maurice, J.-P., Crowley, G., & Hackert, C. (2005). Thermospheric density structures over the polar regions observed with CHAMP. *Annales Geophysicae*, *23*(5), 1659–1672. https: //doi.org/10.5194/angeo-23-1659-2005

Schunk, R. W., & Nagy, A. F. (1978). Electron temperatures in the F region of the ionosphere: Theory and observations. *Reviews of Geophysics*, *16*(3), 355–399. https://doi.org/10.1029/RG016i003p00355

Shepherd, G. G. (1979). Dayside cleft aurora and its ionospheric effects. *Reviews of Geophysics*, *17*(8), 2017–2033. https://doi.org/10.1029/RG017i008p02017

Sims, G., Ashley, M. C. B., Cui, X., Everett, J. R., Feng, L., Gong, X., … Zhu, Z. (2012). Airglow and aurorae at dome A, Antarctica. *Publications of the Astronomical Society of the Pacific*, *124*(916), 637–649.

Sojka, J., Schunk, R., David, M., Innis, J., Greet, P., & Dyson, P. (2001). A theoretical model study of F-region response to high latitude neutral wind upwelling events. *Journal of Atmospheric and Solar-Terrestrial Physics*, *63*(14), 1571–1584. https://doi.org/10.1016/S1364-6826(01)00035-9

Solomon, S. C., Hays, P. B., & Abreu, V. J. (1988). The auroral 6300 Å emission: Observations and modeling. *Journal of Geophysical Research*, *93*(A9), 9867–9882. https://doi.org/10.1029/JA093iA09p09867

Su, F., Wang, W., Burns, A. G., Yue, X., & Zhu, F. (2015). The correlation between electron temperature and density in the topside ionosphere during 2006–2009. *Journal of Geophysical Research: Space Physics*, *120*, 10,724–10,739. https://doi.org/10.1002/2015JA021303

Thomas, L. D., & Nesbet, R. K. (1975). Low-energy electron scattering by atomic oxygen. *Physical Review A*, *11*, 170–173. https://doi.org/10.1103/PhysRevA.11.170

Trattner, K. J., Mulcock, J. S., Petrinec, S. M., & Fuselier, S. A. (2007). Probing the boundary between antiparallel and component reconnection during southward interplanetary magnetic field conditions. *Journal of Geophysical Research*, *112*, A08210. https://doi.org/10.1029/2007JA012270

Vontrat-Reberac, A., Fontaine, D., Blelly, P.-L., & Galand, M. (2001). Theoretical predictions of the effect of cusp and dayside precipitation on the polar ionosphere. *Journal of Geophysical Research*, *106*(A12), 28,857–28,865. https://doi.org/10.1029/2001JA900131

Wickwar, V. B., & Kofman, W. (1984). Dayside red auroras at very high latitudes: The importance of thermal excitation. *Geophysical Research Letters*, *11*(9), 923–926. https://doi.org/10.1029/GL011i009p00923

Zhou, X. W., Russell, C. T., Le, G., Fuselier, S. A., & Scudder, J. D. (2000). Solar wind control of the polar cusp at high altitude. *Journal of Geophysical Research*, *105*(A1), 245–251. https://doi.org/10.1029/1999JA900412

Paper III

III

Seasonal and solar cycle variations of thermally excited 630.0 nm emissions in the polar ionosphere

N. K. Kwagala, K. Oksavik, D. A. Lorentzen, M. G. Johnsen, and K. M. Laundal

Submitted to Journal of Geophysical Research

Seasonal and Solar Cycle Variations of Thermally Excited 630.0 nm Emissions in the Polar Ionosphere

Norah Kaggwa Kwagala,[1,2] Kjellmar Oksavik[1,2,3], Dag A. Lorentzen[2], Magnar G. Johnsen[4], and Karl M. Laundal[1]

[1]Birkeland Centre for Space Science, University of Bergen, Bergen, Norway.
[2]Birkeland Centre for Space Science, The University Centre in Svalbard, Longyearbyen, Norway.
[3]Center for Space Science and Engineering Research (Space@VT), Virginia Polytechnic Institute and State University, Blacksburg, VA, USA.
[4]Tromsø Geophysical Observatory, UiT - The Arctic University of Norway

Key Points:

- Thermal emissions maximize during equinox and solar maximum
- Thermal emissions are dominated by high electron temperatures at solar minimum, and by high electron densities at solar maximum
- There is an equinoctial asymmetry in the occurrence of thermal emissions at Svalbard, which reverses with the solar cycle

Corresponding author: Norah Kaggwa Kwagala, norah.kwagala@uib.no

Abstract
Solar cycle and seasonal variations have been found in the occurrence of strong thermally excited 630.0 nm emissions in the polar ionosphere. Measurements from the EISCAT Svalbard Radar have been used to derive the thermal emission intensity. Thermally excited emissions have been found to maximize at solar maximum with peak occurrence rate of ∼40% compared to ∼2% at solar minimum. These emissions also have the highest occurrence in equinox and the lowest occurrence rate in summer and winter. There is an equinoctial asymmetry in the occurrence rate which reverses with the solar cycle. This equinoctial asymmetry is attributed to variations of the solar wind-magnetosphere coupling arising from the Russell-McPherron effect. The occurrence rate of thermal excitation emission on the dayside, at Svalbard, has been found to be higher in autumn than spring at solar maximum and the reverse at solar minimum. Enhanced electron temperatures characterize the strong thermal component for solar minimum and winter, whereas enhanced electron densities characterize the thermal component for solar maximum. The results point to solar wind-magnetosphere-ionosphere coupling as the dominant controlling process.

1 Introduction

Thermally excited 630.0 nm emissions in the polar ionosphere arise when the ambient ionospheric electrons are rapidly heated by precipitating soft electrons and cool via excitation of atomic oxygen to the 1D state, which then de-excites via emission of the 630.0 nm line [*Kozyra et al.*, 1990; *Carlson*, 1996; *Carlson et al.*, 2013; *Johnsen et al.*, 2012; *Lockwood et al.*, 1993; *Kwagala et al.*, 2017, 2018]. *Kwagala et al.* [2017] found that thermally excited emissions can contribute more than 50% of the observed 630.0 nm emission intensity in the cusp ionosphere. *Kwagala et al.* [2018] presented a general statistical study on occurrence of thermally excited emissions with specific focus on the strong thermal component (intensity > 1 kR). They showed that thermally excited emissions mainly occur on the dayside and maximizes around magnetic noon. Earlier literature [e.g., *Kozyra et al.*, 1990; *Lockwood et al.*, 1993] reports 3000 K as the electron temperature beyond which thermally excited emissions can become important. *Kwagala et al.* [2018] found an additional population of thermally excited emissions at lower temperatures (∼2300-3000 K) when extreme electron densities prevailed.

Little is known about the occurrence of thermally excited emissions in the different seasons. Optical observation of these emissions is not possible when the sun is above the horizon, like during summer at Svalbard. Most cases in literature have been from winter [e.g., *Carlson et al.*, 2013; *Kwagala et al.*, 2017]. However, several statistical studies on other aspect like geomagnetic activity have reported seasonal and

semiannual variations [e.g., *Cliver et al.*, 2000; *Zhao and Zong*, 2012]. Such variations have been attributed to the variations in the orientation of the Earth's dipole axis with respect to the Parker spiral field, also known as the Russell-McPherron effect [e.g., *Russell and McPherron*, 1973; *Zhao and Zong*, 2012]. In some statistical studies at high latitudes [e.g., *Aruliah et al.*, 1996, 1997, and references therein], the Russell-McPherron effect has been given as the source of equinoctial asymmetry observed at high latitudes. It is not yet known if such variations will be seen for thermally excited emissions.

In this paper, we therefore investigate seasonal and solar cycle variations of thermally excited emissions. EISCAT Svalbard Radar (ESR) measurements are used to derive the thermal excitation component. The ESR takes measurements of ionospheric parameters irrespective of cloud cover and/or sunlight conditions. We describe our approach in section 2. Section 3 contains the observations and results. The discussion of results is given in section 4 and our conclusions are summarised in section 5.

2 Approach

In this study, we estimate the thermally excited emission intensity in the polar ionosphere using ESR measurements of electron temperature and density. The data used and methodology are described in this section.

2.1 Data

Data from the ESR 42 m beam for the period 2000-2015 has been used for the electron density and electron temperature. ESR is located at 75.12° N quasi-dipole magnetic latitude and magnetic local time is ∼UT+3 (geographic coordinates: 78.15° N, 16.02° E). The MLT is defined with respect to the subsolar point using Equation 93 of *Laundal and Richmond* [2017]. A description of the EISCAT Svalbard radar is given by *Wannberg et al.* [1997]. The handling of the EISCAT Svalbard radar data for the period of interest is described in detail by *Kwagala et al.* [2018] and is quickly summarised here. The Naval Research Laboratory Mass Spectrometer and Incoherent Scatter Radar 2000 model (NRLMSISE-00) [*Picone et al.*, 2002] has been used to generate the number density of atomic oxygen. Also in the discussion chapter we use atomic oxygen density generated by the Thermosphere-Ionosphere-Electrodynamics General Circulation Model (TIE-GCM) [*Roble et al.*, 1977, 1982; *Richmond*, 1995; *Dickinson et al.*, 1981; *Qian et al.*, 2014, 2009] for comparison. The TIE-GCM is a first principles physics-based and self consistent 3D thermosphere ionosphere model [*Roble et al.*, 1988; *Richmond et al.*, 1992; *Qian et al.*, 2014]. The sunspot number

and F10.7 cm radio flux is obtained from the NOAA/SWPC database (`ftp://ftp.swpc.noaa.gov/pub/weekly`).

2.2 Method

The volume emission rate is calculated using a formulae provided by *Carlson et al.* [2013];

$$I_{630}(h) = \alpha[T_e(h)] \times N_o(h) \times N_e(h) \quad (Rayleighs/km) \tag{1}$$

and total vertical column intensity is the line-of-sight integration of the volume emission rate;

$$I_{630} = \int_{250km}^{650km} I_{630}(h)dh \quad (Rayleighs) \tag{2}$$

where;

$$\alpha(T_e) = 0.15 \times \sqrt{T_e} \times \frac{(8537 + T_e)}{(34191 + T_e)^3} \times e^{(\frac{-22756}{T_e})} \quad (cm^3/s) \tag{3}$$

is given by *Mantas and Carlson* [1991] based on O(^{1}D) electron impact excitation cross section by *Lan et al.* [1972] for deriving O(^{1}D) excitation rates by thermal electron impact. T_e is the electron temperature in Kelvins, N_e the electron density in cm^{-3}, and N_o the atomic oxygen density in cm^{-3}. All the parameters are functions of altitude h in kilometres.

The output of the model as well as the inputs are categorised in seasons of the year and solar maximum and minimum. Further analyses are done to investigate the seasonal and solar cycle variations and dependences.

3 Observations and Results

Throughout this paper, "strong thermal emission" refers to all calculated thermally excited emission intensities exceeding 1 kR. A detailed rationale for this categorisation is given by *Kwagala et al.* [2018]. Any use of terms like thermal component or thermally excited emissions, will be referring to the strong thermal component.

3.1 Solar cycle variations

Figure 1 gives an overview of data distribution for solar maximum (red) and solar minimum (blue). Although there is more data for solar minimum (1c) than solar maximum (1a), the data is evenly distributed at all MLTs. The strong thermal component is normalised to percentage for comparison. The occurrence rate of the strong thermal component is highest at solar maximum (b). The peak occurrence

rate reaches ∼40% for solar maximum (b) whereas that for solar minimum (d) is only ∼2%. Figure 1e shows the periods for solar maximum (red) and solar minimum (blue) considered for this analysis. The periods are selected with respect to the peak and minimum sunspot number (magenta line) and f10.7 radio flux (green line) for solar maximum and minimum, respectively.

Figure 2 presents the distributions for electron density (a,c) and temperature (b,d) associated with the strong thermal component for solar minimum (a,b) and solar maximum (c,d). The black line shows the strong thermal average with the gray shading showing the standard deviation of the distributions associated with the strong thermal emission. The dotted line marks the seasonal mean for reference. We refer to the difference between strong thermal average (black line) and the seasonal mean (dotted line) as the parameter enhancement (Δ). Generally, the electron temperatures and densities are enhanced for the strong thermal component, as expected. However, the electron temperature enhancement (ΔT_e) is largest at solar minimum at altitude range 250-500 km (Figure 2b).

When we compare the strong thermal associated parameters for solar minimum (a,b) with those for solar maximum (c,d), we find that the strong thermal component at solar minimum has higher electron temperatures than at solar maximum. Furthermore, the electron densities associated with the strong thermal component at solar maximum are generally higher than those at solar minimum. The higher background electron density at solar maximum is likely responsible for the high occurrence rate and therefore the solar cycle variations that we see.

3.2 Seasonal Variations

To investigate the seasonal variation, the data is subdivided into four seasons. Figure 3 presents an overview of the data coverage for the four seasons: winter (a,b), spring (c,d), summer (e,f), and autumn (g,h). Winter is from 20th November to 20th January. Spring is from 20th February to 20th April. Summer is from 20th May to 20th July. Autumn is from 20th August to 20th October. For all seasons, the data is evenly distributed at all MLTs. The strong thermal component has highest occurrence around magnetic noon. The highest occurrence rate of the strong thermal component is seen in autumn and spring. Autumn shows higher occurrence rate than spring on the dayside, indicating an equinoctial asymmetry. There is no significant difference seen in the occurrence rate for summer and winter.

Figure 4 shows the electron density and temperature distributions associated with the strong thermal component for winter (a,b), equinox (c,d) and summer (e,f). This figure has the same format as Figure 2. Generally, the strong thermal electron

densities and temperatures are enhanced as expected. The largest electron temperature enhancement (ΔT_e) is seen in winter(b) at 250-450 km altitude, while ΔT_e is comparable for equinox(d) and summer (e) throughout the altitude range of focus (250-650 km). The electron density enhancement (ΔN_e) is largest in summer throughout the altitude range of focus, however comparable with equinox in the altitude range of 250-450 km.

4 Discussion

In this study, we have estimated the intensity of thermally excited emissions using measurements of electron temperature and density from the ESR. These measurements have been described in detail in the previous section. Atomic oxygen density is another key parameter required for thermal excitation. However, we did not have any atomic oxygen density measurements and so we used modelled atomic oxygen density from the NRLMSISE-00 model [*Picone et al.*, 2002]. We will therefore start our discussion by commenting on the modelled atomic oxygen density before discussing the solar cycle and seasonal variations seen in the previous section.

4.1 Comment on the Modelled Atomic Oxygen Density

The atomic oxygen densities from the NRLMSISE-00 model that have been used in our study to derive the thermal component are summarized in Figure 5. The average of the modelled atomic oxygen density at each altitude associated with the strong thermal component for solar maximum (red) and solar minimum (cyan) are shown in Figure 5a. The gray shading marks the spread of the modelled atomic oxygen densities associated with the strong thermal component for the respective periods. The model shows generally higher densities for solar maximum than at solar minimum. The model shows an increase of factors $\sim$6 and $\sim$9 at $\sim$350 km and $\sim$400 km, respectively, from solar minimum to solar maximum. The former and latter factors agree with *Vickers et al.* [2014] and *Emmert and Picone* [2010] who reported the same increments from estimates based on ESR measurements and satellite observations at the same altitudes, respectively.

For the seasons shown in Figure 5b, that is; winter (blue), equinox (green) and summer (red), the model shows some variations, with highest densities for equinox and lowest for winter. This is the expected seasonal variation of thermospheric density reported in literature [e.g., *Vickers et al.*, 2013, and references therein]. According to the model, there are just minor atomic oxygen density enhancements (ΔN_o) associated with the strong thermal component which show no solar cycle variations and minor seasonal variations. Therefore, the variations we see in thermal emissions are unlikely

to be due to variations in atomic oxygen density but rather variations in electron density and temperature.

When we compare the atomic oxygen density from NRLMSISE-00 model with the density from the physics-based TIE-GCM model [e.g., *Roble et al.*, 1988; *Richmond et al.*, 1992; *Qian et al.*, 2014], we get the results shown in Figure 6. Figure 6 shows the comparison between the atomic oxygen density from the two models for selected days in summer (a,b) and winter(c,d) for solar minimum (a,c) and solar maximum (b,d). Generally, the NRLMSISE-00 model produces lower atomic oxygen density than TIE-GCM. This comparison shows that the difference is biggest for winter irrespective of the solar cycle, where the TIE-GCM shows over 50% higher atomic oxygen density than the NRLMSISE-00 model that we used. Our estimates and the following discussion therefore, are a lower limit.

4.2 Solar Cycle Variation of Thermally Excited Emissions

The occurrence rate of thermally excited emission for solar maximum and solar minimum have been presented in Figure 1. The strong thermally excited emissions occur ∼20 times more frequently for solar maximum than solar minimum. The activity at the sun is highest during solar maximum [e.g., *Hathaway*, 2010]. This implies increased solar wind - magnetosphere coupling and so higher chances of magnetosphere-ionosphere coupling via particle precipitation on the dayside. We should therefore expect the ambient electrons in the polar ionosphere to be heated more frequently via this process during solar maximum compared to solar minimum. In addition, the background electron density is generally higher for solar maximum compared to solar minimum (see Figures 2a vs c). Therefore, relatively less electron temperature enhancement (ΔT_e) is required to potentially reach the thermal excitation level for solar maximum compared to solar minimum, hence the low occurrence rate should be expected at solar minimum (see Figure 1d). In addition, the electron densities are generally low for solar minimum, hence raising the electron temperature even higher for thermal excitation to become significant. Generally, with the higher electron density background, just a small increase in electron temperature is needed, which may explain the amplified solar cycle variation.

We also note that the data from the field aligned ESR might be biased depending on whether the field of view is inside the polar cap or not. The latitudinal location of the open/closed field boundary (OCB) marks the boundary of the polar cap on the dayside [e.g., *Cowley and Lockwood*, 1992]. On the dayside, the equatorward boundary of the 630.0 nm auroral emission has been used to mark the open/closed field line boundary [e.g., *Johnsen and Lorentzen*, 2012; *Johnsen et al.*, 2012]. *Johnsen and Lorentzen* [2012] found seasonal variations in the latitudinal location of the open/closed bound-

ary. They showed that during solar minimum, when the polar cap has contracted, the auroral activity is likely to move poleward of ESR beam. Therefore, thermally excited emissions could potentially be occurring but outside the ESR beam. This could potentially explain the low occurrence rate of thermal emission seen at solar minimum. However, if this was entirely responsible for the solar cycle variation we see, the thermal emission electron density and temperature at solar maximum and solar minimum would be comparable. According to Figure 2, this is not the case.

4.3 Seasonal Variation of Thermally Excited Emissions

The thermally excited emissions have been found to have the highest occurrence at equinox. There is no difference found in the occurrence rate of thermal emissions in winter and summer. This is due to the variations in electron density and electron temperature and not atomic oxygen. Other studies on other aspects like geomagnetic activity, cross-polar potential, ionospheric conductance report similar seasonal variations [e.g., *Russell and McPherron*, 1973; *Cliver et al.*, 2000, 2002; *Cnossen et al.*, 2012]. These attributed the seasonal variations to magnetic reconnection processes [e.g., *Cnossen et al.*, 2012], and an equinoctial effect which makes the southward B_z coupling less effective at the solstices [e.g., *Cliver et al.*, 2000].

Kervalishvili and Lühr [2013] reported seasonal variations of the electron temperature similar to ours, from a statistical study of thermospheric mass density enhancement. The authors found the electron temperature enhancement largest in winter, just as the electron temperature associated with the strong thermal component in the current study. Such thermospheric mass density enhancement are believed to be a result of neutral upwelling [e.g., *Lühr et al.*, 2004]. Earlier studies have reported a possible coincident occurrence of thermally excited emissions and neutral upwelling [e.g., *Kwagala et al.*, 2017]. Both neutral upwelling and thermally excited emissions are believed to be driven by the dayside magnetic reconnection and associated with soft electron precipitation and electron temperature enhancements in the cusp ionosphere, with the former associated with joule heating and the latter associated with direct electron heating by precipitating soft electrons [e.g., *Prölss*, 2008; *Sadler et al.*, 2012; *Lühr et al.*, 2004; *Zhang et al.*, 2012; *Carlson et al.*, 2013; *Kwagala et al.*, 2017, 2018]. It indicates that the two phenomena could be occurring during the same connected chain of processes in the cusp.

The background electron temperature and density includes among others the contribution from the solar EUV radiation and precipitation. During winter at Svalbard, the sun is below the horizon (zenith angle $>90°$), therefore the direct solar EUV radiation contribution is reduced which could explain the lower electron density and temperature. Since the strong thermal component occurs on the dayside, the enhance-

ments seen in winter could mainly be a result of the precipitation from the dayside magnetopause reconnection (see Figure 4a and b). Due to the already existing relatively low electron densities, large electron temperature enhancements are necessary for the thermally excited emissions to occur, which could explain the few occurrences in winter. We are also of the view that solar EUV radiation heats both ions and electrons at the same rate, and heated electrons will effectively cool via the ordinary mechanism of collision with the ions. Thus, thermal balance will to a large extent be maintained. Therefore, for summer, only when the precipitating electrons from the dayside reconnection heat the ionospheric electrons at a faster rate than the ambient ion-electron collision, will it give rise to the strong thermal emissions. For this reason the strong thermal emissions should not be frequent during summer.

When we analyse the potential bias in the ESR data due to its location with respect to the polar cap, the size of the polar cap has been reported to possibly vary in response to variations in solar wind-magnetosphere coupling [*Cnossen and Richmond*, 2012]. Since this coupling is highest at equinox, we would expect the polar cap to be in the ESR 42 m field of view more frequently. To back this up, the electron temperature (see Figure 4d and f) and density (see Figure 4c and e) in equinox and summer are comparable, when the contribution of solar EUV radiation is expected to be relatively the same on the dayside (sun above horizon). This could imply that the higher occurrence rate of thermal emissions at equinox is biased by the potential higher frequency of the polar cap in the field of view of the ESR 42 m beam.

Furthermore, the thermal component does not occur at the same rate on the dayside for spring and autumn. The equinoctial asymmetry (see Figure 3d vs h) observed in the occurrence rates of thermally excited emissions could be related to the Russell-McPherron (R-M) effect [*Russell and McPherron*, 1973]. The R-M effect is a seasonal and diurnal variation in the Earth's dipole axis with respect to the Parker spiral interplanetary magnetic field, which leads to periodic variations in solar wind magnetosphere coupling. Geomagnetic activity is predicted to maximize near equinoxes, near 23 UT in spring and 11 UT in autumn. Since the MLT of Svalbard is $\sim$UT + 3, the R-M effect predicts peak geomagnetic activity on the dayside in autumn and on the nightside in spring. This is exactly the variation that is observed in the thermal emissions. Based on this argument, we predict an opposite equinoctial asymmetry in thermal emissions in the American sector. This argument was first presented by *Aruliah et al.* [1996], who found an equinoctial asymmetry in thermospheric winds observed in Kiruna, in the same longitude sector as Svalbard. Their observations were from the nightside, and therefore the equinoctial asymmetry was opposite of what we find here. *Aruliah et al.* [1996] attributed the reversal of the asymmetry with the solar cycle to the location of the observation site with respect to the auroral oval which is consistent with our results.

5 Summary and conclusion

We have made the first statistical analysis of the seasonal and solar cycle variations of the occurrence of thermally excited emissions in the polar ionosphere. The thermal emissions have been estimated from EISCAT Svalbard Radar measurements of electron density and temperature for the period 2000-2015. Our key findings include:

1. The thermally excited emission mainly occurs on the dayside and maximizes around magnetic noon, irrespective of the season or solar cycle period.
2. The occurrence of thermally excited emissions maximizes at solar maximum, occurring ∼20 times more frequent than at solar minimum.
3. The occurrence of thermally excited emissions varies with season and maximizes at equinox.
4. There is an equinoctial asymmetry in the occurrence rate of the strong thermal emissions that is attributed to the Russell-McPherron effect.
5. Generally, the electron temperature, electron density and atomic oxygen density associated with the strong thermal component are values above average. The enhancement changes with solar cycle and season.

   i) The electron temperature enhancement is largest at solar minimum and winter.

   ii) The electron density enhancement is largest at solar maximum.

Acknowledgments
The EISCAT data were accessed from `https://www.eiscat.se` and processed using GUISDAP. EISCAT is an international association supported by research organizations in China (CRIRP), Finland (SA), Japan (NIPR and STEL), Norway (NFR), Sweden (VR), and the United Kingdom (NERC). The interplanetary magnetic field and solar wind data were provided by the NASA OMNIWeb service (`https:omniweb.gsfc.nasa.gov/`). The NRLMSISE-00 Atmospheric model was accessed from `https://ccmc.gsfc.nasa.gov/modelweb/models/nrlmsise00.php`.Simulation results have been provided by the Community Coordinated Modeling Center at Goddard Space Flight Center through their public Runs on Request system (`http://ccmc.gsfc.nasa.gov`). The TIE-GCM Model was developed by the R. G. Roble et al. at the High Altitude Observatory, National Center for Atmospheric Research (HAO NCAR). The TIE-GCM is an open-source community model available at the HAO/NCAR web site. This project has been funded by the Norwegian Research Council under the contract 223252. Kjellmar Oksavik was also grateful for being selected as the 2017-

2018 Fulbright Arctic Chair, and his sabbatical at Virginia Tech was sponsored by the U.S.-Norway Fulbright Foundation for Educational Exchange.

References

Aruliah, A. L., A. D. Farmer, T. J. Fuller-Rowell, M. N. Wild, M. Hapgood, and D. Rees (1996), An equinoctial asymmetry in the high-latitude thermosphere and ionosphere, *Journal of Geophysical Research: Space Physics*, *101*(A7), 15,713–15,722, doi:10.1029/95JA01102.

Aruliah, A. L., J. Schoendorf, A. D. Aylward, and M. N. Wild (1997), Modeling the high-latitude equinoctial asymmetry, *Journal of Geophysical Research: Space Physics*, *102*(A12), 27,207–27,216, doi:10.1029/97JA01991.

Carlson, H. C. (1996), Incoherent Scatter Radar mapping of polar electrodynamics, *Journal of Atmospheric and Terrestrial Physics*, *58*(1), 37 – 56, doi:https://doi.org/10.1016/0021-9169(95)00018-6, selected papers from the sixth international EISCAT Workshop.

Carlson, H. C., K. Oksavik, and J. I. Moen (2013), Thermally excited 630.0nm O(1D) emission in the cusp: A frequent high-altitude transient signature, *Journal of Geophysical Research: Space Physics*, *118*(9), 5842–5852, doi:10.1002/jgra.50516.

Cliver, E., Y. Kamide, and A. Ling (2002), The semiannual variation of geomagnetic activity: phases and profiles for 130 years of aa data, *Journal of Atmospheric and Solar-Terrestrial Physics*, *64*(1), 47 – 53, doi:https://doi.org/10.1016/S1364-6826(01)00093-1.

Cliver, E. W., Y. Kamide, and A. G. Ling (2000), Mountains versus valleys: Semiannual variation of geomagnetic activity, *Journal of Geophysical Research: Space Physics*, *105*(A2), 2413–2424, doi:10.1029/1999JA900439.

Cnossen, I., and A. D. Richmond (2012), How changes in the tilt angle of the geomagnetic dipole affect the coupled magnetosphere-ionosphere-thermosphere system, *Journal of Geophysical Research: Space Physics*, *117*(A10), n/a–n/a, doi:10.1029/2012JA018056, a10317.

Cnossen, I., M. Wiltberger, and J. E. Ouellette (2012), The effects of seasonal and diurnal variations in the earth's magnetic dipole orientation on solar wind-magnetosphere-ionosphere coupling, *Journal of Geophysical Research: Space Physics*, *117*(A11), doi:10.1029/2012JA017825, a11211.

Cowley, S. W. H., and M. Lockwood (1992), Excitation and decay of solar wind-driven flows in the magnetosphere-ionosphere system, *Annales Geophysicae*, *10*, 103–115.

Dickinson, R. E., E. C. Ridley, and R. G. Roble (1981), A three-dimensional general circulation model of the thermosphere, *Journal of Geophysical Research: Space Physics*, *86*(A3), 1499–1512, doi:10.1029/JA086iA03p01499.

Emmert, J. T., and J. M. Picone (2010), Climatology of globally averaged thermospheric mass density, *Journal of Geophysical Research: Space Physics*, *115*(A9), doi:10.1029/2010JA015298, a09326.

Hathaway, D. H. (2010), The solar cycle, *Living Reviews in Solar Physics*, *7*(1), 1, doi:10.12942/lrsp-2010-1.

Johnsen, M. G., and D. A. Lorentzen (2012), A statistical analysis of the optical dayside open/closed field line boundary, *Journal of Geophysical Research: Space Physics*, *117*(A2), doi:10.1029/2011JA016984, A02218.

Johnsen, M. G., D. A. Lorentzen, J. M. Holmes, and U. P. Løvhaug (2012), A model based method for obtaining the open/closed field line boundary from the cusp auroral 6300 å [OI] red line, *Journal of Geophysical Research: Space Physics*, *117*(A3), doi:10.1029/2011JA016980, A03319.

Kervalishvili, G. N., and H. Lühr (2013), The relationship of thermospheric density anomaly with electron temperature, small-scale FAC, and ion up-flow in the cusp region, as observed by champ and dmsp satellites, *Annales Geophysicae*, *31*(3), 541–554, doi:10.5194/angeo-31-541-2013.

Kozyra, J. U., C. E. Valladares, H. C. Carlson, M. J. Buonsanto, and D. W. Slater (1990), A theoretical study of the seasonal and solar cycle variations of stable aurora red arcs, *Journal of Geophysical Research: Space Physics*, *95*(A8), 12,219–12,234, doi:10.1029/JA095iA08p12219.

Kwagala, N. K., K. Oksavik, D. A. Lorentzen, and M. G. Johnsen (2017), On the contribution of thermal excitation to the total 630.0 nm emissions in the northern cusp ionosphere, *Journal of Geophysical Research: Space Physics*, doi:10.1002/2016JA023366, 2016JA023366.

Kwagala, N. K., K. Oksavik, D. A. Lorentzen, and M. G. Johnsen (2018), How often do thermally excited 630.0 nm emissions occur in the polar ionosphere?, *Journal of Geophysical Research: Space Physics*, *123*(1), 698–710, doi:10.1002/2017JA024744, 2017JA024744.

Lan, V. K., N. Feautrier, M. L. Dourneuf, and H. V. Regemorter (1972), Cross sections calculations for electron oxygen scattering using the polarized orbital close coupling theory, *Journal of Physics B: Atomic and Molecular Physics*, *5*(8), 1506.

Laundal, K. M., and A. D. Richmond (2017), Magnetic coordinate systems, *Space Science Reviews*, *206*(1), 27–59, doi:10.1007/s11214-016-0275-y.

Lockwood, M., H. C. Carlson, and P. E. Sandholt (1993), Implications of the altitude of transient 630-nm dayside auroral emissions, *Journal of Geophysical Research: Space Physics*, *98*(A9), 15,571–15,587, doi:10.1029/93JA00811.

Lühr, H., M. Rother, W. Köhler, P. Ritter, and L. Grunwaldt (2004), Thermospheric up-welling in the cusp region: Evidence from CHAMP observations, *Geophysical Research Letters*, *31*(6), doi:10.1029/2003GL019314, L06805.

Mantas, G. P., and H. C. Carlson (1991), Reexamination of the O(3P→1D) excitation rate by thermal electron impact, *Geophysical Research Letters*, *18*(2), 159–162, doi:10.1029/91GL00019.

Picone, J. M., A. E. Hedin, D. P. Drob, and A. C. Aikin (2002), NRLMSISE-00 empirical model of the atmosphere: Statistical comparisons and scientific issues, *Journal of Geophysical Research: Space Physics*, *107*(A12), doi:10.1029/2002JA009430, 1468.

Prölss, G. W. (2008), Perturbations of the upper atmosphere in the cleft region, *Journal of Atmospheric and Solar-Terrestrial Physics*, *70*(18), 2374 – 2380, doi:https://doi.org/10.1016/j.jastp.2008.06.017.

Qian, L., S. C. Solomon, and T. J. Kane (2009), Seasonal variation of thermospheric density and composition, *Journal of Geophysical Research: Space Physics*, *114*(A1), doi:10.1029/2008JA013643, a01312.

Qian, L., A. G. Burns, B. A. Emery, B. Foster, G. Lu, A. Maute, A. D. Richmond, R. G. Roble, S. C. Solomon, and W. Wang (2014), *The NCAR TIE-GCM*, pp. 73 – 83, John Wiley & Sons, Ltd, doi:10.1002/9781118704417.ch7.

Richmond, A. D. (1995), Ionospheric electrodynamics using magnetic apex coordinates, *Journal of geomagnetism and geoelectricity*, *47*(2), 191–212, doi:10.5636/jgg.47.191.

Richmond, A. D., E. C. Ridley, and R. G. Roble (1992), A thermosphere/ionosphere general circulation model with coupled electrodynamics, *Geophysical Research Letters*, *19*(6), 601–604, doi:10.1029/92GL00401.

Roble, R. G., R. E. Dickinson, and E. C. Ridley (1977), Seasonal and solar cycle variations of the zonal mean circulation in the thermosphere, *Journal of Geophysical Research*, *82*(35), 5493–5504, doi:10.1029/JA082i035p05493.

Roble, R. G., R. E. Dickinson, and E. C. Ridley (1982), Global circulation and temperature structure of thermosphere with high-latitude plasma convection, *Journal of Geophysical Research: Space Physics*, *87*(A3), 1599–1614, doi:10.1029/JA087iA03p01599.

Roble, R. G., E. C. Ridley, A. D. Richmond, and R. E. Dickinson (1988), A coupled thermosphere/ionosphere general circulation model, *Geophysical Research Letters*, *15*(12), 1325–1328, doi:10.1029/GL015i012p01325.

Russell, C. T., and R. L. McPherron (1973), Semiannual variation of geomagnetic activity, *Journal of Geophysical Research*, *78*(1), 92–108, doi:10.1029/JA078i001p00092.

Sadler, F. B., M. Lessard, E. Lund, A. Otto, and H. Lhr (2012), Auroral precipitation/ion upwelling as a driver of neutral density enhancement in the cusp, *Journal of Atmospheric and Solar-Terrestrial Physics*, *8788*, 82 – 90, doi:http://dx.doi.org/10.1016/j.jastp.2012.03.003.

Vickers, H., M. J. Kosch, E. Sutton, Y. Ogawa, and C. La Hoz (2013), Thermospheric atomic oxygen density estimates using the EISCAT Svalbard Radar, *Journal of Geophysical Research: Space Physics*, *118*(3), 1319–1330, doi:10.1002/jgra.50169.

Vickers, H., M. J. Kosch, E. Sutton, L. Bjoland, Y. Ogawa, and C. La Hoz (2014), A solar cycle of upper thermosphere density observations from the EISCAT Svalbard Radar, *Journal of Geophysical Research: Space Physics*, *119*(8), 6833–6845, doi:10.1002/2014JA019885.

Wannberg, G., I. Wolf, L.-G. Vanhainen, K. Koskenniemi, J. Röttger, M. Postila, J. Markkanen, R. Jacobsen, A. Stenberg, R. Larsen, S. Eliassen, S. Heck, and A. Huuskonen (1997), The EISCAT Svalbard radar: A case study in modern incoherent scatter radar system design, *Radio Science*, *32*(6), 2283–2307, doi:10.1029/97RS01803.

Zhang, B., W. Lotko, O. Brambles, M. Wiltberger, W. Wang, P. Schmitt, and J. Lyon (2012), Enhancement of thermospheric mass density by soft electron precipitation, *Geophysical Research Letters*, *39*(20), doi:10.1029/2012GL053519, l20102.

Zhao, H., and Q.-G. Zong (2012), Seasonal and diurnal variation of geomagnetic activity: Russell-mcpherron effect during different imf polarity and/or extreme solar wind conditions, *Journal of Geophysical Research: Space Physics*, *117*(A11), doi:10.1029/2012JA017845, a11222.

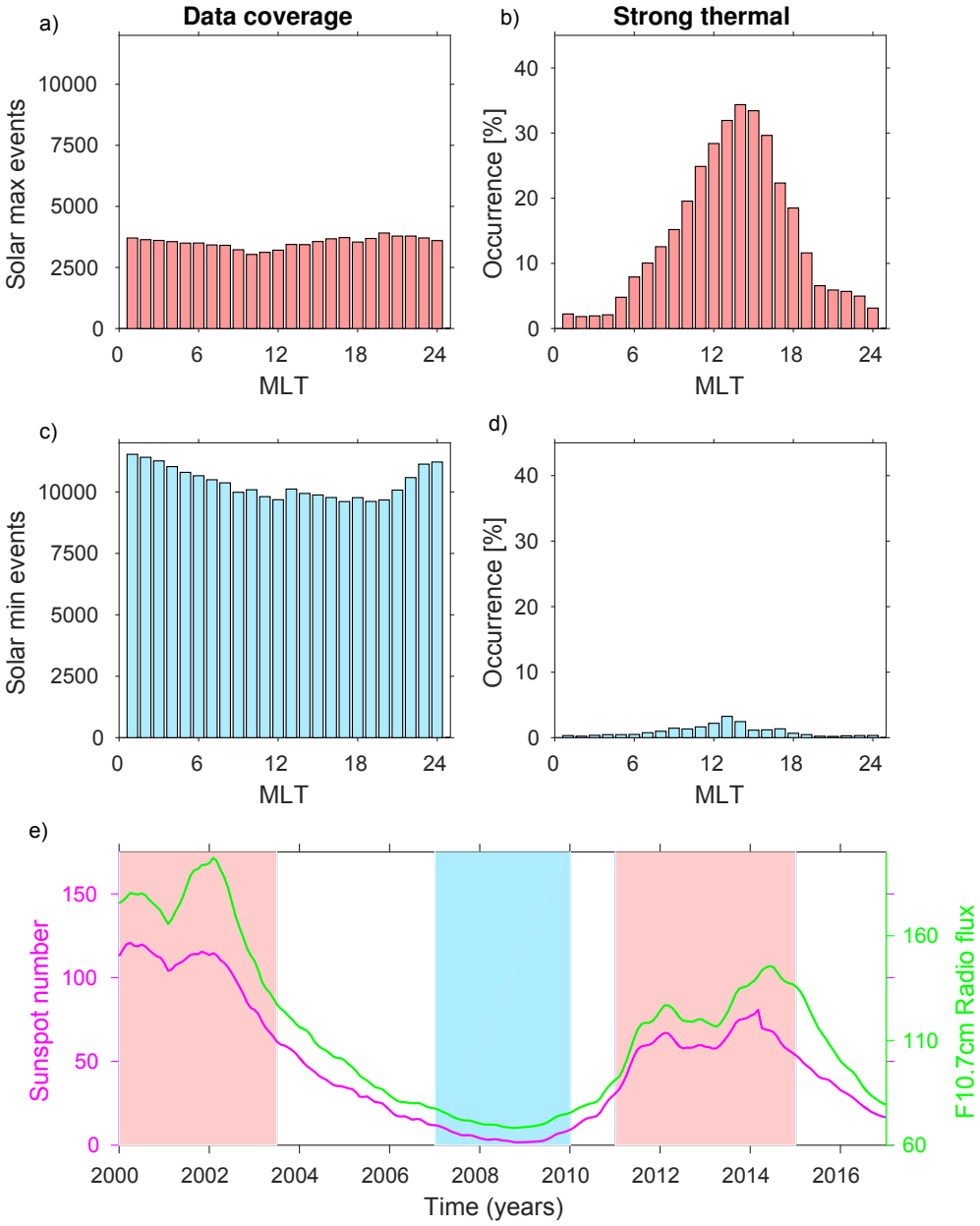

Figure 1. Data coverage for solar maximum (a,b) and solar minimum (c,d). The left column (a,c) is data coverage for reference only, and the right column (b,d) is the MLT distribution of the strong thermal emissions which is the focus of this paper. Panel e shows the monthly averaged sunspot number (magenta) and F10.7 cm solar flux (green) progression after year 2000. The red shading is used to indicate the period for solar maximum shown in a and b. The blue shading is used to indicate the period for solar minimum shown in c and d. Higher occurrence rate is seen for solar maximum.

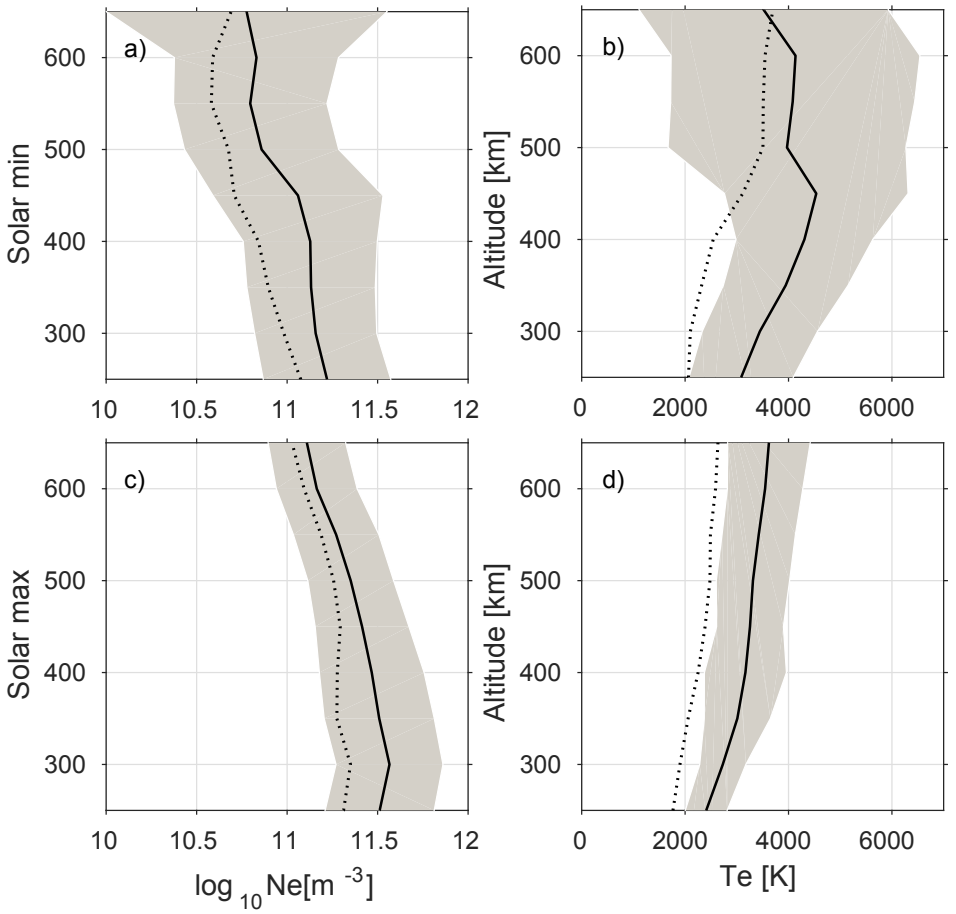

Figure 2. Distribution of electron temperature (b,d) and electron density (a,c) for solar minimum (a,b) and solar maximum (c,d), associated with the strong thermal component. The black line shows the strong thermal average with the gray shading marking the standard deviation of the strong thermal distribution. The dotted line shows the solar minimum/maximum mean for reference.

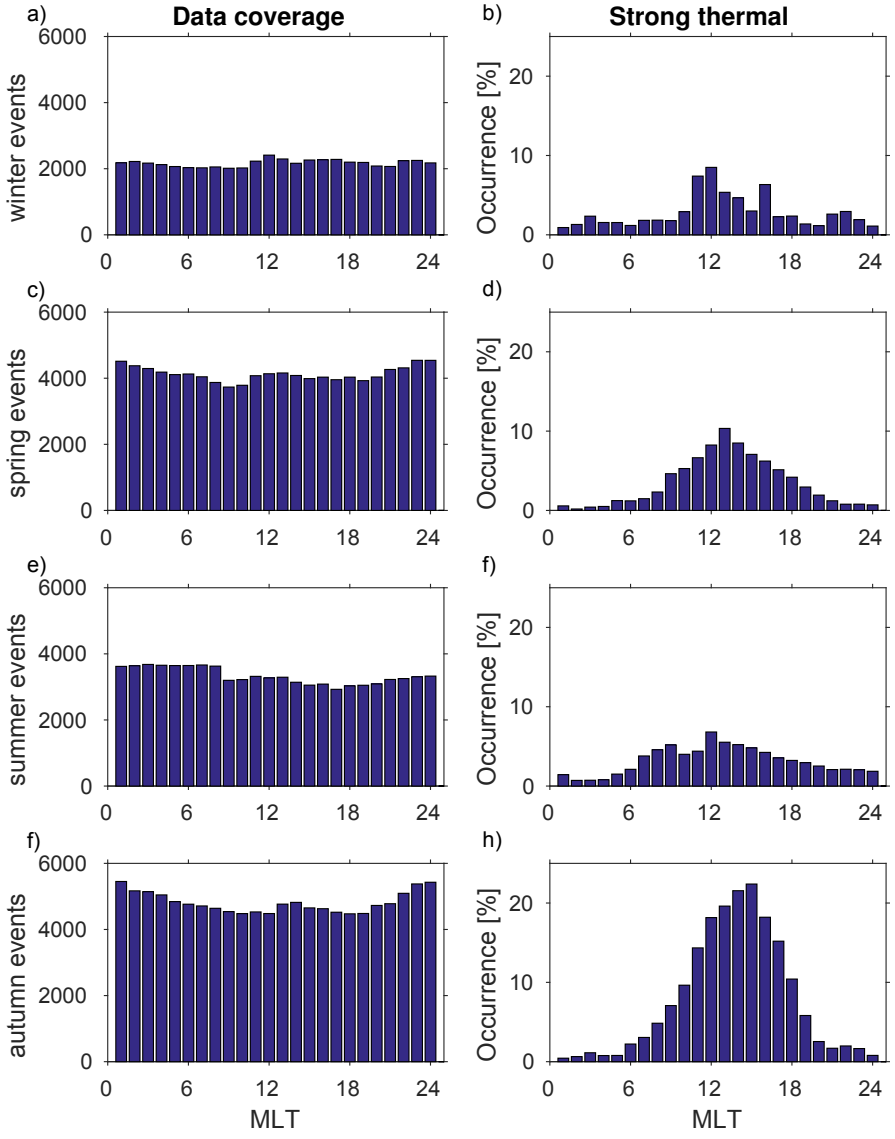

Figure 3. Data coverage for the four seasons of the year: winter (a,b), spring (c,d), summer (e,f), and autumn (g,h). The left column (a,c,e,g) is data coverage for reference only, and the right column is MLT distribution of the strong thermal events that is the focus of this paper. The highest occurrence is seen in equinox (spring and autumn).

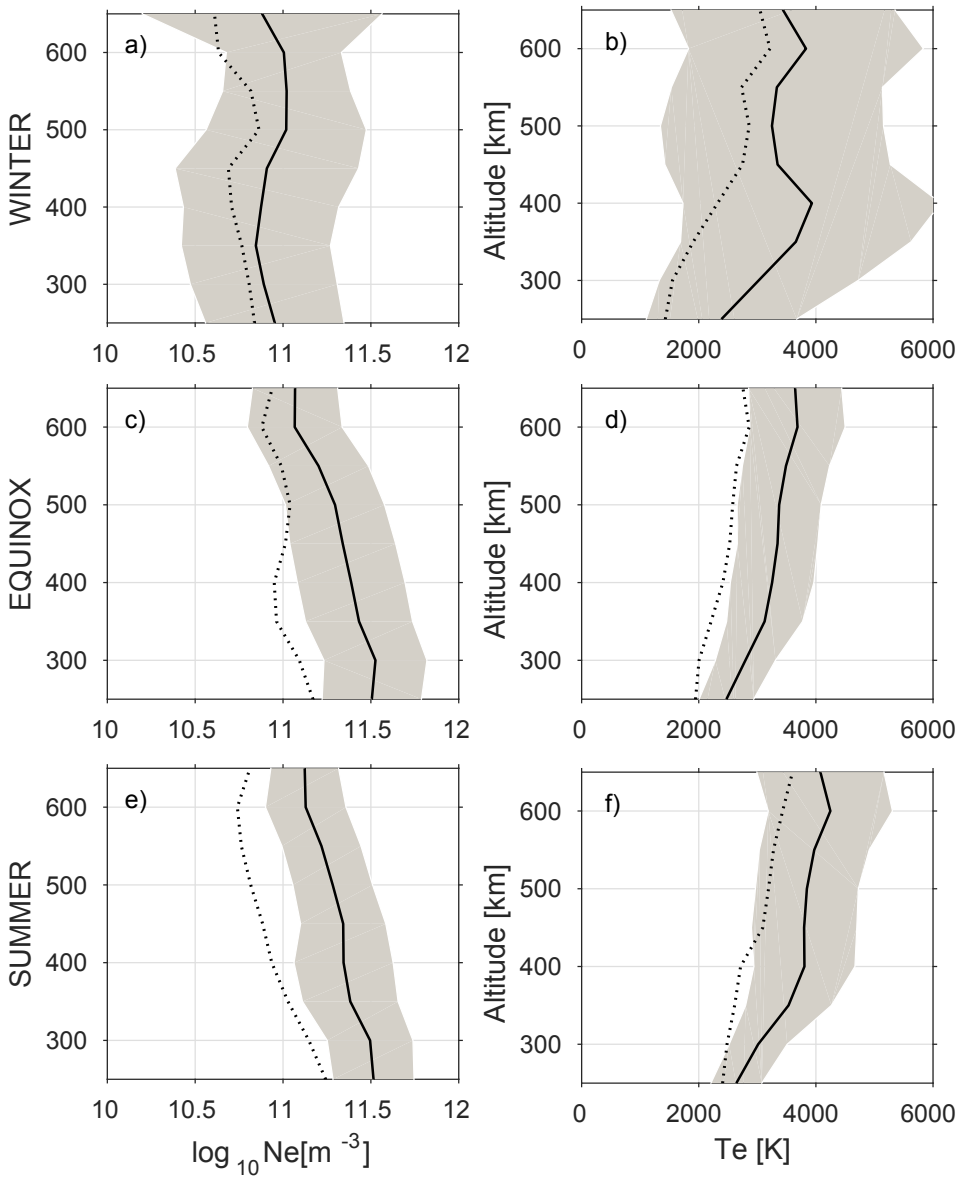

Figure 4. Distribution of electron temperature (b,d,f) and electron density (a,c,e) for winter (a,b), equinox (c,d) and summer (e,f), associated with the strong thermal component. The black line shows the strong thermal average with the gray shading marking the standard deviation of the strong thermal distribution. The dotted line shows the seasonal mean for reference. The thermal emission electron temperature is higher at solar minimum than at solar maximum. The thermal emission electron density is higher at solar maximum than at solar minimum.

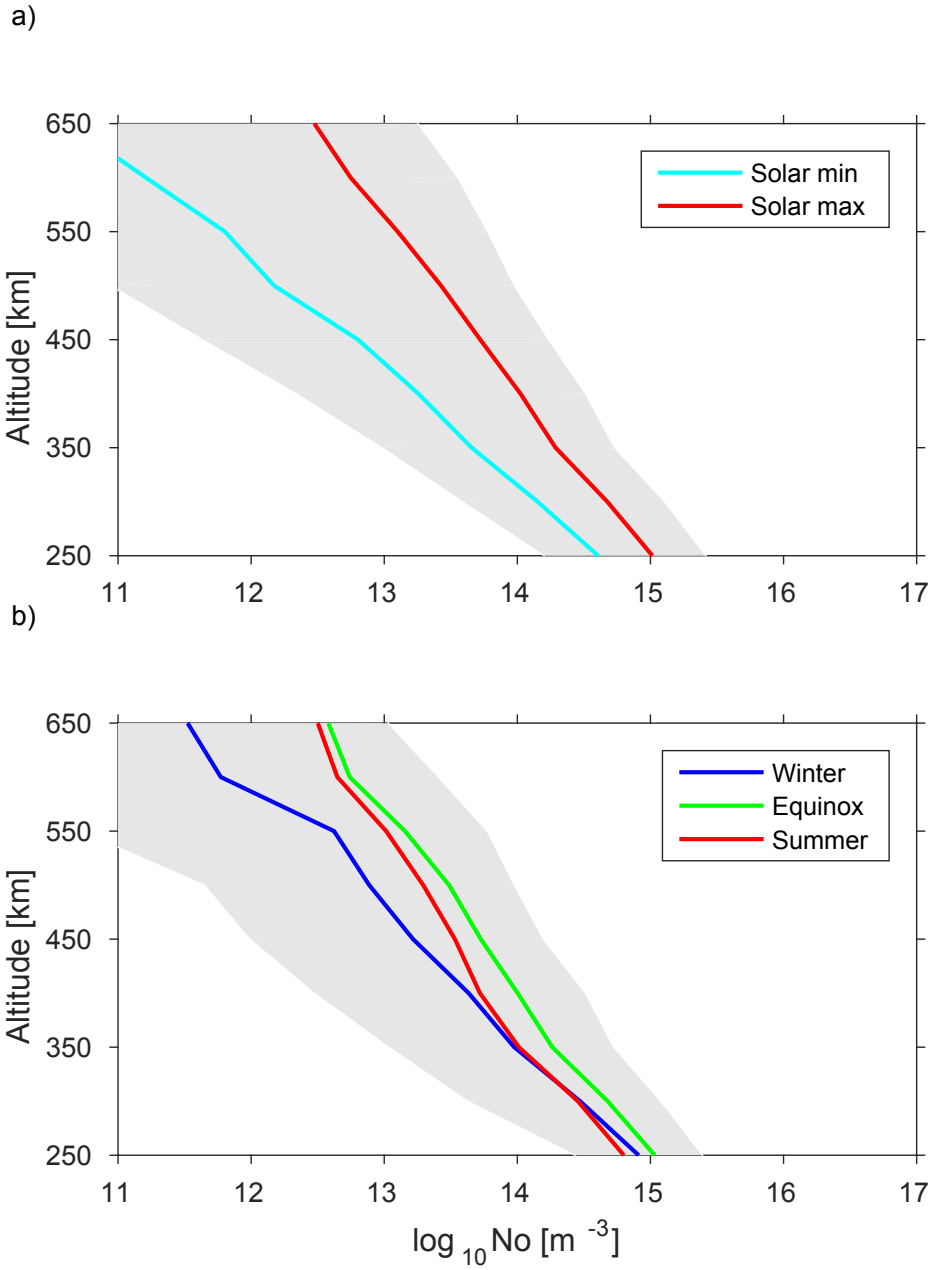

Figure 5. The NRLMSISE-00 model atomic oxygen density averaged at each altitude, for the strong thermal component. (a) solar maximum (red) and solar minimum (cyan). (b) winter (blue), equinox (green) and summer (red). The gray shading shows the spread of the atomic oxygen densities. The density is highest at solar maximum (a) and equinox (b) and lowest at solar minimum and winter.

Graphic design: Communication Division, UiB / Print: Skipnes Kommunikasjon AS

uib.no

ISBN: 978-82-308-3702-3